

REPORT DOCUMENTATION PAGE

Public reporting burden for this collection of information is estimated to average 1 hour per response, including gathering and maintaining the data needed, and completing and reviewing the collection of information. Send collection of information, including suggestions for reducing this burden, to Washington Headquarters Services, Davis Highway, Suite 1204, Arlington, VA 22202-4302, and to the Office of Management and Budget, Paperwork

AFRL-SR-AR-TR-02-

0320

1. AGENCY USE ONLY (Leave blank)		2. REPORT DATE 19-JUL-2002		3. REPORT FINAL (21-JUN-1999 TO 30-NOV-2001)	
4. TITLE AND SUBTITLE CONTROL AND OPTIMIZATION OF REGENERATIVE POWER FLOW IN 21ST CENTURY AIRLIFTERS				5. FUNDING NUMBERS F49620-99-C-0035	
6. AUTHOR(S) DR. DOUGLAS K. KINDER DR. DUSHAN BOROYEVICH					
7. PERFORMING ORGANIZATION NAME(S) AND ADDRESS(ES) CENTER FOR POWER ELECTRONIC SYSTEMS THE BRADLEY DEPT. OF ELECTRICAL AND COMPUTER ENGINEERING 657, WHITTEMORE HALL BLACKSBURG, VA 24061-0111				8. PERFORMING ORGANIZATION REPORT NUMBER	
9. SPONSORING/MONITORING AGENCY NAME(S) AND ADDRESS(ES) AIR FORCE OFFICE OF SCIENTIFIC RESEARCH 4015 WILSON BOULEVARD ARLINGTON, VA 22203				10. SPONSORING/MONITORING AGENCY REPORT NUMBER	
11. SUPPLEMENTARY NOTES					
12a. DISTRIBUTION AVAILABILITY STATEMENT				20021008 177	
Approved for public release; distribution unlimited					
13. ABSTRACT (Maximum 200 words) In this project we investigated the optimization of the power distribution system and some of its components for 21st century airlifters. Herein we describe the formulation of an optimization problem for typical components found in a power distribution system: an input filter and a buck converter. The optimization formulation includes time and frequency domain constraints as well as optimization of the inductors. An optimization problem is formulated for each of the components, but it is formulated in such a way that the two-optimization problems can be easily integrated into a single optimization problem accounting for internal stability. Using this principle, an optimization problem can be formulated for each component of the power distribution system, and then integrated into the combined optimization of the entire system. An example is given in which the system is optimized to bound the effect of the regenerative power flow onto the aircraft power bus. A bi-Level formulation is introduced which significantly reduces the computational complexity of the optimization problem. It is anticipated that the next generation aircraft will include novel actuators that incorporate piezoelectric material. Since this material is an energy transducer, we can expect these actuators to regenerate power back onto the power bus. To study this effect, models are developed of the actuators and the power flow is investigated as a function of the internal control loops. Then an optimization problem is formulated for the drive amplifiers for these actuators.					
14. SUBJECT TERMS				15. NUMBER OF PAGES 165	
				16. PRICE CODE	
17. SECURITY CLASSIFICATION OF REPORT UNCLASSIFIED	18. SECURITY CLASSIFICATION OF THIS PAGE UNCLASSIFIED	19. SECURITY CLASSIFICATION OF ABSTRACT UNCLASSIFIED	20. LIMITATION OF ABSTRACT		

JUL 19 2002

Control and Optimization of Regenerative Power Flow In 21st Century Airlifters

Final Report

For the period
June 21, 1999 to November 30, 2001

Sponsored By

Air Force Office of Scientific Research
New World Vistas Program
Subsystem Integration and Power

AFOSR Contract Number: F49620-99-C-0035

Dr. Craig S. Hartley, Program Manager
AFOSR/NA
801 North Randolph Street, Room 732
Arlington, VA 22203-1977

December 1, 2001

Prepared by

Dr. Douglas K. Lindner, Dr. Dushan Boroyevich

Center for Power Electronic Systems
The Bradley Department of Electrical and Computer Engineering
657, Whittemore Hall
Blacksburg, VA 24061 - 0111

Executive Summary

In this project we investigated the optimization of the power distribution system and some of its components for 21st century airlifters.

Herein we describe the formulation of an optimization problem for typical components found in a power distribution system: an input filter and a buck converter. The optimization formulation includes both time and frequency domain constraints as well as optimization of the inductors. An optimization problem is formulated for each of the components, but it is formulated in such a way that the two optimization problems can be easily integrated into a single optimization problem accounting for internal stability. Using this principle, an optimization problem can be formulated for each component of the power distribution system, and then integrated into the combined optimization of the entire system. An example is given in which the system is optimized to bound the effect of the regenerative power flow onto the aircraft power bus. A bi-level formulation is introduced which significantly reduces the computational complexity of the optimization problem.

It is anticipated that the next generation aircraft will include novel actuators that incorporate piezoelectric material. Since this material is an energy transducer, we can expect these actuators to regenerate power back onto the power bus. To study this effect, models are developed of the actuators and the power flow is investigated as a function of the internal control loops. Then an optimization problem is formulated for the drive amplifiers for these actuators.

The interconnection of components in power distribution systems poses both linear and nonlinear stability problems. In this study several of these stability issues are investigated. The stable interaction between the input filter and a three-phase AC-DC converter is characterized using the Middlebrook criteria and singular values. The stability of a bidirectional converter under two-way power flow is investigated. Finally, the stability of a nonlinear system is investigated using bifurcation methods. An optimal parameter update is proposed that maximizes the stability margins of the system.

Directed energy weapons are expected to play an important role in the future. An important component in such a weapon is the thyristor assembly, which handles the power flow. We describe a multidisciplinary optimization problem for the design of the thyristor that includes mechanical, electrical, and thermal properties. Neural networks are used to reduce the computational cost.

The following individuals contributed to this research: Dr. Douglas K Lindner, Dr. Dushan Boroyevich, Mr. Sriram Chandrasekaran, Mr. Konstantin Louganski, Dr. Scott Ragon, Mr. Sergio Busquet-Monge, Ms. Chunping Song.

Table Of Contents

1. INTRODUCTION.....	4
1.1 ORGANIZATION OF THE REPORT.....	5
2. BASELINE POWER SYSTEM.....	6
2.1 ARCHITECTURE.....	7
2.1.1. <i>Actuation Loads</i>	9
2.2 REGENERATIVE ENERGY	11
2.2.1. <i>Electromechanical Actuator Modeling</i>	13
3. OPTIMIZATION OF A SAMPLE SYSTEM.....	16
3.1 SAMPLE POWER SYSTEM	17
3.2 MODEL DEVELOPMENT.....	18
3.2.1. <i>Input Filter</i>	18
3.2.2. <i>Buck Converter</i>	19
3.2.3. <i>Inductor Model</i>	20
3.3 OPTIMIZATION OF THE INPUT FILTER	21
3.3.1. <i>Design Variables</i>	21
3.3.2. <i>Constraints</i>	22
3.3.3. <i>Objective Function</i>	26
3.3.4. <i>Optimization Results</i>	27
3.4 OPTIMIZATION OF THE BUCK CONVERTER.....	30
3.4.1. <i>Design Variables</i>	30
3.4.2. <i>Constraints</i>	31
3.4.3. <i>Objective Function</i>	35
3.4.4. <i>Optimization Results</i>	35
3.5 OPTIMIZATION OF SAMPLE SYSTEM.....	37
3.6 BI-LEVEL OPTIMIZATION OF THE INPUT FILTER	42
3.6.1. <i>Bi-Level Formulation for System Design</i>	42

3.6.2.	<i>Bi-Level Inductor Design Problem</i>	58
3.6.3.	<i>Future Work: Three-Level Filter Design Problem</i>	64
4.	ANALYSIS AND OPTIMIZATION OF SMART ACTUATORS	64
4.1	MODELING OF THE ACTUATOR AND STRUCTURE	64
4.1.1.	<i>Anhysteretic Nonlinearity</i>	69
4.2	OPTIMIZATION OF THE DRIVE AMPLIFIER.....	72
4.2.1.	<i>Problem Definition</i>	73
4.2.2.	<i>Model Development</i>	75
4.2.3.	<i>Determination of DC Bus Voltage</i>	80
4.2.4.	<i>Estimation of Actuator Current Ripple</i>	83
4.2.5.	<i>Formulation of optimization problem</i>	86
4.2.6.	<i>Optimization Results</i>	88
4.3	ACTIVE DAMPING USING PIEZOELECTRIC ACTUATORS.....	89
4.3.1.	<i>Active damping of structure</i>	90
4.3.2.	<i>Amplifier Requirements</i>	93
4.3.3.	<i>Power Flow Analysis</i>	96
5.	BIFURCATION ANALYSIS AND OPTIMIZATION	103
5.1	MULTIVARIABLE IMPEDANCE RATIO CRITERION	103
5.1.1.	<i>Middlebrook Impedance Ratio Criterion</i>	104
5.1.2.	<i>Input Filter Interaction in Three-Phase AC-DC Converters</i>	105
5.1.3.	<i>Three Phase Boost Rectifier</i>	109
5.1.4.	<i>Effect of Input Filter on Rectifier Performance</i>	112
5.1.5.	<i>Sufficient Condition for Stability</i>	114
5.2	STABILITY UNDER BIDIRECTIONAL POWER FLOW	118
5.2.1.	<i>Stability under Bidirectional Power Flow</i>	119
5.3	BIFURCATION METHODS.....	123
5.3.1.	<i>Input Filter Interaction</i>	124
5.3.2.	<i>Interaction at the DC Bus</i>	135
5.4	OPTIMAL PARAMETER UPDATE.....	139
5.4.1.	<i>Bifurcation Margin</i>	139

5.4.2.	<i>Computation of the Gradient</i>	141
5.4.3.	<i>Simulation Results</i>	145
6.	OPTIMIZATION OF A THYRISTOR ASSEMBLY	146
6.1	THYRISTOR ASSEMBLY	147
6.2	SIMULATION	149
6.3	OPTIMIZATION FORMULATION	150
6.3.1.	<i>Design Variables</i>	150
6.3.2.	<i>Fixed Parameters</i>	151
6.3.3.	<i>Constraints</i>	152
6.3.4.	<i>Objective Function</i>	153
6.4	OPTIMIZATION ALGORITHM.....	153
6.5	SOFTWARE INTERFACE.....	154
6.5.1.	<i>Direct Interface</i>	154
6.5.2.	<i>Neural Network Interface</i>	155
6.6	OPTIMIZATION RESULTS	158
6.6.1.	<i>Optimization with Electrical Constraints</i>	158
6.6.2.	<i>Optimization with Thermal and Electrical Constraints</i>	161
6.7	CONCLUSIONS.....	162
7.	REFERENCES	163

1. Introduction

The principal objective of the research presented in this report is to develop mathematical optimization methodologies and tools for the design of next generation power systems. It is projected that in next generation transport aircraft, all power (except propulsion) will be distributed and processed electrically. In other words, electrical power will be utilized for driving aircraft subsystems currently powered by hydraulic, pneumatic or mechanical means including utility and flight control actuation, environmental control system, lubrication and fuel pumps, and numerous other utility functions. In addition, modern aircraft are also equipped with electrically driven, structurally integrated smart actuators that are used for active vibration control of wing surfaces in order to reduce fatigue and mechanical wear and tear. These concepts are embraced by what is known as the "More Electric Aircraft (MEA)" initiative. The MEA emphasizes the utilization of electrical power as opposed to hydraulic, pneumatic, and mechanical power for optimizing aircraft performance and life cycle cost. For example, hydraulically driven actuators would be replaced by electric motor driven pumps, and a pneumatically driven compressor for environmental control would be replaced by an electric motor driven compressor. Some expected benefits of moving to an MEA or "Power-By-Wire" secondary power systems are listed below:

Reduced design complexity	Reduced production labor
Fewer design components	Shorter checkout time
Smaller certification workload	Less ground support equipment
Lower flight test hours	Higher system reliability
Reduced procurement workload	Less spared inventory
Lower total component/system cost	Easier aircraft modification
Reduced parts count	Enhanced safety
Less tooling	Less environmental impact

Increasing use of electric power is seen as direction of technological opportunity for aircraft power systems based on rapidly evolving advancements in power electronics, fault tolerant electrical power distribution systems and electrically driven primary flight control actuator systems. The decision to convert to electrically driven subsystems depends on the overall cost and performance benefits. Thus reliable, high power density motors and motor drives with power ratings ranging from a few horsepower to hundreds of horsepower will be required. More importantly, the magnitude, quality, reliability, and fault tolerance of the electric power to be generated and distributed in the aircraft must be significantly greater than what the present state-of-the-art technology can provide. The aircraft power distribution system hence, plays a central role in the developing concepts of "Power-by-Wire" and "More Electric Aircraft". The MEA will need a highly reliable, fault tolerant, autonomously controlled electrical power system to deliver high quality power from the sources to the load.

The concept of the "More Electric Aircraft" has been in existence for a little less than a decade, and a considerable amount of research effort has been devoted to the

development of advanced technologies in power electronics, motor drives, actuation systems and generating equipment. However, design methodologies to appropriately integrate the different subsystems together and control their interactions have not received much attention. The research reported here represents a step in this direction.

In this report, the utility of optimization methods is demonstrated for the design of an interconnected system consisting of an input filter and a regulated DC-DC buck converter (called the sample system), the design of the drive amplifier for a piezoelectric actuator, and the design of a thyristor assembly for high-power applications. The formulation of the optimization problems consists of model development, identification of design variables, definition of the optimization constraints and the objective function. Several of the optimization formulations use linear analysis methods to guarantee internal stability of individual systems and stability of the interconnected system. However, due to the nonlinear nature of the systems in the power distribution system, linear techniques only provide information on local stability information. Hence, a significant amount of effort has been devoted to the study of nonlinear stability and subsystem interaction analysis methods.

1.1 Organization of the Report

In Part 2, the baseline power system architecture is introduced. The origin and nature of regenerative power from flight control actuators is briefly discussed. A detailed model of the EMA is simplified to an interconnected system consisting of a DC-DC buck converter preceded by an EMI input filter. This is used as the sample system for the optimization methodology in Part 3.

Part 3 of this report focuses on the development of automated optimization methodologies for the design of a simple interconnected system called the sample power system which consists of an EMI input filter followed by a regulated DC-DC buck converter. The baseline power system architecture is introduced, and the origin and nature of regenerative power from flight control actuators is briefly discussed. The development of the optimization methodology for the sample system is presented next. The optimization formulation of the input filter is described first. The identification of the design variables, definition of the constraints and the objective function are explained in detail. This is followed by the optimization formulation for the design of the buck converter. The individual optimization methodologies are combined to yield the optimization formulation for the sample system. It is shown that optimizing the integrated system as a whole results in a lower weight compared to that obtained by integrating the individually optimized systems. Finally, a multi-level optimization methodology is introduced for the purpose of reducing the computational cost of the optimization process. This methodology is demonstrated using the filter design problem.

Part 4 of the dissertation deals with the modeling, optimization and control of a piezoelectric stacked actuator. A detailed electromechanical model of the actuator coupled with a simple mechanical structure is developed that includes the anhysteretic

nonlinearity between the polarization and the electric field in the actuator. An optimization methodology for the design of a current controlled amplifier for driving the actuator is developed. The optimization formulation is used to determine the DC bus voltage and the physical design of the inductor. Optimization results are presented to illustrate the effectiveness of the proposed methodology. Finally, A control law is presented wherein actuator is used for actively damping the mechanical structure. The current flowing in the actuator is controlled to be proportional to the acceleration of the structure. A detailed analysis of the mechanical power flow between the actuator and the amplifier is presented. Guidelines to design the current controlled amplifier based on the peak current and voltage in the actuator are proposed.

Part 5 of the report is devoted to development of techniques for the analysis of stability and interaction between interconnected subsystems. First, the interaction between a three phase input filter and a three phase boost rectifier is studied, and a multivariable impedance ratio criterion based on the singular values of terminal impedances is proposed to guarantee stability and minimal interaction. Simplifying approximations that lend the criterion to physical insight are presented. Second, the integrated stability analysis of a regulated power converter with an input filter under bi-directional power flow is examined. The converter is modeled as a constant power load and a simplified but insightful analysis of stability is presented. It is shown that the forward direction of power flow is more critical to the stability of the system than the reverse direction. Third, the use of bifurcation methods to obtain global stability information about integrated systems is described. Specifically, the interaction between an input filter and a regulated DC-DC buck converter and that between the bus regulator and a load converter in a simplified power system are presented. The results are compared with those obtained from linear analysis methods and their implications on the design of these subsystems are discussed. Finally, a nonlinear design methodology, founded in the field of power systems, is applied to incrementally improve the robustness of a nonlinear system by directing the system away from the onset of instability through a bifurcation. The method is demonstrated using the example of a regulated DC-DC boost converter. The potential incorporation of this design technique to an optimization formulation is discussed.

In Part 6, the optimization methodologies developed for the aircraft power distribution system are extended to the design of a thyristor stack for pulsed power applications. The thyristor stack is designed subject to constraints on its electrical and thermal performance characteristics. To perform the optimization, a software tool for multi-disciplinary optimization is developed using an evolutionary strategies algorithm and neural network technology. The tool allows commonly used off-the-shelf analysis tools such as Ansoft Maxwell 3D and Orcad PSPICE to be used efficiently as part of the optimization process. Results obtained for the thyristor stack assembly are presented and discussed.

2. Baseline Power System

In this section, the baseline architecture of the power distribution system is described. The power distribution system is based on the proposed next generation 270V DC bus.

The Electromechanical (EMA) and Electrohydraulic (EHA) actuators have been specifically developed for use with this type of DC power distribution system under the More Electric Aircraft initiative. This architecture also includes smart actuators, which consist of piezoelectric patches embedded or attached to the aircraft structure. The key electrical components of the power distribution system are bi-directional power converters for the conversion, control and conditioning of electrical power. One of the distinguishing features of this power distribution system is the regeneration of energy back to the electrical source from flight control actuators under certain operating conditions. This phenomenon of regeneration represents a significant departure from current power distribution systems where the power is allowed to flow only in one direction from the generator to the loads.

2.1 Architecture

The baseline power distribution system architecture was developed jointly with Lockheed Martin Control Systems (LMCS) and the following specifications were agreed upon:

1. 270 V DC power bus with a 270 V battery
2. Two Engine Starter/Generators (500 kW each) with Split/Parallel Bus
3. APU Channel Starter/Generator (200 kW)
4. Smart Load Management
5. Loads
 - Electric Actuation
 - Cargo Bay Pressurization
 - Negative Impedance Avionics Loads
 - Environmental Control System

The characteristics of aircraft electric loads in a typical commercial transport aircraft are given in Table 2.1.

Table 2.1. Characteristics of Aircraft Electric Loads

Load Group	Characteristics of the Load	Percentage of Total Load
Motor (ECS, Pumps)	<ul style="list-style-type: none"> Mainly squirrel-cage induction motor at present. Brushless DC motor with power converter will compete with the induction motor Fixed Frequency ac or dc with power converter; coarsely regulated, insensitive to waveform and transients for ac induction motor Power Flow is bidirectional 	Represents the largest portion of aircraft electrical loads
Heating	<ul style="list-style-type: none"> Constant voltage ac; constant or variable frequency, or dc; tolerate low quality, coarsely regulated power Power Flow in one direction 	Represent large segment of electric loads in commercial transports
Lighting	<ul style="list-style-type: none"> Incandescent lamps prefer low voltage ac or dc; tolerate transients and poor waveform Power flow in one direction 	
Electronics	<ul style="list-style-type: none"> Closely regulated, clean dc or ac; input power ultimately transformed to low voltage dc for utilization 	

	<ul style="list-style-type: none"> • Power Flow in one direction 	
Control	<ul style="list-style-type: none"> • Consists of relays, actuators, indicators and some lights and electronics. • Part of this load requires closely regulated power, ac or dc; the remainder can tolerate low quality power • Power Flow of actuator load is bidirectional 	Represent a small portion of the total load, usually less than 5% of the total load

Conceptually, this system is shown in Figure 2.1. The power distribution system is built around a dual 270 V/500 kW DC bus with an APU and battery backup auxiliary bus. The starter/generator units generate three-phase AC power at 110V/400Hz. The key electrical components for the regulation of the power bus are the bi-directional power converters (BDC). The BDC between a starter/generator units and the corresponding DC distribution bus serves as the bus regulator converting the 110V/400Hz three-phase AC power to tightly regulated 270V DC in the face of load and source disturbances. Other BDCs in the system process the power at the DC bus according to the requirements of the corresponding loads.

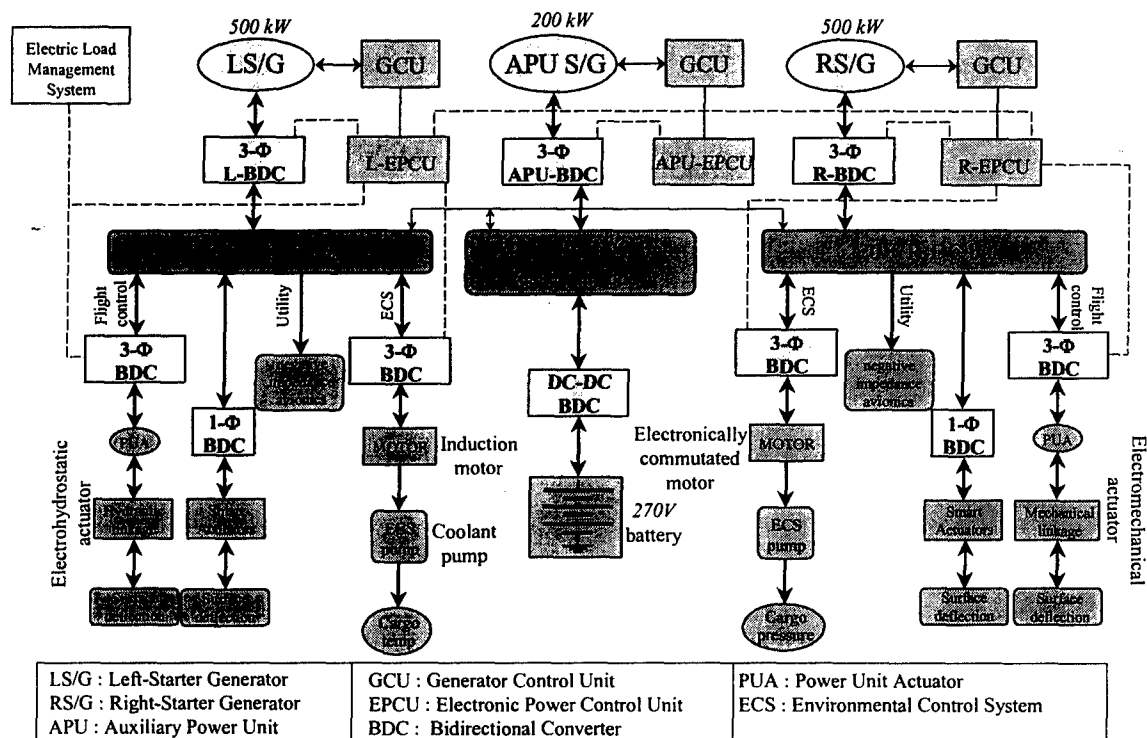


Figure 2.1. Baseline Power System Architecture

Models and parameters of EMA and EHA actuators were provided by LMCS. Also included are conventional motor loads associated with the ECS system. Novel piezoelectric actuators are also under consideration. The presence of BDCs represents a significant change in the properties of these next generation power distribution systems in that they transfer power in the forward direction from the generators to the loads and, under certain conditions, in the reverse direction back to the generators when the actuation loads operate in the regenerative mode. The origin and characteristics of this

regenerative phenomenon and the consequent effects on the power distribution system are described in the following section.

2.1.1. Actuation Loads

Electro-Hydraulic Actuators (EHAs) will drive the primary control surfaces of the aircraft. Two EHAs will drive each surface panel for the elevator, aileron, and flaperon, while three EHAs will drive the rudder. There will be a total of 15 EHAs driving the seven primary flight control surfaces. Figure 2.2 depicts the actuator location for each of the primary surfaces.

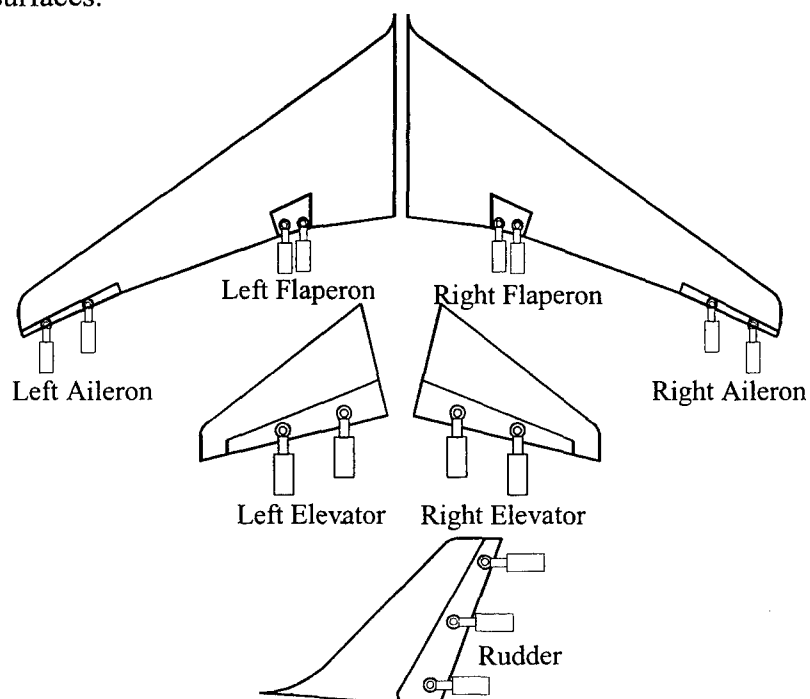


Figure 2.2 Primary Actuator Configuration, EHA

The secondary flight control surfaces consist of 14 spoiler panels. Electro-Mechanical Actuators (EMAs) will drive these panels. Each of these EMAs will have one output shaft connecting to a particular surface panel. This configuration differs from that of the primary surfaces, where two or three separate EHA RAM output shafts connect to the same control surface. Figure 2.3 depicts the secondary control surfaces and their actuator locations.

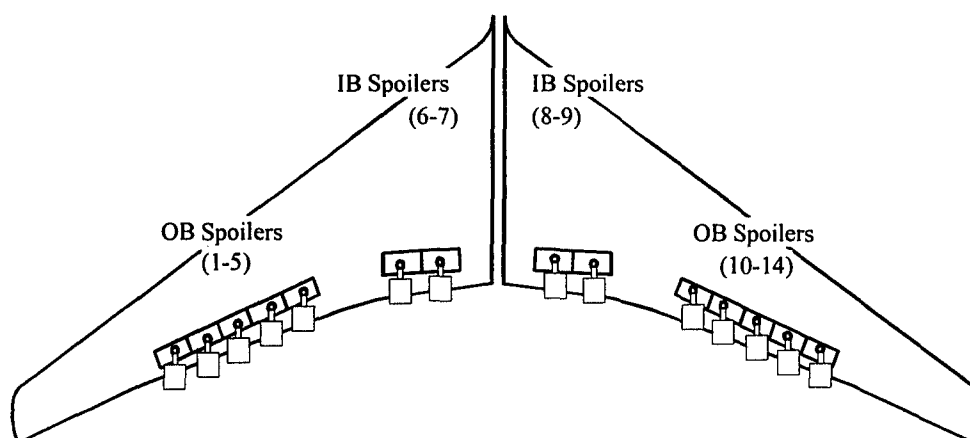


Figure 2.3. Secondary Actuator Configuration, EMA

The operating duty cycles of each of the deflection surfaces, associated hinge moments and power levels in hp are given in Table 2.2.

Table 2.2. Selected Actuator Duty Cycles for Regeneration Study

Flight Phase	Elevator (EHA) 4 x 10 hp	Aileron (EHA) 4 x 10 hp	Flaperon (EHA) 4 x 9 hp	Rudder (EHA) 3 x 15 hp	Outboard Spoiler (EMA) 4 x 6 hp	Inboard Spoiler (EMA) 10 x 6 hp	
Bypass Test on Ground	-15 to +10	+10 to -10	-10 to +10	-15 to +10			Surface Deflection (deg)
	+210 to -220	-230 to +230	-60 to +110	+1530 to -1590			Hinge Moment (ft-lbs)
Control Check on Ground	-30 to +25	+15 to -30	+36 to -10	-25 to +25			Surface Deflection (deg)
	+1670 to -1750	-90 to +90	+500 to -1120	-4740 to 4940			Hinge Moment (ft-lbs)
Roll Maneuver		+6 to -9	+24 to +36		0 to +4.5	0 to +1.0	Surface Deflection (deg)
		-990 to -350	-8520 to -10420		0 to +154	0 to -324	Hinge Moment (ft-lbs)
Yaw Maneuver		+3 to -5	+30 to -36	-5.5 to +5.5			Surface Deflection (deg)
		-790 to -510	-9610 to -10140	+17610 to -14280			Hinge Moment (ft-lbs)
Landing Rollout		-30 to 0	-10 to 0		0 to +45	0 to +60	Surface Deflection (deg)
		+230 to 0	-370 to 0		-5310 to +492	-1035 to +1482	Hinge Moment (ft-lbs)

2.2 Regenerative Energy

The operation of EMAs is briefly described in this section to identify the origin and nature of regenerative power from these flight control actuators. A block diagram of an EMA connected to the DC bus is shown in Figure 2.4.

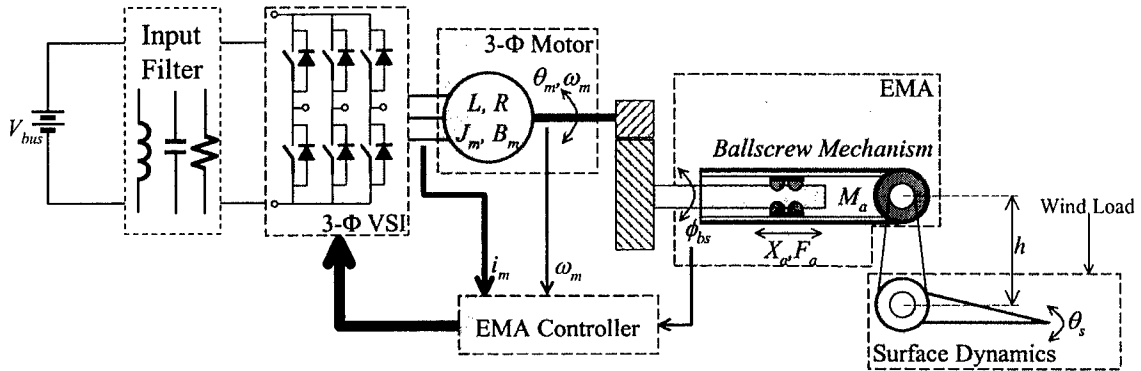


Figure 2.4. Electromechanical actuator system diagram.

The EMA is driven by a three-phase brushless DC or permanent magnet synchronous motor drive. A three-phase DC-AC inverter converts the 270V DC available on the DC bus to the three phase AC voltages required by the drive motor. The DC bus is represented by an ideal 270 V DC source. The inverter is preceded by an EMI input filter to attenuate the switching noise from reaching the DC bus. The control objective is to drive the surface in response to a deflection command θ_{ref} in the presence of a wind load disturbance. The origin of regenerative power is explained in the following.

Typical simulation results for the EMA are shown below in Figure 2.5. To start with, a surface deflection command to drive the surface from zero to a given reference position is issued. In response to this command, the drive motor accelerates the control surface to drive θ_s toward θ_{ref} . Positive values of bus current represent power drawn by the motor and negative values represent power regeneration. During the acceleration, the motor draws a large current. The motor speed steadies at its maximum allowable as the deflection increases linearly in the presence of the wind load. For the simulation results shown in Figure 2.5, the wind load is in the same direction as the motor torque. Hence, in order to maintain the linear surface deflection profile, the EMA controller makes the motor acts as a generator, absorb the energy from the wind load and siphon it back to the DC bus. This is represented by the large negative current at the DC bus.

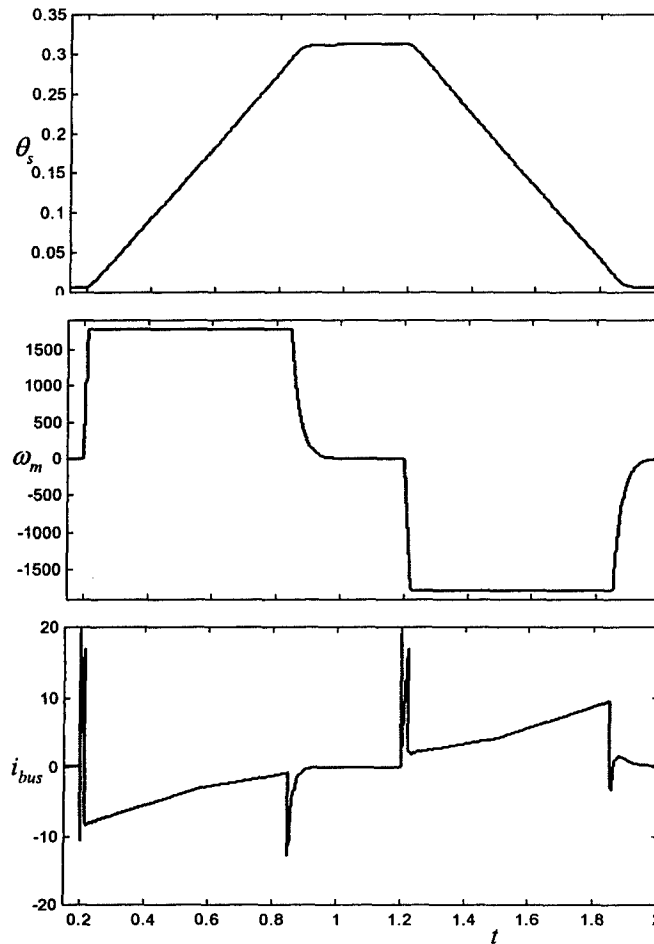


Figure 2.5. Simulation Results of the EMA

As the surface approaches its final commanded position, the motor brakes rapidly. This results in a surge of regenerative energy back to the DC bus as seen by the rapid negative excursion in the bus current. The same sequence of events is repeated when the surface is commanded to return to its original position. The motor accelerates in the opposite direction and the wind load opposes its motion thereby resulting in a large current being drawn from the bus. However, the rapid braking resulting the surge of regenerative energy toward the end of the operating cycle is the same as in the previous case. Hence, it can be seen that the DC bus sees the regeneration of energy from these actuators as (1) a slowly varying load disturbance due to the wind load and (2) a fast transient load disturbance due to the braking operation of the drive motor. Typical effects of such a disturbance on a regulated DC bus are transient voltage swings and possible instability. Simulation results are shown in Figure 2.6 to illustrate the transient voltage peaks due to regenerative process.

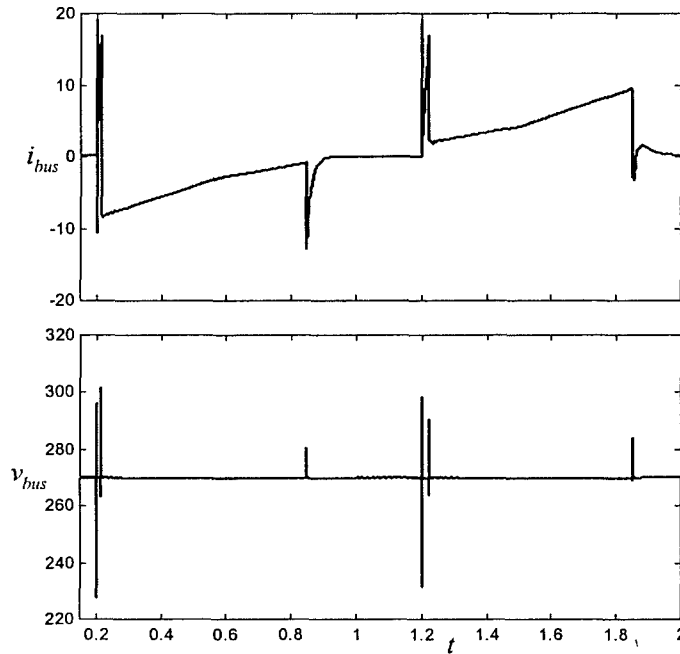


Figure 2.6. DC bus voltage response due to regeneration from EMA

It can be seen that DC bus is almost unaffected by the slow varying regenerative transient but suffers voltage spikes during the acceleration and braking operation of the motor. It is important that the magnitudes of these spikes are limited such that the safe and reliable operation of the other loads connected to the DC bus is not compromised. Limits on the transient voltage excursions on the DC bus are specified in the Mil Std-704E [1]. Hence, it is essential that the magnitude of the voltage spikes be well within these limits. In addition, if the propagation of the regenerative energy through the power distribution system can be clearly understood, methods to utilize the energy can be devised to increase the efficiency of the system.

2.2.1. Electromechanical Actuator Modeling

The EMA is driven by a three-phase brushless DC or permanent magnet synchronous motor drive (Figure 2.4). A three-phase voltage source inverter (VSI) converts the 270V DC available on the DC bus to the three phase AC voltages required by the drive motor. The motor is loaded by the actuator and the control surface as shown in Figure 2.1. The control surface is subjected to the wind load as described in the previous section. A multi-loop controller consisting of motor current, motor speed and actuator position feedback loop is used to control the three-phase inverter. The inverter-motor drive is typically modeled in rotating DQ-coordinates that are synchronized with the rotor position. This modeling approach essentially reduces the motor currents and voltages to DC and the resulting model approximately to that of a DC motor [2]. Consequently, the three-phase inverter can be represented by a single-phase bi-directional full bridge converter. The load torque on the motor is a function of the parameters of the actuator, the surface dynamics and the wind load acting on the control surface.

It was shown in the previous section that the wind load on the control surface results in a load torque that drives the motor as a generator, which in turn regenerates energy back to the DC bus when the control surface is commanded to move from zero a reference position. The wind load acting on the control surface and the position of the surface are shown in Figure 2.7. The wind load is defined as a function of the position of the control surface. The motor position and the equivalent load torque acting on the motor due to the wind load are shown in Figure 2.8.

From Figures 2.7 and 2.8, it can be seen that the dynamics of the control surface and those of the motor are sufficiently decoupled that positions of the control surface and the motor are linearly related. In addition, if the small transients at the edges of the load torque profile in Figure 2.8 are neglected, it can be assumed that the wind load on the surface and the load torque are linearly related.

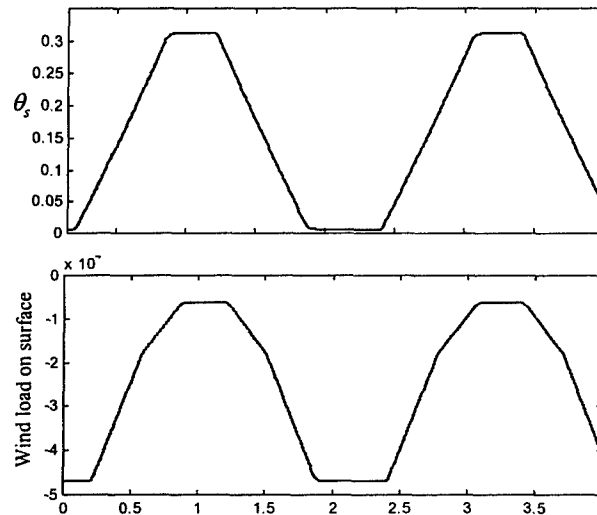


Figure 2.7. Control surface position and wind load

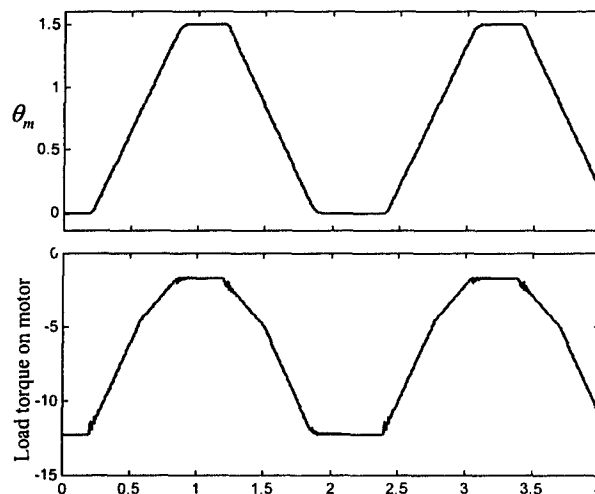


Figure 2.8. Motor position and load torque

Hence, the regenerative process can be captured with reasonable accuracy if the actuator and the dynamics of the control surface can be replaced by a time varying load torque defined as a function of the motor position. This results in considerable simplification of the model of the EMA. The controller of the EMA also needs to be replaced with an appropriate multiloop controller for the motor consisting of motor current, speed and position control loops.

A block diagram of the simplified EMA model with a separately excited DC motor with a load torque and a multiloop controller is shown in Figure 2.9.

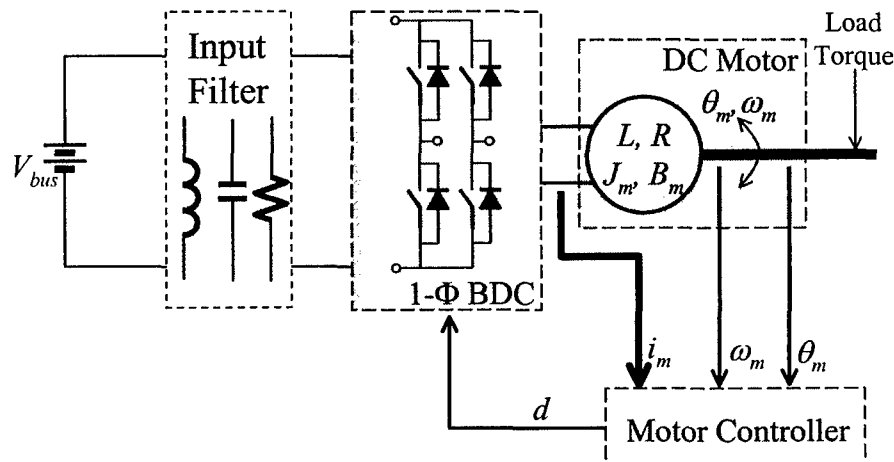


Figure 2.9. Block diagram of simplified EMA model

The dynamic equations of the separately excited DC motor are given below.

$$\begin{aligned} L_a \frac{di_a}{dt} &= -R_a i_a - K_e \omega_m + d V_{bus} \\ J \frac{d\omega_m}{dt} &= K_t i_a - B_m \omega_m - T_{ex} \\ \frac{d\theta_m}{dt} &= \omega_m \end{aligned} \quad (2.1)$$

where,

- v_a - armature voltage,
- i_a - armature current,
- ω_m - armature angular speed,
- T_{ex} - load torque applied to the motor shaft,
- L_a - armature inductance,
- R_a - armature resistance,
- J_m - armature inertia,
- B_m - friction coefficient,
- K_e - back-emf constant,
- K_t - electromagnetic torque constant,
- d - duty cycle of the drive converter.

The duty cycle d , in Equation (2.1), as a function of the armature current, motor speed and position and the load torque T_{ex} , as a function of the motor position are defined as given below:

$$\begin{aligned} d &= f(i_a, \omega_m, \theta_m) \\ T_{ex} &= g(\theta_m). \end{aligned} \quad (2.2)$$

The electrical equivalent circuit of Equation (2.1) is identical to that of a conventional bi-directional buck converter, which is representative of a majority of the bi-directional power converters in the aircraft power distribution system (Figure 2.1). An equivalent bi-directional buck converter representation of Equation (2.1) is shown in Figure 2.10.

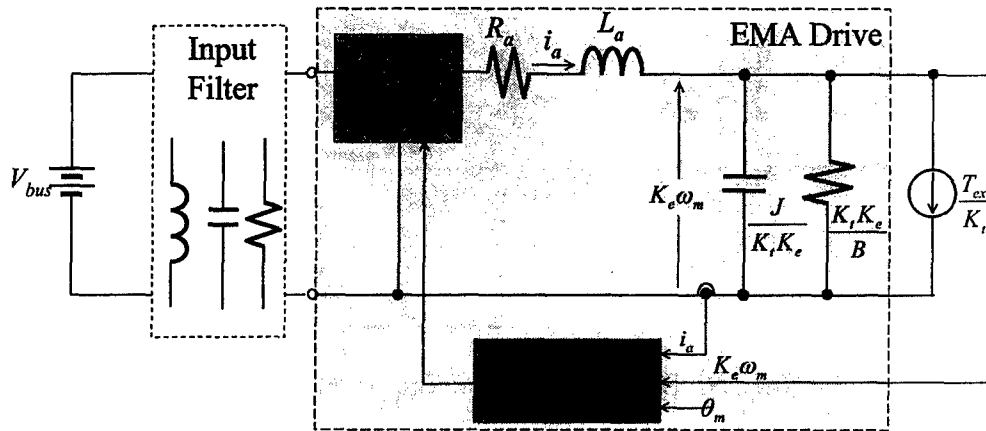


Figure 2.10. Equivalent buck converter representation of simplified EMA drive

Based on the simplifications mentioned above, the sample system is identified as a regulated DC-DC buck converter preceded by an EMI input filter. The optimization of the sample system is described in detail in the next section.

3. Optimization of a Sample System

The subject of this section is the development of an optimization methodology for the sample power system. Based on the simplifications presented in the previous section, the sample system is identified as an interconnection of a regulated DC-DC buck converter preceded by an input filter. The sample system captures the essential features of the optimization procedure. An optimization methodology is formulated for the filter. This optimization methodology is then extended to a regulated DC-DC buck converter, taking into account the increase in complexity of the converter. The procedure is then extended to the sample system to address system wide design considerations. Stability of the global system is insured, and any ill effects of regenerative power flow are minimized. In order to assess the validity of the results obtained from the optimizer, the optimal designs are compared to a filter built for a three-phase buck converter for a telecommunications

application [3]. To improve the computational efficiency of the optimization procedure, a multi-level optimization methodology is described and implemented using the filter.

3.1 Sample Power System

The sample system consists of an input filter followed by a regulated DC-DC buck converter and is shown in Figure 3.1.

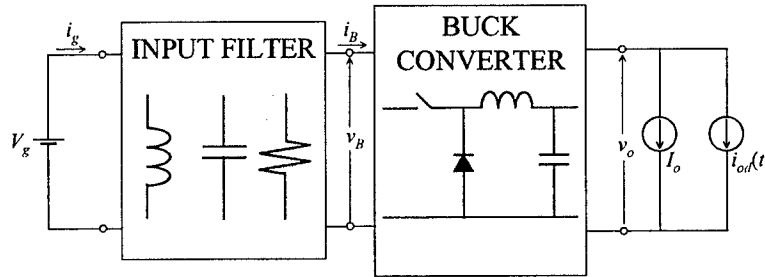


Figure 3.1. Block diagram of the sample system.

The power is supplied by the aircraft power bus, which is assumed to be a stiff DC source of $V_g = 270\text{V}$. The buck converter is representative of motor drives commonly found in aircraft power systems. The converter is loaded by a fixed DC current source I_o (to represent the average power drawn).

Switching converters, due to their high frequency switching behavior, inject an appreciable amount of high frequency noise into the system. This high frequency noise results in what is known as Electromagnetic Interference (EMI) between the converter and other interconnected systems. Input filters are added at the front end of these converters in order to prevent the switching noise from entering the source subsystem. Stringent EMI specifications exist that impose upper bounds on the input filter transfer characteristics at different frequency ranges as dictated by the specific application.

To account for the effect of regenerative power flow, the load disturbance $i_{od}(t)$ indicated in Figure 3.1 is represented by a pulse load with duration T_p as shown in Figure 3.2.

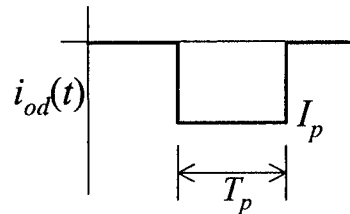


Figure 3.2. Load disturbance profile

The nominal operating conditions for the sample system are given in Table 3.1. The goal of the optimization is to design these two subsystems such that: 1) each subsystem meets its own performance specifications (to be described below), 2) the overall system is stable within prescribed stability bounds, 3) the effect of the transient disturbance source $i_{od}(t)$

at the output of the buck converter on the input voltage of the converter is limited, and 4) the overall weight of the system is minimized.

Table 3.1. Nominal Operating Conditions for Sample System

Variable	Description	Value
V_g	Filter input voltage	270 V
V_B	Filter output voltage	270 V
V_o	Converter output voltage	100 V
D	Converter duty cycle	V_o/V_g
I_o	Converter average load current	15A
I_B	Converter input current	$I_o(V_o/V_g)$
I_p	Peak value of pulse disturbance	-20 A
T_p	Duration of pulse disturbance	10 ms

The modeling of the input filter, buck converter and the inductor is described in the next section. The formulation of the optimization problems for the input filter, buck converter and the integrated sample system are then explained in the subsequent sections.

3.2 Model Development

The development of the models for the subsystems in the sample system is described in this section.

3.2.1. Input Filter

The schematic of the input filter used in the sample system is shown in Figure 3.3. The DC bus is represented by an ideal DC voltage source of 270 V. The constant current source accounts for the nominal current load of the buck converter in the sample system discussed in the last section. The time varying current source accounts for the regenerative energy from the buck converter. This current source represents the dynamic coupling between various blocks of the power distribution system.

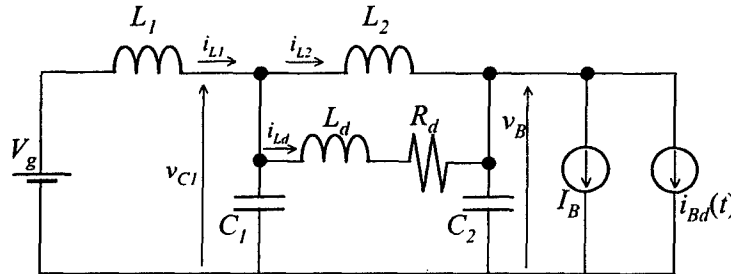


Figure 3.3. Schematic of input filter used in sample system.

Using network analysis, the state equations of the input filter can be obtained in a straightforward manner. The state equations are given by:

$$\begin{aligned}
\frac{di_{L1}}{dt} &= \frac{1}{L_1}(V_g - v_{C1}) \\
\frac{di_{L2}}{dt} &= \frac{1}{L_2}(v_{C1} - v_B) \\
\frac{di_{Ld}}{dt} &= \frac{1}{L_d}(v_{C1} - v_B - R_d i_{Ld}) \\
\frac{dv_{C1}}{dt} &= \frac{1}{C_1}(i_{L1} - i_{L2} - i_{Ld}) \\
\frac{dv_B}{dt} &= \frac{1}{C_2}(i_{L2} + i_{Ld} - I_B - i_{Bd}).
\end{aligned} \tag{3.1}$$

3.2.2. Buck Converter

The schematic of the DC-DC buck converter is shown in Figure 3.4a. The switch-diode combination highlighted in Figure 3.4a is replaced by a single-pole double throw switch, known as the PWM switch, as shown in Figure 3.4b. The switch S is turned on (switch at position a in Figure 3.4b) and off (switch at position b in Figure 3.4b) at a fixed frequency to transform the input voltage v_B to a periodic square wave voltage v_L . The voltage v_L is then filtered by the L - C filter to obtain the output voltage v_o . The average value of the output voltage is varied by modulating the time interval the switch S is kept on.

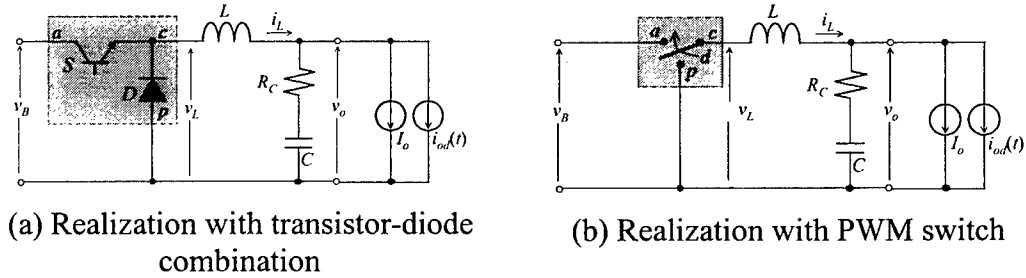


Figure 3.4. Schematic of DC-DC Buck converter

An average model of the buck converter, which neglects the switching ripple in the currents and voltages, is used [4]. The average model of the buck converter replaces the switch-diode combination in the switch model (Figure 3.4a) by controlled current and voltage sources. A multi-loop controller consisting of an inner inductor current loop and an outer voltage loop is used for the regulation of the output voltage to a fixed reference. Since average models of the converters are in general nonlinear, small signal models linearized around an operating point are derived. These linearized models are then used for the design of the current and voltage controllers. As already mentioned, the input voltage v_B , is represented by an ideal voltage source of 270V. The average model of the buck converter along with a block diagram of the controller is shown in Figure 3.5.

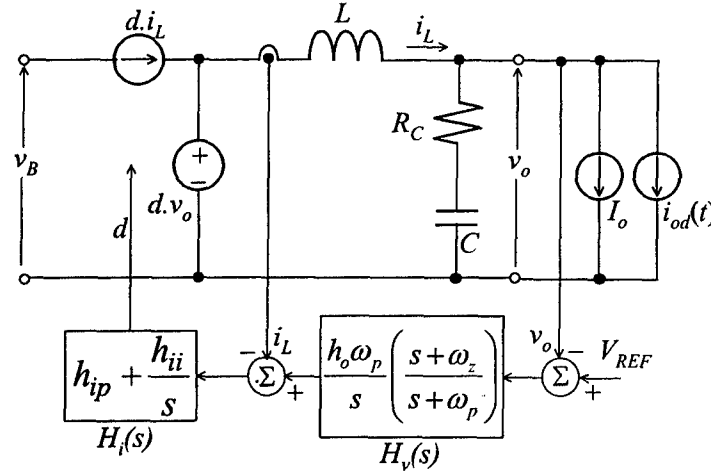


Figure 3.5. Average model of buck converter with inductor current and output voltage compensators

The state equations of the closed loop system shown in Figure 3.5 can be written as:

$$\begin{aligned}
 \frac{di_L}{dt} &= \frac{1}{L} (d v_B - v_C - R_C (i_L - I_o - i_{od})) \\
 \frac{dv_C}{dt} &= \frac{1}{C} (i_L - I_o - i_{od}) \\
 \frac{dv_{oc1}}{dt} &= \omega_Z (v_{oc2} - v_{oc1}) \\
 \frac{dv_{oc2}}{dt} &= h_o \omega_p (v_o - V_{REF}) - \omega_p (v_{oc2} - v_{oc1}) \\
 \frac{di_{Lc}}{dt} &= h_{ii} (V_{REF} - v_{oc2} - i_L),
 \end{aligned} \tag{3.2}$$

where d is the duty cycle of the converter given by:

$$d = i_{Lc} + h_{ip} (V_{REF} - v_{oc2} - i_L). \tag{3.3}$$

In Equations (3.2) and (3.3), the states v_{oc1} and v_{oc2} represent the state variables of the voltage controller and i_{Lc} represents the state variable of the current controller. The average model is nonlinear due to the product of the duty cycle d , which is a function of the state variables, and the input voltage v_B .

3.2.3. Inductor Model

The design of the inductors in the sample system includes their physical design in addition to just the determination of the inductance values. The inductors are assumed to use typical EE cores as shown in Figure 3.6.

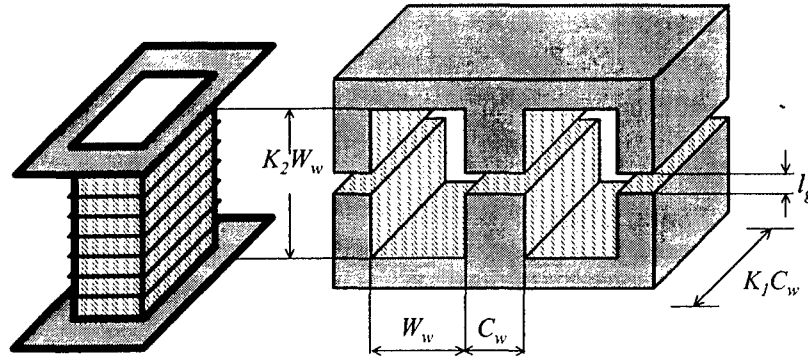


Figure 3.6. EE Core, bobbin and relevant dimensions

The quantities K_1 and K_2 shown in Figure 3.6 are assumed to be fixed and represent the aspect ratios of the center leg and the window, respectively. The other physical variables governing the design of each inductor are listed in Table 3.2. Note that these variables include parameters related to the windings and wire size.

Table 3.2. Physical variables associated with inductor design

Variable	Description
n	Number of turns
A_{cp}	Cross sectional area of
C_w	Center leg width
W_w	Window width
l_g	Airgap length

The inductance as a function of these physical variables is given by:

$$L = \frac{\mu_o K_1 C_w^2 n^2}{l_g} \quad (3.4)$$

3.3 Optimization of the Input Filter

The optimization of the input filter is described in this section. The identification of the design variables, definition of the constraints and the objective function are explained in detail.

3.3.1. Design Variables

Design variables for the input filter shown in Figure 3.3 include the capacitance values C_1 and C_2 , and resistance value R_d , and the a set of variables describing each of the three inductors. The complete set of input filter design variables is listed in Table 3.3.

3.3.2. Constraints

The input filter design constraints are subdivided into performance, stability and physical constraints as explained in the following subsections.

Performance Constraints

Performance constraints are further classified as frequency domain and time domain constraints.

Table 3.3. Design Variables for the Input Filter

Design Variable	Description
C_1	Filter capacitance
C_2	Filter capacitance
R_d	Filter resistance
n_d	Number of turns for L_d
A_{cpd}	Cross sectional area of winding for L_d
C_{wd}	Center leg width for L_d
W_{wd}	Window width for L_d
l_{gd}	Airgap length for L_d
n_1	Number of turns for L_1
A_{cp1}	Cross sectional area of winding for L_1
C_{w1}	Center leg width for L_1
W_{w1}	Window width for L_1
l_{g1}	Airgap length for L_1
n_2	Number of turns for L_2
A_{cp2}	Cross sectional area of winding for L_2
C_{w2}	Center leg width for L_2
W_{w2}	Window width for L_2
l_{g2}	Airgap length for L_2

Frequency domain constraints

As mentioned earlier, input filters are added at the front end of switching converters in order to prevent the high frequency noise from entering the source subsystem. Stringent EMI specifications exist that impose upper bounds on the input filter transfer characteristics at different frequency ranges as dictated by the specific application.

The EMI specifications on the input filter are typically translated into frequency domain constraints on the forward voltage transfer function of the input filter. This transfer function between the input and output voltage of the input filter in Figure 3.3 is given by:

$$\frac{V_B(j\omega)}{V_g(j\omega)} = A_v(j\omega). \quad (3.5)$$

The frequency response of the forward voltage transfer function for a typical input filter is shown in Figure 3.7.

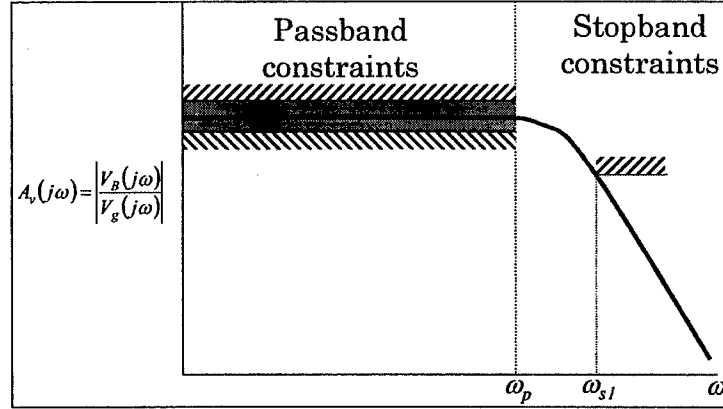


Figure 3.7. Definition of frequency domain performance specifications for the input filter

Two types of constraints exist for the frequency response function: low frequency passband constraints and high frequency stopband constraints. The transfer of power from the source to the load occurs almost entirely in the low frequency region. Hence, the input filter needs to be designed to have near unity gain in the passband. These passband constraints are defined in terms of upper and lower bounds on the input-output transfer function of the filter up to a passband frequency, ω_p , as shown in Figure 3.7. For the present problem, the passband constraint is defined as:

$$-1 \text{ dB} \leq |A_v(j\omega)| \leq 6 \text{ dB} \text{ for } 0 \leq \omega \leq \omega_p = 2\pi \cdot 5 \times 10^3 \text{ rad/sec.} \quad (3.6)$$

In addition, the filter must attenuate the high frequency switching noise according to given EMI specifications. Therefore, above a certain frequency, ω_{s1} , shown in Figure 3.7 the frequency response function must be below a given value.

For the present case, the frequency boundaries for the stopband and passband constraints were chosen based on the assumption that the converter to which the filter is attached has a nominal switching frequency of 100 kHz. For the present problem, the stopband constraint is:

$$|A_v(j\omega)| < -60 \text{ dB for } \omega > \omega_{s1} = 2\pi \cdot 50 \times 10^3 \text{ rad/sec.} \quad (3.7)$$

Time Domain Constraints

The time domain constraints account for the dynamic coupling between the various components of the power distribution system. In the sample system shown in Figure 3.1,

a pulse current load at the output of the buck converter develops a transient current disturbance $i_{Bd}(t)$. This transient current represents the regenerative energy from the actuator. This transient current will cause an undesirable voltage swing at the output of the filter. A time domain constraint on the output voltage is imposed to limit the disturbance. This constraint is an upper bound on the maximum transient excursion of the output voltage of the filter as indicated in Figure 3.8. For this work, the maximum transient voltage excursion limit is:

$$\Delta v_B < 20 \text{ V.} \quad (3.8)$$

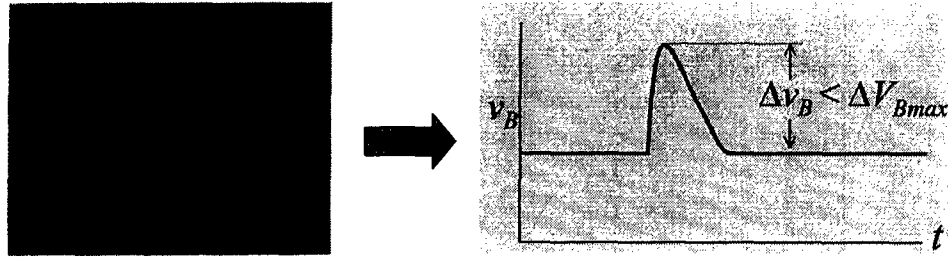


Figure 3.8. Time domain constraint for input filter

Stability Constraints

Because the input filter consists only of passive components it is generally internally stable (with all its eigenvalues in the left half of the s -plane). However, the input filter is notorious for causing instability due to its interaction with a regulated converter. It can be shown that a regulated power converter can have a negative input impedance that might cause the interconnected system to become unstable. Constraints that guarantee stability of the interconnected system are defined in the frequency domain using the Middlebrook impedance ratio criterion [5].

Figure 3.9 shows a generic subsystem interface formed by connecting two electrical subsystems. A standard two-port model as shown in Figure 3.9 represents each subsystem.

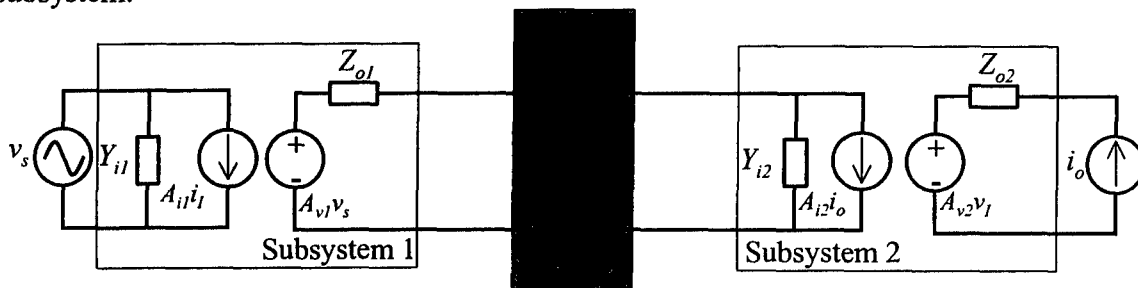


Figure 3.9. Generic Subsystem Interface

The impedance ratio criterion guarantees stability and minimal interaction between the interconnected subsystems by that the magnitude of the output impedance of subsystem 1 (filter) must everywhere be less than the input impedance of subsystem 2 (converter). The input filter schematic showing only the relevant impedances is shown in Figure 3.10.

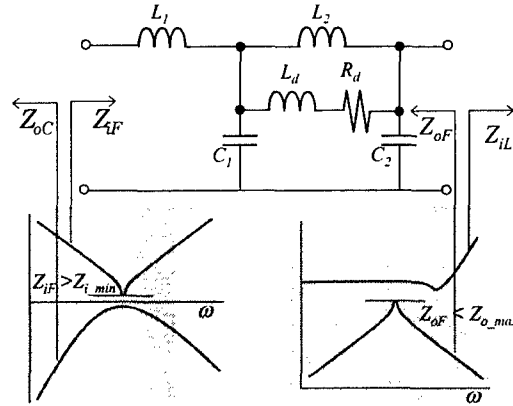


Figure 3.10. Impedances at the terminals of the input filter.

The impedance looking out of the output terminals of the filter is designated Z_{iL} and is the input impedance of the buck converter. For the filter optimization problem, this impedance is considered to be fixed and given. Applying the impedance ratio criteria, the output impedance of the filter Z_{oF} , which depends on the design parameters, must be less than the impedance Z_{iL} . Since Z_{iL} is given, sufficient separation between these two impedances can be enforced by requiring that the upper bound of the output impedance of the filter satisfy:

$$Z_{o_max} = \max_{\omega} (|Z_{oF}(j\omega)|) < 15 \text{ dB} < Z_{iL}. \quad (3.9)$$

Similar reasoning is applied to the interaction between the filter and the DC bus:

$$Z_{i_min} = \min_{\omega} (|Z_{iF}(j\omega)|) > 3 \text{ dB}. \quad (3.10)$$

Physical Constraints

These constraints are defined to guarantee physically meaningful dimensions for the core and windings used in the inductor (Figure 3.6). They are defined as follows [6]:

- The widths of the center leg C_w , and of the window W_w are not allowed to be less than 1 mm to ensure sufficient mechanical strength of the core.
- In order to ensure sufficient mechanical strength for the winding, the copper wire used cannot be greater than 30AWG, which is equivalent to a cross-sectional area of $7.29 \times 10^{-8} \text{ m}^2$.
- The number of turns in the inductor cannot be less than one and must be an integer.
- The current density in the windings of the inductor cannot be greater than maximum allowable current density for copper.

- The available window area of the EE core must be large enough to accommodate the windings of the inductor and the bobbin as shown in Figure 3.6. Through simple geometry, this constraint translates to:

$$K_2 W_w^2 > \left(\frac{n A_{cp}}{F_w} + W_{bob} K_2 W_w \right), \quad (3.11)$$

where

$$\begin{aligned} F_w, \text{window fill factor} &= 0.4 \\ W_{bob}, \text{bobbin thickness} &= 1.5 \text{ mm} \\ K_2, \text{Window area aspect ratio} &= 3. \end{aligned} \quad (3.12)$$

- The dimensions of the inductor should be such that the maximum allowable saturation flux density for a ferrite core material, $B = 0.3 \text{ T}$, is not exceeded.

$$B_{sp} > \frac{LI_{L(pk)}}{n K_1 C_w^2} \quad (3.13)$$

Where

$$\begin{aligned} B_{sp}, \text{saturation flux density of ferrite} &= 0.3 \text{ T} \\ K_1, \text{center leg aspect ratio} &= 1.5 \end{aligned} \quad (3.14)$$

3.3.3. Objective Function

The objective function is the weight of the input filter. The total filter weight is the sum of the weights of the inductors, capacitors, and resistors:

$$J = W_L + W_C + W_R. \quad (3.15)$$

The weight of an inductor is determined as the sum of the weights of iron and copper used in the core and windings, respectively:

$$W_L = W_{fe} + W_{cu}. \quad (3.16)$$

From Figure 3.6, the weight of the copper can be obtained as:

$$W_{cu} = D_{cu} Vol_{cu}, \quad (3.17)$$

where

$$D_{cu} = 8900 \text{kg/m}^3 \quad (3.18)$$

$$Vol_{cu} = MLT \cdot n \cdot A_{cp}$$

$$MLT = 2F_c C_w (1 + K_1), \text{ mean length/turn,}$$

$$F_c = 1.9, \text{ winding pitch factor.}$$

Similarly, the weight of the iron used in the EE core is given by (Figure 3.6):

$$W_{fe} = D_{fe} Vol_{fe}, \quad (3.19)$$

where

$$D_{fe} = 7800 \text{kg/m}^3 \quad (3.20)$$

$$Vol_{fe} = Z_p A_p$$

$$Z_p = 2(1 + K_2)W_w + \frac{\pi}{2}C_w, \text{ magnetic path length}$$

$$A_p = K_1 C_w^2, \text{ Area of cross section of center leg.}$$

The weight of a capacitor is approximated as a function of the energy stored in it and is given by:

$$W_C = \alpha_C C V_C^2. \quad (3.21)$$

The constant α_C was obtained from manufacturer data sheets. Finally, the weight of the resistor is approximated as a function of the energy dissipated in it and is given by:

$$W_R = \int_0^t R \cdot i_R^2 \cdot dt. \quad (3.22)$$

3.3.4. Optimization Results

Optimization was performed using the VisualDOC optimization software [7] using the Modified Method of Feasible Directions algorithm [8]. The transient peak voltage constraint was enforced by imposing an upper bound constraint on the maximum output voltage obtained from a time domain simulation of the filter response. Constraint derivatives were computed using finite differences. Depending on the initial design used to start the optimization iterations, convergence was obtained within approximately 200 function evaluations (here a single function evaluation includes both a time domain simulation and frequency domain computations). The optimizations were achieved in approximately 40 minutes on a 500 MHz Pentium III PC.

To assess the validity of the results obtained from the optimizer, the optimal designs were compared to a filter built for a three-phase buck converter for a telecommunications application [3]. This hardware design, developed without the use of the optimizer, is referred to here as the nominal design. In addition to providing weight savings in comparison to the nominal design, the optimal design methodology is automated and can considerably reduce design cycle time.

The optimization algorithm used for the present work belongs to a class of optimization algorithms termed “gradient based methods”. In order to begin the optimization process, these algorithms are typically provided with an initial design. Once an initial design is specified, gradients of the objective function and constraints are computed with respect to the design variables to compute a search direction in the design space. Next, the design space is searched along the computed direction so as to minimize the objective function while satisfying all the constraints. Gradients are then recomputed at the new design point, and the process continues until no further improvements are possible. If the design space contains several local minima, there is a possibility that a gradient-based optimizer may be trapped by a local minimum, and the answer will depend on the selection of the initial design point. In order to increase the probability of finding the point with the smallest objective function value (the global minimum), it is customary to execute the optimization algorithm starting from several different initial designs. In the present work, it was found that there were local minima in the design space, although in all cases studied, even the local minima were lighter than the nominal design. The results reported here correspond to the best designs found during the course of the study and are likely to be the globally optimum design.

The physical variables for the filter inductors values for the nominal and optimal designs are given in Table 3.4. The nominal and optimum component values and the objective function are provided in Table 3.5. Response quantities of interest for the nominal and optimal designs are given in Table 3.6. Response quantities that are at their upper or lower bounds are listed in bold face type. All the physical constraints on the inductor designs were active for the optimal design. The other active constraints for the optimized design were the lower bound constraint on the input impedance Z_{iF} and the stopband constraint on the input-output transfer function. Note that the peak voltage constraint was violated for the nominal design.

Table 3.4. Physical variables of the filter inductors

Variable	Nominal value	Optimal value
n_1	29.53	19.94
A_{cp1}	$0.630 \times 10^{-5} \text{ m}^2$	$0.530 \times 10^{-5} \text{ m}^2$
C_{w1}	$0.751 \times 10^{-2} \text{ m}$	$0.484 \times 10^{-2} \text{ m}$
W_{w1}	$0.682 \times 10^{-2} \text{ m}$	$1.017 \times 10^{-2} \text{ m}$
l_{g1}	$1.16 \times 10^{-3} \text{ m}$	$0.664 \times 10^{-3} \text{ m}$
n_2	45.98	42.77
A_{cp2}	$0.448 \times 10^{-5} \text{ m}^2$	$0.382 \times 10^{-5} \text{ m}^2$
C_{w2}	$0.985 \times 10^{-2} \text{ m}$	$0.939 \times 10^{-2} \text{ m}$

W_{w2}	$1.33 \times 10^{-2} \text{ m}$	$1.244 \times 10^{-2} \text{ m}$
l_{g2}	$1.29 \times 10^{-3} \text{ m}$	$1.03 \times 10^{-3} \text{ m}$
n_d	16.06	7.79
A_{cpd}	$0.349 \times 10^{-5} \text{ m}^2$	$0.359 \times 10^{-5} \text{ m}^2$
C_{wd}	$0.396 \times 10^{-2} \text{ m}$	$0.585 \times 10^{-2} \text{ m}$
W_{wd}	$0.978 \times 10^{-2} \text{ m}$	$0.564 \times 10^{-2} \text{ m}$
l_{gd}	$0.355 \times 10^{-3} \text{ m}$	$0.176 \times 10^{-3} \text{ m}$

Table 3.5. Nominal and Optimal Filter Designs

Variable	Nominal value	Optimal value
L_1	80 μH	26.49 μH
L_2	300 μH	296.77 μH
L_d	21.5 μH	22.29 μH
C_1	5 μF	7.19 μF
C_2	18.8 μF	27.70 μF
R_d	3 Ω	2.23 Ω
Weight	0.5279 kg	0.3692 kg

Table 3.6. Response quantities for nominal and optimal designs of input filter

Response variable	Nominal	Optimal
Minimum input	3.81* dB	2.99 dB
Maximum output	15.39 dB	9.11 dB
Passband maximum	5.63 dB	3.18 dB
Passband minimum	$6.55 \times 10^{-6} \text{ dB}$	7.94390×10^{-6}
Stopband maximum	-63.13dB	-60.00 dB
Peak output voltage	21.97* V	13.75 dB

*violated constraint

To compare the optimization results with the hardware (nominal) design, several additional optimization runs were performed corresponding to different values of the lower bound constraint Z_{i_min} on the input impedance. The resulting family of optimal designs is compared to the nominal design in Figure 3.11. For the same value (3.8 dB) of Z_{i_min} , the optimal design is 25% lighter than the nominal design. For the same weight, on the other hand, the minimum input impedance for the optimized design is approximately 47% higher than for the nominal design.

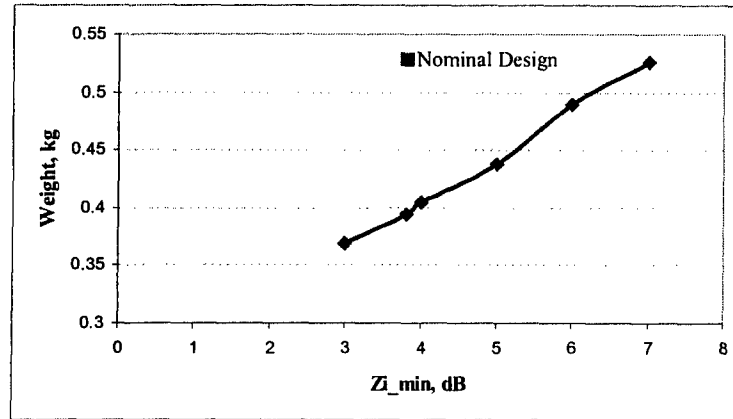


Figure 3.11. Weight of optimal designs as a function of the lower bound on the input impedance

3.4 Optimization of the Buck Converter

The formulation of the optimization problem for the design of the buck converter is considered in this section. The approach to this subsystem is very similar to the approach taken for the filter, particularly the interaction constraints. Some additional constraints are required for the converter, however, because of its internal complexity.

3.4.1. Design Variables

Design variables for the buck converter include the physical parameters governing the design of the inductor, the capacitance C , the switching frequency of the converter f_s , and a set of parameters governing the feedback controller (h_o , ω_z , ω_p , h_{ip} , and h_{ii}). As with the filter, it is assumed that an EE core is used for the inductor (Figure 3.6). Table 3.7 contains a list of all design variables used for the buck converter.

Table 3.7. Design Variables for buck converter

Design Variable	Description
n	Number of turns for L
A_{cp}	CSA of winding for L
C_w	Center leg width for L
W_w	Window width for L
l_g	Airgap length for L
C	Capacitance
f_s	Switching frequency of buck converter
h_o	Voltage controller gain
ω_z	Voltage controller zero
ω_p	Voltage controller pole
h_{ip}	Current controller proportional gain
h_{ii}	Current controller integral gain

3.4.2. Constraints

The performance, stability and physical constraints on the design of the buck converter are described in the following paragraphs.

Performance Constraints

Frequency Domain Constraints

Two frequency domain constraints are imposed on the buck converter. The average model of the closed loop converter is linearized around the nominal operating point to yield a small signal linear model. This linear model is then used for the determination for the transfer functions on which the frequency domain constraints are imposed. These constraints can be explained with the help of the simplified block diagram of the closed loop buck converter shown in Figure 3.12.

Frequency domain constraints for the buck converter are imposed as upper bounds on the maximum magnitude of the transfer function between the input and output voltage and the voltage loop gain crossover frequency.

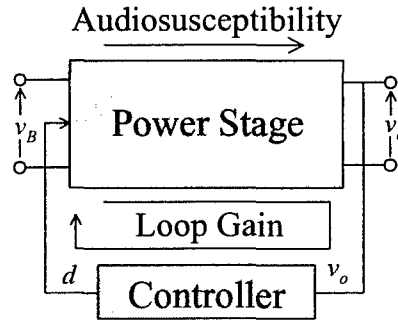
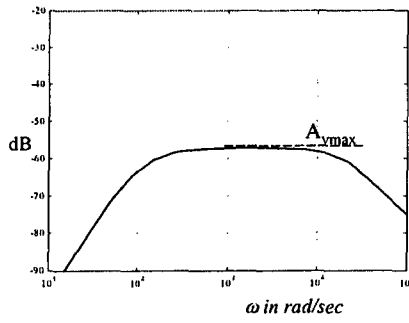


Figure 3.12. Simplified block diagram of closed loop buck converter

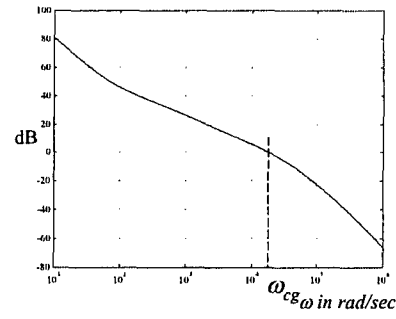
The transfer function between the input voltage v_B and the output voltage v_o is called the audiosusceptibility of the converter. A typical transfer function is shown in Figure 3.13a. An upper bound is imposed on this transfer function in order to guarantee sufficient rejection of any audio frequency disturbance introduced at the input voltage. This constraint can be stated as:

$$A_v = \max_{\omega} \left| \frac{V_o(j\omega)}{V_B(j\omega)} \right| < -30 \text{ dB.} \quad (3.23)$$

The second constraint is imposed on the loop gain. The loop gain is the open loop transfer function between the output voltage error $V_{ref} - v_o$, and the output voltage v_o (Figure 3.50). The characteristics of the loop gain transfer function determine the bandwidth and the stability margins of the closed loop system. A typical curve is shown in Figure 3.13b.



(a) Audiosusceptibility



(b) Voltage Loop Gain

Figure 3.13. Frequency Domain Constraints for the buck converter

An upper bound constraint is also imposed on the crossover frequency of the voltage loop gain, ω_{cg} in order to limit the bandwidth of the converter. (This relationship can be found in classical control theory.) The bound on the bandwidth of the converter will guarantee that the switching frequency ripple in the inductor current and the output voltage are sufficiently attenuated before they propagate through the controller. The frequency ω_{cg} is chosen to be sufficiently less than half the switching frequency. For the present problem this upper bound is given by:

$$\omega_{cg} < \frac{2\pi f_s}{5}. \quad (3.24)$$

Additional constraints will be imposed on the voltage loop gain for stability reasons as discussed below.

Time Domain Constraints

Time domain constraints are introduced to account for transients in the voltages in the converter due to transient disturbances at the output terminals of the converter. These constraints are identical to those developed for the filter in Section 3.3. A pulse load disturbance represents the transient disturbance at the output of the buck converter. For the optimized design of the buck converter, a fixed resistance is included in series with an ideal voltage source as shown in Figure 3.14.

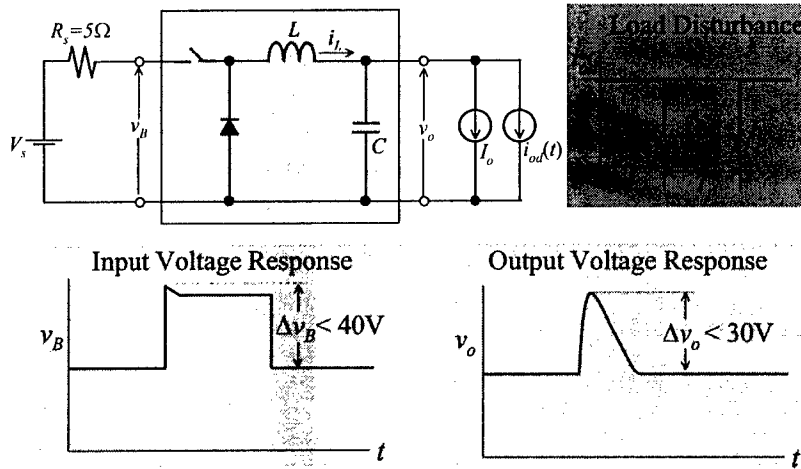


Figure 3.14. Time domain constraints for the converter

This fixed resistance was included to represent the effect of the input filter when imposing the impedance ratio criteria for stability. The resistance value was chosen to be equal to 5Ω , which was the maximum output impedance (15 dB) of the nominal input filter design (Table 3.6) and the voltage variations at the input and output of the converter were constrained as:

$$v_B < 40V, \Delta v_o < 30V. \quad (3.25)$$

Stability Constraints

Like the filter, the buck converter must satisfy external stability constraints, so that the entire sample system in Figure 3.1 is stable. In addition, because of the presence of the internal control loop, the converter must be internally stable.

Internal Stability Constraints

The design of the feedback controller for the buck converter (Figure 3.5) must guarantee stability and robustness of the closed loop system in the presence of disturbances in the load current and source voltage. These stability constraints are defined as bounds on the gain margin, g_m , and phase margin, ϕ_m of the closed loop. From classical control theory [9], positive values of phase margin and gain margin are necessary conditions for stability. In order to guarantee sufficient robustness of the closed loop, lower bounds are imposed on these values. These values are widely used in the design of switching converters. These constraints translate into constraints on the voltage loop gain in Figure 3.13b.

$$\begin{aligned} \phi_m &> 60^\circ \\ g_m &> 3 \text{ dB} \end{aligned} \quad (3.26)$$

External Stability Constraints

External stability constraints are used to guarantee stability of the interconnected system after adding the input filter. As for the input filter, they are defined using the impedance ratio criterion with the input and output impedances appropriately defined. An upper bound is imposed on the maximum magnitude of the output impedance, Z_{o_max} , and a lower bound on the minimum magnitude of the input impedance, Z_{i_min} , of the closed loop converter. Using the notation of Section 3.3, these bounds are given as:

$$\begin{aligned} Z_{i_min} &= \min_{\omega} (|Z_{iB}(j\omega)|) > 30 \text{ dB} \\ Z_{o_max} &= \max_{\omega} (|Z_{oB}(j\omega)|) < 20 \text{ dB.} \end{aligned} \quad (3.27)$$

Since the output impedance of the filter is set to 15dB in Equation (3.9), the first of these two constraints ensures that there is at least a 15 dB separation between the output impedance of the filter and the input impedance of the converter. (See Figure 3.10.) The upper bound of the output impedance is set to ensure sufficient separation from the minimum input impedance of the load to the buck converter. Since the load is represented by an ideal current source (which has an infinite input impedance), the upper bound of the output impedance was arbitrarily chosen.

Physical Constraints

In addition to the physical constraints, which guarantee physically meaningful dimensions for the core and winding of the inductors similar to the input filter, constraints are also imposed to limit the switching ripple in the inductor currents and the capacitor voltages. Although the average model for the buck converter is used for the analysis, expressions for switching ripple in terms of average quantities are readily available.

Inductor Current Ripple

It is generally required that the peak-to-peak inductor current ripple be less than 10% of the nominal inductor current. From Figure 3.50, the inductor current ripple can be obtained as [4]:

$$\Delta I_L = \frac{(1-D) V_o}{f_s L}. \quad (3.28)$$

If $P_o = V_o I_{L(nom)}$, is the nominal power rating of the converter, a lower bound on the inductance based on the switching ripple is then determined as follows:

$$\Delta I_L < 0.1 I_{L(nom)} \Rightarrow L > 10 \left(\frac{V_o^2}{P_o} \right) \left(\frac{1-D}{f_s} \right). \quad (3.29)$$

Output Voltage Ripple

The ripple in the output voltage is generally limited to be less than 1% of the average value. It is assumed that the capacitor absorbs the ripple component of the inductor current. The peak-to-peak output voltage ripple constraint is derived as follows [4]:

$$\Delta V_o = \frac{1}{8C} \frac{\Delta I_L}{f_s} + \Delta I_L R_C. \quad (3.30)$$

Substituting for the inductor current ripple from Equation (3.29), the output voltage ripple constraint is:

$$\Delta V_o = \frac{1}{8LC} \frac{(1-D)}{f_s} V_o + \frac{(1-D)}{Lf_s} V_o R_C = \frac{1}{LC} \frac{(1-D)}{f_s^2} V_o \left(\frac{1}{8} + \tau f_s \right) < 0.01 V_o \quad (3.31)$$

$$\Delta V_o < 0.01 V_o \Rightarrow LC > 100 \cdot \left(\frac{1-D}{f_s^2} \right) \left(\frac{1}{8} + \tau f_s \right),$$

where $\tau = R_C C$ is the ESR time constant of the capacitor. If the voltage ripple is limited to be less than 1% of the average value, then the following constraint is obtained.

$$LC > 100 \cdot \left(\frac{1-D}{f_s^2} \right) \left(\frac{1}{8} + \tau f_s \right). \quad (3.32)$$

3.4.3. Objective Function

The objective function is the weight of the converter, which is calculated according to Equation (3.15) as the sum of the weights of the inductors and the capacitors. The controller is not assumed to contribute significantly to the weight of the converter and hence is neglected in the determination of the weight.

3.4.4. Optimization Results

As was the case for the input filter problem, the VisualDOC optimization software [7] using the Modified Method of Feasible Directions algorithm [8] were used to obtain an optimized design. The transient peak voltage constraint was enforced by imposing an upper bound constraint on the maximum output voltage obtained from a time domain simulation of the filter response. Constraint derivatives were computed using finite differences. Converged optimal designs were obtained in approximately 300 function evaluations (a single function evaluation includes both a time domain simulation and frequency domain computations). The optimizations were achieved in approximately 20 minutes on a 500 MHz Pentium III PC. The optimal design for the buck converter was generally insensitive to the initial design.

To assess the validity of the results obtained from the optimizer, the optimal designs were compared to a three-phase buck converter for a telecommunications application

[3]. This hardware design, developed without the use of the optimizer, is referred to as the nominal design. The physical variables for the filter are given in Table 3.8.

Table 3.8. Physical variables for the inductor in the buck converter

Variable	Nominal value	Optimal value
n	55	55.55
A_{cp}	$1.1 \times 10^{-5} \text{ m}^2$	$1.05 \times 10^{-5} \text{ m}^2$
C_w	$1.65 \times 10^{-2} \text{ m}$	$1.626 \times 10^{-2} \text{ m}$
W_w	$2.5 \times 10^{-2} \text{ m}$	$2.28 \times 10^{-2} \text{ m}$
l_g	$3.9 \times 10^{-3} \text{ m}$	$3.66 \times 10^{-3} \text{ m}$

The nominal and optimal designs of the buck converter along with the corresponding objective functions are presented in Table 3.9. Response variables of interest for the optimized buck converter are given in Table 3.10. Response variables at their upper or lower bounds are listed in bold face type. The active constraints for the optimized converter design were the physical constraints on the design of the inductor and the constraint on the input voltage variation to the transient load disturbance. Note that the nominal design violates the constraint on the inductor current ripple. The optimized converter design is not significantly lighter than the nominal design, but it was obtained in a shorter period of time and with a minimal amount of effort compared to the standard manual design procedures.

Table 3.9. Component values and objective function for the buck converter

Variable	Nominal value	Optimal value
L	400 μH	419.75 μH
C	82 μH	46.88 μF
h_o	1	0.881
ω_z	100 rad/sec	420.14 rad/sec
ω_p	40000 rad/sec	54983 rad/sec
h_{ip}	1	0.998
h_{ii}	100	100
f_s	100kHz	100 kHz
<i>Weight</i>	1.5637 kg	1.5072 kg

Table 3.10. Response quantities for nominal and optimal designs

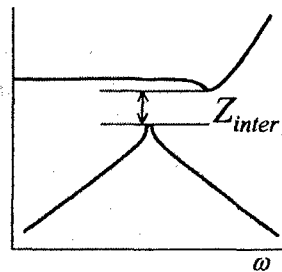
Response variable	Nominal	Optimal
Inductor current ripple	1.574 A*	1.5A
Capacitor voltage ripple	0.6V	1V
Phase margin	72.5°	69.54°
Gain margin	58.67 dB	37.13 dB
Minimum input impedance	33.72 dB	33.69 dB
Maximum output impedance	0.02 dB	1.25 dB
Audiosusceptibility	-57.24 dB	-55.99 dB
Peak output voltage	19.85 V	22.61 V
Peak input voltage	37.38 V	38.85 V

* violated constraint

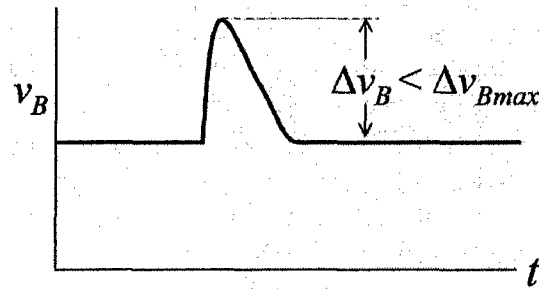
3.5 Optimization of sample system

The optimization procedure for the design of the sample system (combined filter/converter) is presented in this section. The individual optimization formulations of the input filter and the converter are combined with a few modifications in the definition of the constraints. The design variables are those of the input filter and the converter as shown in Tables 3.3 and 3.7. The constraints on the optimization of the interconnected system are obtained from those of the designs of each of the individual systems with some modifications to account for interactions between the input filter and the converter. The constraints that need to be modified are those that are defined at the interface between the input filter and the converter.

1. Due to the interconnection of the filter and the converter, it may not be appropriate to impose fixed limits on the output impedance of the filter and the input impedance of the converter, as was the case when they were designed independently. Since a sufficient condition for stability is to ensure a minimum separation between the two impedances, the constraints on the minimum input impedance of the converter, Z_{iB} , and the maximum output impedance of the filter, Z_{oF} , are replaced by a single constraint that imposes a lower bound on the difference between the two as shown in Figure 3.15a.



(a) Impedance Separation



(b) Interface voltage variation

Figure 3.15. Interaction constraints on the sample system design

The interaction constraints used for the current example are:

$$\min_{\omega} (|Z_{iB}(j\omega)|) - \max_{\omega} (|Z_{oF}(j\omega)|) > 15 \text{ dB.} \quad (3.33)$$

The 15-dB separation used in the first constraint is consistent with the constraints used for the individually optimized designs (Equations (3.9) and (3.27)) presented earlier. All other constraints are directly carried over from the optimization formulations of the input filter and the buck converter.

2. The constraint on the transient excursions on the output voltage of the input filter and the input voltage of the converter are replaced by a single constraint on the maximum excursion of the interface voltage v_B , as shown in Figure 3.15b.

$$v_B < 20V. \quad (3.34)$$

3. The objective function is the total weight of the input filter and converter.

3.5.1. Optimization Results

Converged optimal designs were obtained in approximately 1400 function evaluations, where a single function evaluation again includes both a time domain simulation and frequency domain computations. The optimizations were achieved in approximately 90 minutes on a 500 MHz Pentium III PC. The physical variables associated with the inductors in the sample system are given in Table 3.11. The component values and objective functions are given in Table 3.12. The important responses are listed in Table 3.13.

The active constraints for the filter in this optimization run were all the physical constraints on the design of the inductors, the lower bound constraint on the input impedance, the upper bound stopband constraint, and the upper bound constraint on the passband. The active constraints on the converter were the physical constraints on the inductor design and the upper bound on the voltage variation at the output due to a load disturbance. The filter design obtained from the combined problem is 5% lighter than that obtained from the individual optimization, while the converter design obtained for the combined optimization problem is almost identical to that obtained independently. Differences in the combined designs and the independently obtained designs arise because the interconnection of two subsystems creates a feedback loop where a change in the source subsystem causes a change in the load subsystem and vice versa. When the optimization was performed on the integrated sample system as a whole, the optimizer was able to take advantage of the interaction between the filter and converter and reduce the overall system weight. The nature of the interaction between the filter and the converter are explained in the following.

Table 3.11. Physical variables of inductors in sample system

Variables		Nominal	Individual Optimization	Integrated Optimization
FILTE	n_1	29.53	19.94	20.01
	A_{cp1}	0.630×10^{-5}	$0.530 \times 10^{-5} \text{ m}^2$	$0.521 \times 10^{-5} \text{ m}^2$
	C_{w1}	$0.751 \times 10^{-2} \text{ m}$	$0.484 \times 10^{-2} \text{ m}$	$0.480 \times 10^{-2} \text{ m}$
	W_{w1}	$0.682 \times 10^{-2} \text{ m}$	$1.017 \times 10^{-2} \text{ m}$	$1.014 \times 10^{-2} \text{ m}$
	l_{g1}	$1.16 \times 10^{-3} \text{ m}$	$0.664 \times 10^{-3} \text{ m}$	$0.657 \times 10^{-3} \text{ m}$
	n_2	45.98	42.77	42.81
	A_{cp2}	0.448×10^{-5}	$0.382 \times 10^{-5} \text{ m}^2$	$0.370 \times 10^{-5} \text{ m}^2$
	C_{w2}	$0.985 \times 10^{-2} \text{ m}$	$0.939 \times 10^{-2} \text{ m}$	$0.914 \times 10^{-2} \text{ m}$
	W_{w2}	$1.33 \times 10^{-2} \text{ m}$	$1.244 \times 10^{-2} \text{ m}$	$1.230 \times 10^{-2} \text{ m}$
	l_{g2}	$1.29 \times 10^{-3} \text{ m}$	$1.03 \times 10^{-3} \text{ m}$	$1.017 \times 10^{-3} \text{ m}$
	n_d	16.06	7.79	7.78
	A_{cpd}	0.349×10^{-5}	$0.359 \times 10^{-5} \text{ m}^2$	$0.356 \times 10^{-5} \text{ m}^2$
	C_{wd}	$0.396 \times 10^{-2} \text{ m}$	$0.585 \times 10^{-2} \text{ m}$	$0.576 \times 10^{-2} \text{ m}$
	W_{wd}	$0.978 \times 10^{-2} \text{ m}$	$0.564 \times 10^{-2} \text{ m}$	$0.561 \times 10^{-2} \text{ m}$
	l_{gd}	$0.355 \times 10^{-3} \text{ m}$	$0.176 \times 10^{-3} \text{ m}$	$0.172 \times 10^{-3} \text{ m}$
BUCK	n	55	55.55	55.55
	A_{cp}	$1.1 \times 10^{-5} \text{ m}^2$	$1.05 \times 10^{-5} \text{ m}^2$	$1.05 \times 10^{-5} \text{ m}^2$
	C_w	$1.65 \times 10^{-2} \text{ m}$	$1.626 \times 10^{-2} \text{ m}$	$1.63 \times 10^{-2} \text{ m}$
	W_w	$2.5 \times 10^{-2} \text{ m}$	$2.28 \times 10^{-2} \text{ m}$	$2.28 \times 10^{-2} \text{ m}$
	l_g	$3.9 \times 10^{-3} \text{ m}$	$3.66 \times 10^{-3} \text{ m}$	$3.67 \times 10^{-3} \text{ m}$

When the input filter is optimized individually, the load disturbance was represented by a pulse current load similar to that at the output of the converter except that it was scaled by its duty cycle. When the converter and the filter are optimized together, the load disturbance at the output of the filter (and hence, at the input of the converter) is filtered by the presence of the converter. Hence, the transient peak currents flowing into the inductors of the filter are less than those that were present when the filter was optimized individually.

This is illustrated in Figure 3.16 and where the transient responses of the filter inductor current i_{L1} , with and without the buck converter are shown. Since the peak currents flowing into the filter inductors are lower when the converter is taken into account, smaller inductors can be used. This results in a lower weight filter.

Table 3.12. Component values and Objective Function for the sample system

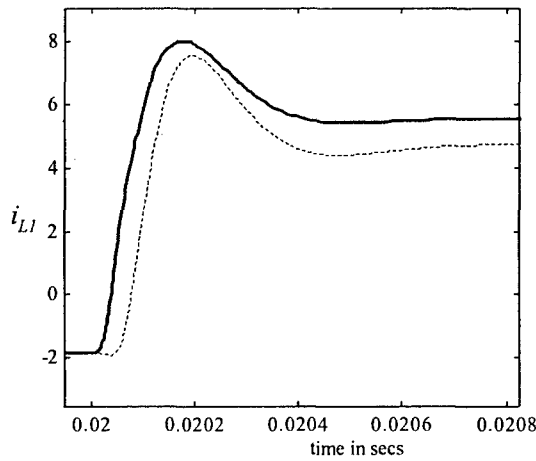
Variables		Nominal	Individual Optimization	Integrated Optimization
FILTE R	L_1	80 μ H	26.49 μ H	26.531 μ H
	L_2	300 μ H	296.77 μ H	283.84 μ H
	L_d	21.5 μ H	22.29 μ H	22.045 μ H
	C_1	5 μ F	7.19 μ F	7.21 μ F
	C_2	18.8 μ F	27.70 μ F	27.86 μ F
	R_d	3 Ω	2.23 Ω	2.27 Ω
WEIGHT		0.5279 kg	0.3692 kg	0.3495 kg
CON VERT ER	L	400 μ H	419.75 μ H	419.75 μ H
	C	82 μ F	46.88 μ F	46.904 μ F
	h_o	1	0.881	0.880
	ω_z	100 rad/sec	420.14 rad/sec	420.12 rad/sec
	ω_p	40000	54983 rad/sec	54998.2 rad/sec
	h_{ip}	1	0.998	0.998
	h_{ii}	100	100	100
	f_s	100 kHz	100 kHz	100 kHz
WEIGHT		1.5637 kg	1.5072 kg	1.5072 kg

Table 3.13. Response quantities of Integrated Optimization

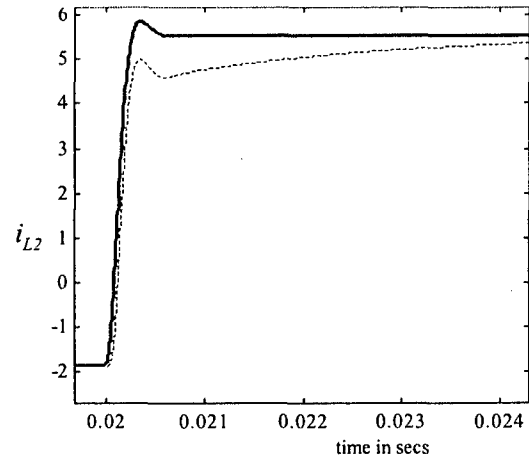
Response Quantity		Value
INPUT FILTER	Minimum input impedance	3.00 dB
	Maximum output	9.3382 dB*
	Passband maximum	3.36 dB
	Passband minimum	4.87×10^{-6} dB
	Stopband maximum	-60 dB
BUCK CONVERTER	Phase margin	69.57°
	Gain Margin	37.18 dB
	Minimum input impedance	33.72 dB*
	Maximum output	1.25 dB
	Audiosusceptibility	-55.98 dB
	Peak output voltage	22.59 V
INTERFACE QUANTITIES	Impedance Difference	24.378 dB
	Peak interface voltage	11.81 V

* These responses were not constrained while performing the integrated optimization. They are shown here for the sake of completeness.

It can be seen from Figure 3.17 that the output voltage variation of the buck converter in the optimized sample system is higher than that of the individually optimized converter.



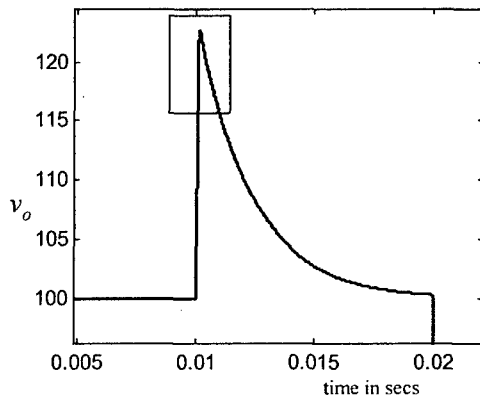
(a) Filter Inductor current i_{L1}



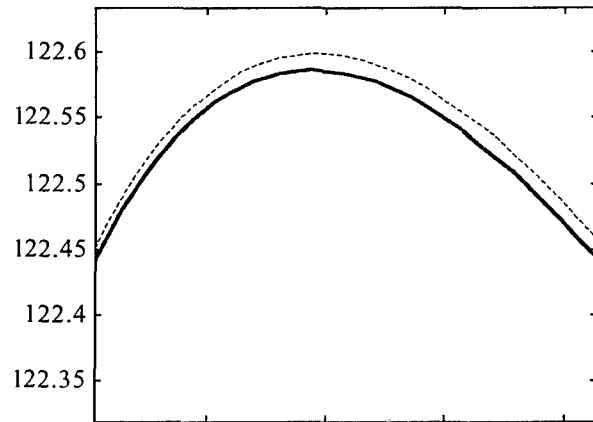
(b) Filter Inductor Current i_{L2}

Figure 3.16. Filter inductor currents with (--) and without (-) buck converter

Simulation results of the sample system with the converter design obtained from the individual and integrated optimizations are shown in Figure 3.17.



(a) Converter output voltage in sample system



(b) Expanded view of boxed area in (a)

Figure 3.17. Converter output voltage in sample system with individually optimized converter design (-) and converter design obtained from optimized sample system (--)

A similar observation can be made from Figures 3.16a and 3.16b, where the filter inductor currents are shown. The optimizer increases the capacitance slightly (Table 3.12) at the output of the buck converter to allow a larger voltage variation. This results in a larger portion of the transient current to flow into the output capacitance of the buck converter than propagate to the filter. This enables the filter weight to be significantly decreased. The optimizer was, therefore, able to take advantage of the system interactions and the more accurate representations of the load disturbances and voltage variations to arrive at an improved (lower weight) design for the combined filter/converter sample system.

3.6 Bi-level Optimization of the Input Filter

The simulation of a large power distribution system such as that depicted in Figure 2.1 involves complicated interactions between the various subsystems that must be taken into account in the design process. The work presented in Section 3.5 has demonstrated that, even for a very simple two-component circuit design, it is advantageous to optimize the system as a whole rather than optimizing each of the individual components independently.

Unfortunately, as additional components are added to the optimization problem, the optimization task becomes more difficult. The optimization algorithm becomes less efficient as the number of design variables and constraints increase, and the computational expense of simulating the response of the overall power system rapidly grows very large (especially when the simulations need to be repeated numerous times).

In order to surmount these difficulties, a bi-level design methodology was formulated for the power system design. In the bi-level design methodology, the design problem is decomposed into two design levels: an *upper* design level and a *lower* design level. At the upper level, the power system as a whole is evaluated and designed using as few design variables as possible. The design variables describing each component in the system are sufficient to specify its overall behavior and its interaction with the other components in the system, but design variables describing local details are omitted. At the lower level, detailed models of the individual components are used to compute more complex behavior and to design the details that were not included in the upper level model. The upper and lower level design problems cannot be solved independently from one another, and must be properly coordinated. In the present work, the upper and lower design levels are coordinated with one another using a *design database*.

This proposed methodology allows the complexity of the system level design problem to be reduced while simultaneously accounting for potentially important local details. A description of the bi-level optimization methodology as applied to the system-level input filter design problem is presented in the following section. In section 3.6.2, the methodology is extended to the design of the inductors in the input filter.

3.6.1. Bi-Level Formulation for System Design

The formulation for the bi-level system design problem will be presented in this section. At the upper level, the filter will be evaluated and designed using a simple model suitable for inclusion in a large power system design problem. At the lower level, the filter details will be designed using a more accurate model.

In section 3.3, it was necessary to specify values for 18 design variables to design the input filter. If one only wishes to determine the low-frequency behavior of the filter, however, it is not necessary to know all of the details of the filter design: it is only necessary to know the effective inductance, L , resistance, R , and capacitance, C , of the filter. This means that it may be possible to remove the 18 design variables describing the

filter from the system-level design problem and replace them with the three variables L , R , and C . To compute the total weight of the filter, however, it is necessary to know the weight of the filter as a function of the variables L , R and C . As it turns out, it is possible in this case to formulate a separate design problem that will allow the minimum filter weight to be computed as a function of L , R and C . This second optimal design problem will constitute the lower-level design level for the input filter design problem. The formulations for the upper and lower level design problems will be described in the following two sections.

Upper-Level: System Design Problem

The system-level filter design problem utilizes the model illustrated in Figure 3.19. In this model, the filter is characterized by three design variables: inductance L , capacitance C , and resistance, R . This simplified model is capable of accurately predicting the low frequency behavior of the filter, including the interface voltages v_B and v_o .

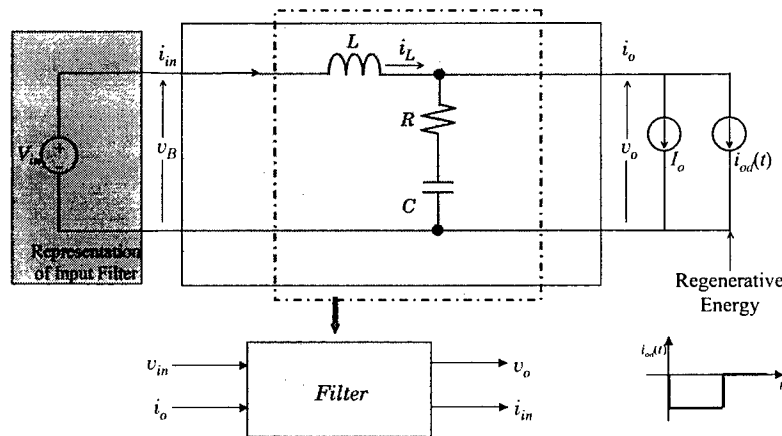


Figure 3.19. Upper-level filter model

The upper-level optimization problem can be stated as follows:

Given: operating conditions (Table 3.1)

Minimize: total filter weight

By varying: L , R , C

Such that:

- The output impedance of the filter, Z_{of} , must be less than the input impedance of the converter, Z_{il} , in order to ensure stability of the interconnected system. Since Z_{il} is

given, sufficient separation between these two impedances can be enforced by requiring that the maximum output impedance of the filter satisfy:

$$Z_{o_max} = \max_{\omega} (|Z_{of}^U(j\omega)|) < 15 \text{ dB}\Omega < Z_{iL}. \quad (3.35)$$

- To assure that the interaction between the filter and the power bus is stable, the minimum input impedance of the filter must exceed the maximum output impedance of the power bus, Z_{oC} . Since Z_{oC} is given, sufficient separation between these two impedances can be enforced by requiring that the minimum input impedance of the filter satisfy:

$$Z_{i_min} = \min_{\omega} (|Z_{if}^U(j\omega)|) > 3 \text{ dB}\Omega > Z_{oC}. \quad (3.36)$$

- The magnitude of the input-output transfer function of the filter, $A_v(j\omega)$, must remain between an upper bound, 6dB , and a lower bound, -1dB , up to a passband edge frequency, ω_p (see Figure 3.20):

$$-1\text{dB} \leq |A_v(j\omega)| \leq 6\text{dB} \quad \text{for } 0 \leq \omega \leq \omega_p = 2\pi 5 \times 10^3 \text{ rad/sec}. \quad (3.37)$$

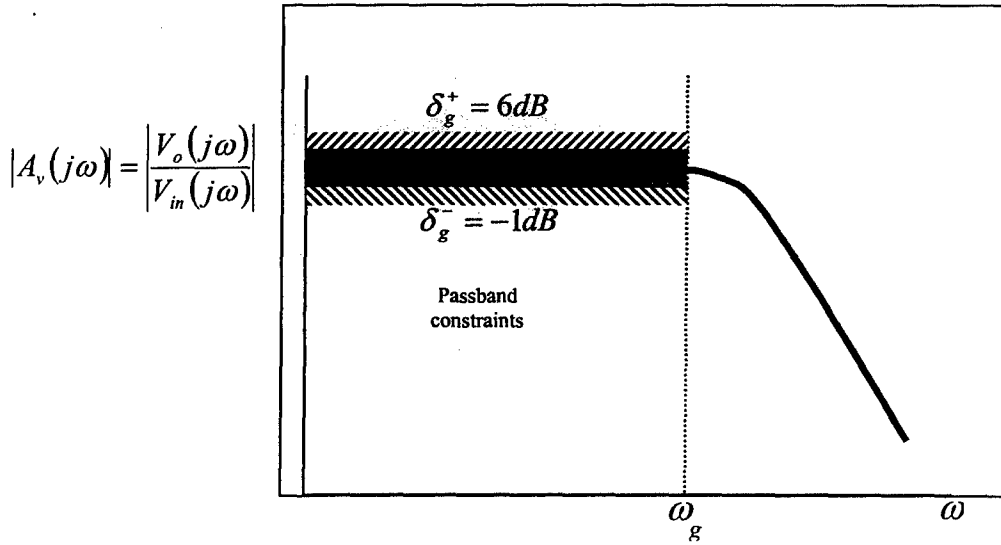


Figure 3.20. Passband constraints for system-level filter

- The maximum transient excursion of the output voltage of the filter is to 20dB (see Figure 3.22):

$$\Delta v_B < 20 \text{ V}. \quad (3.38)$$

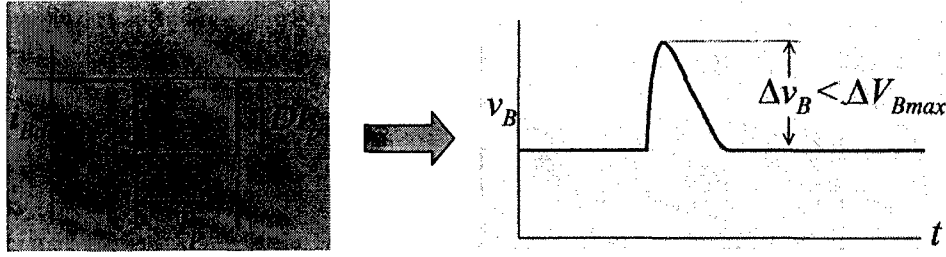


Figure 3.22. Time domain constraint

Note that the system-level design problem cannot be solved independently from the lower-level design problem – information from the detailed filter design problem is required to accurately compute the filter weight as a function of L , R , and C . The lower-level design problem can be stated as follows:

Lower-Level: Detailed Filter Design Problem

The lower level input filter model (Figure 3.3) is the same as that used in section 3.3. Given an upper level design (L , R , C), the objective of the lower level design problem is to minimize the filter weight by varying the values of the variables listed in Table 3.14 while matching the behavior of the upper level design up to a specified frequency. The matching is accomplished by requiring that the higher order input-output transfer function for the detailed lower level design matches the lower order transfer function for the upper level design up to the specified frequency. Operating conditions for the filter are given in Table 3.1.

Given: Upper level filter design (L , R , C) and operating conditions

Minimize: total filter weight

By varying: $n_1, A_{cp1}, C_{w1}, W_{w1}, I_{g1}, n_2, A_{cp2}, C_{w2}, W_{w2}, I_{g2}, n_d, A_{cpd}, C_{wd}, W_{wd}, I_{gd}, C_l, C_2, R_d$

Such that:

- The magnitude of the input-output transfer function of the filter, $A_v(j\omega)$, remains between an upper bound, δ_g^+ , and a lower bound, δ_g^- , up to a passband edge frequency, ω_p (see Figure 3.23). The bounds are chosen so that the upper level and lower level transfer functions match in the passband. These upper and lower bounds are computed using the specified L , R , and C values.

$$\delta_g^- \text{ dB} \leq |A_v(j\omega)| \leq \delta_g^+ \text{ dB} \quad \text{for } 0 \leq \omega \leq \omega_p = 2\pi 5 \times 10^3 \text{ rad/sec.} \quad (3.39)$$

- The magnitude of the input-output transfer function, $A_v(j\omega)$, remains below an upper bound above a certain frequency, ω_{s1} (see Figure 3.23):

$$|A_v(j\omega)| < -60 \text{ dB} \quad \text{for } \omega > \omega_{s1} = 2\pi \cdot 50 \times 10^3 \text{ rad/sec} \quad (3.40)$$

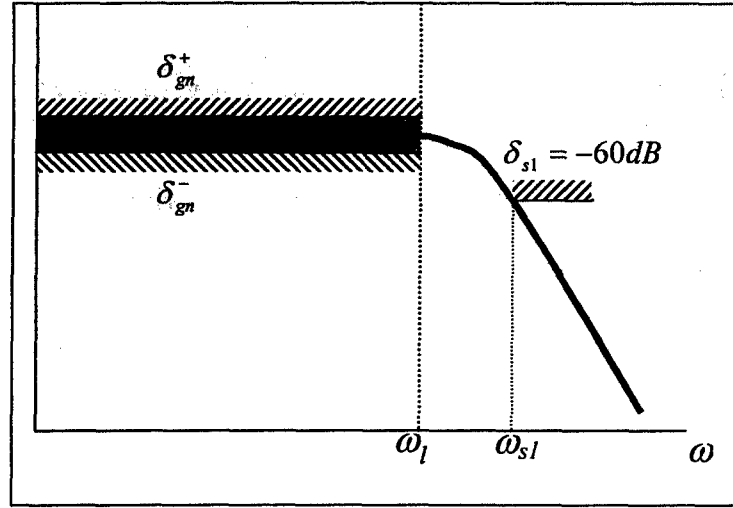


Figure 3.23. Required frequency response of lower-level filter design

- The maximum output impedance of the lower level filter, Z_{oF}^L , must be less than or equal to the maximum output impedance of the upper level filter, Z_{oF} . Because Z_{oF} is required (Equation 3.35) to be less than the input impedance of the converter, Z_{iL} , (to ensure stability of the interconnected system) this constraint assures that that Z_{oF}^L will also be less than to the input impedance of the converter.

$$Z_{o_max} = \max_{\omega} (|Z_{oF}^L(j\omega)|) \leq \max_{\omega} (|Z_{oF}^U(j\omega)|) \quad (3.41)$$

- To assure that the interaction between the filter and the power bus is stable, the minimum input impedance of the lower level filter, Z_{iF}^L , must be greater than or equal to the minimum input impedance of the upper level filter, Z_{iF} . Because Z_{iF} is required (Equation 3.36) to exceed the maximum output impedance of the power bus, Z_{oC} , (to ensure stability of the interconnected system) this constraint assures that Z_{iF}^L will also exceed Z_{oC} .

$$Z_{i_min} = \min_{\omega} (|Z_{iF}^L(j\omega)|) \geq \min_{\omega} (|Z_{iF}^U(j\omega)|) \quad (3.42)$$

For each of the inductors (L_1 , L_2 , and L_d):

- The computed inductance:

$$L^* = \frac{\mu_o K_1 C_w^2 n^2}{l_g + Z_p / \mu_r}, \quad (3.43)$$

is equal to the given inductance, L . Here, μ_o is the permeability of free space, μ_r is the permeability of ferrite, K_l is the aspect ratio of the core leg, and Z_p is the mean magnetic path length.

- The widths of the center leg, C_w , and of the window, W_w , are greater than 1 mm.
- The copper wire cannot have a cross-sectional area less than $7.29 \times 10^{-8} \text{ m}^2$.
- The current density in the windings of the inductor cannot be greater than maximum allowable current density for copper which was considered to be $5.5 \times 10^6 \text{ A/m}^2$.
- The window of the EE-core houses the windings and the bobbin. The area occupied by the windings is given by:

$$W_a = \frac{nA_{cp}}{F_w}, \quad (3.44)$$

where $F_w=0.4$ is the window fill factor. The window fill factor is included to account for imperfections in the windings on the bobbin. The area occupied by the bobbin in the window, using simple geometry, can be determined as:

$$W_b = W_{bob} K_2 W_w, \quad (3.45)$$

where W_{bob} is the thickness of the bobbin wall. Hence, the window is required to be large enough to accommodate the windings and the bobbin. This requirement is formulated as a constraint given by:

$$K_2 W_w^2 > W_a + W_b. \quad (3.46)$$

- In order to prevent the inductor core from running into saturation, the dimensions of the inductor should be such that the maximum allowable saturation flux density for a ferrite core material, $B_{sp} = 0.3 \text{ T}$, is not exceeded. The maximum flux density is determined as the ratio of the maximum flux to the area of cross section of the center leg. Hence, this constraint is given by:

$$B_{sp} > \frac{\Phi_{pk}}{A_{Cw}} = \frac{(\psi_{pk}/n)}{K_1 C_w^2} = \frac{(LI_{L(pk)}/n)}{K_1 C_w^2}. \quad (3.47)$$

Combined Upper and Lower Level Design Problems

By solving the lower level filter design problem, the minimum filter weight can be computed as a function of the upper level parameters L , R , and C . Thus, for every

different design that the upper level optimization code generates during the design iterations, the lower level optimization problem can be solved to find the associated weight.

In practice, it is often difficult or time consuming to directly connect the lower level optimizer to the upper level optimizer and to properly coordinate the flow of information between them. An alternative is to approximate the output of the lower level optimizers using relatively simple functions (response surface approximations) before the upper level iterations begin. Once the response surface(s) are constructed, they can be used as surrogates for the lower level optimizer. Instead of calling the local optimizer at each iteration, the upper level optimizer may evaluate the response surface function to obtain an estimate of the filter weight. The approach was used in the present work.

Before trying to solve the system-level design problem, the lower-level optimization problem is solved for a range of different L , R , and C values and the results stored in a "design database". Using the data stored in the database, a simple function (a polynomial least-squares fit) is constructed that approximates the filter weight as a function of L , R , and C . Once the function is obtained, the upper-level optimization problem can be run and the system can be designed. In the present example, the system level consists only of a simplified filter model, but in practice it can consist of any number of connected components. Whenever the weight of the filter is required, L , R , and C are inserted into the response surface function and the required weight is efficiently computed.

Given the existence of the response surface function, the number of design variables required to design the filter at the system level is reduced from eighteen to three. This means that the system level design problem can now be solved more efficiently and reliably. This may be especially important if the system level design problem consists of large numbers of interconnected components. Although it was not investigated here, it is possible that a similar methodology could be used to decompose the design problem for other components in the power system, further increasing the efficiency of the system level design.

Examples

The first step in the bi-level design process is to solve the lower level design problem for different values of L , R , and C and to store the results in a database. Given sufficient data, this database will be used to approximate the results (optimal weight) of the lower level optimizer. Before the database can be constructed, it is necessary to decide what ranges of the variables L , R , and C the database should be valid for. A database valid for large variable ranges will be more versatile, but will be more time consuming to construct. On the other hand, if the variable ranges are too small, the resulting database will not be very useful. In the present work, physical principals were used to derive a set of variable ranges for the input filter. The derivation is given in the following section.

Derivation of the ranges for L, R, C

To design the filter, some general criteria must first be specified:

$$\begin{aligned} f_s &\in [f_{s_min}, f_{s_max}], \\ Q &\in [Q_{min}, Q_{max}], \\ P_{loss} &\in [P_{loss_min}, P_{loss_max}]. \end{aligned} \quad (3.48)$$

If the corner frequency is set as:

$$\omega_0 = 1/10 \cdot 2\pi f_s$$

then:

$$\omega_0 = \frac{1}{\sqrt{LC}} = 1/10 \cdot 2\pi f_s, \quad (3.49)$$

$$Q = \delta^+ - \delta^- = \frac{\sqrt{L/C}}{R}, \quad (3.49)$$

$$i_{AC}^2 R = P_{loss}, \quad (3.50)$$

where i_{AC} is the current through the resistor R. Depending on the ranges of f_s, Q, P_{loss} in Equation 3.48 and on Equations 3.49 through 3.50, meaningful values for L, R, and C can be computed.

First, derive i_{AC} . Assuming the output current of the buck converter is I_o , we can get the waveform of output current of the filter shown in Figure 3.24.

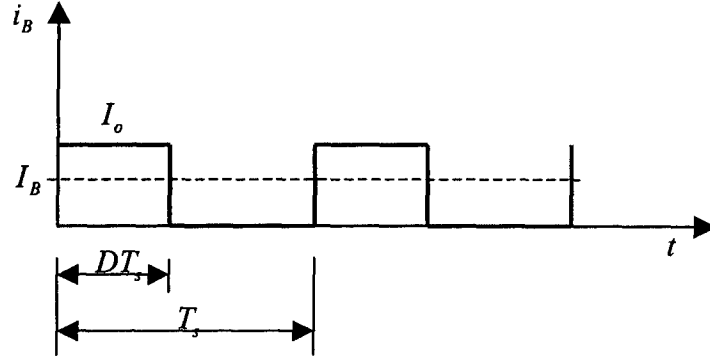


Figure 3.24. Waveform of the output current of the filter

From the circuit, we know:

$$i_{AC}^2 R = P_{loss}, \quad (3.51)$$

$$i_{B_PK} = I_o, \quad (3.52)$$

$$I_B = DI_o. \quad (3.53)$$

The current through the resistor is:

$$i_{AC} = i_{AC}^+ = i_{B_pk} - I_B, \quad (3.54)$$

during ON time, and:

$$i_{AC} = i_{AC}^- = 0 - I_B, \quad (3.55)$$

during OFF time. Then get:

$$P_{loss} = i_{AC}^{+2} RD + i_{AC}^{-2} RD'. \quad (3.56)$$

From equations (3.54), (3.55) and (3.56), we have:

$$P_{loss} = DD' I_o^2 R, \quad (3.57)$$

$$\Rightarrow R = \frac{P_{loss}}{DD' I_o^2}. \quad (3.58)$$

According to equations (3.49),

$$\sqrt{\frac{L}{C}} = RQ. \quad (3.59)$$

From equations (3.48), (3.58) and (3.59), we can derive:

$$C = \frac{DD'I_o^2}{P_{loss} \cdot 0.1 \cdot 2\pi f_s}. \quad (3.60)$$

From equations (3.59) and (3.60), we have:

$$L = \frac{P_{loss} Q}{DD'I_o^2 \cdot 0.1 \cdot 2\pi f_s}. \quad (3.61)$$

Summarizing equations (3.58), (3.60) and (3.61) we have:

$$R = \frac{P_{loss}}{DD'I_o^2}, \quad (3.62)$$

$$C = \frac{DD'I_o^2}{P_{loss} \cdot 0.1 \cdot 2\pi f_s}, \quad (3.63)$$

$$L = \frac{P_{loss} Q}{DD'I_o^2 \cdot 0.1 \cdot 2\pi f_s}. \quad (3.63)$$

So for any given value or range of f_s, Q, P_{loss} and converter specifications, we can obtain the value or the range of L, R, C .

Consider the parameters of the sample system given in Table 3.1:

$$I_o = 15A, \quad (3.64)$$

$$V_o = 100V,$$

$$V_B = 270V,$$

the duty cycle is:

$$D = 100 / 270 = 0.37. \quad (3.65)$$

Given:

$$f_s \in [50k, 250k], \quad (3.66)$$

$$Q \in [0.1, 5], \quad (3.67)$$

$$P_{loss} \in [2\%P_o, 20\%P_o], \quad (3.68)$$

Then from equations (3.58), (3.60) and (3.61), we can get the ranges for L , R , C :

$$R \in [0.572, 5.72]\Omega, \quad (3.69)$$

$$C \in [1.113, 55.65]\mu F, \quad (3.70)$$

$$L \in [0.364, 910.4]\mu H. \quad (3.71)$$

Comparison of Lower-Level and Upper Level Responses

Given an upper-level filter design (specified values for L , R , and C), the lower level optimization problem can be solved. The objective of the lower level optimization problem is to find the lowest weight filter design that matches the low-frequency behavior of the upper level design. To demonstrate this process, an arbitrary combination of L , R , and C were chosen ($100 \mu H$, 1.0Ω , $100 \mu F$), the lower level optimization problem was solved, and the upper and lower level responses were compared.

The upper level simulation was run, and the following characteristic parameters were obtained:

$$\max |Z_{out}^{global}| = 1\Omega = 0dB, \quad (3.72)$$

$$\min |Z_{in}^{global}| = 1.414\Omega = 3dB, \quad (3.73)$$

$$\delta_g^+ = 3.33dB, \quad (3.74)$$

$$\delta_g^- = 0dB. \quad (3.75)$$

Using equations 3.72 through 3.75, the constraints for the lower-level design problem can be formulated (Equations 3.39 through 3.42). The results of running the lower level optimization problem with these constraints are presented in Table 3.14.

The corresponding frequency and time response are shown in Figures 3.25 and 3.26.

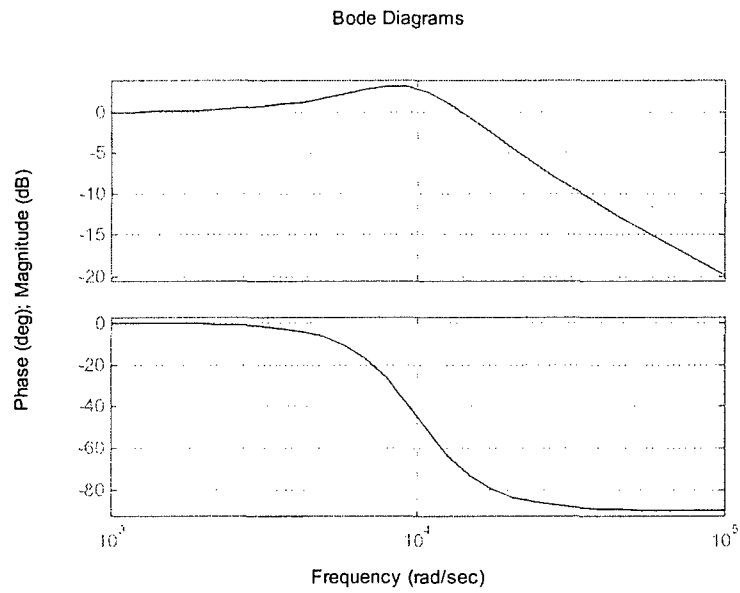


Figure 3.25. Frequency domain response of the upper-level filter

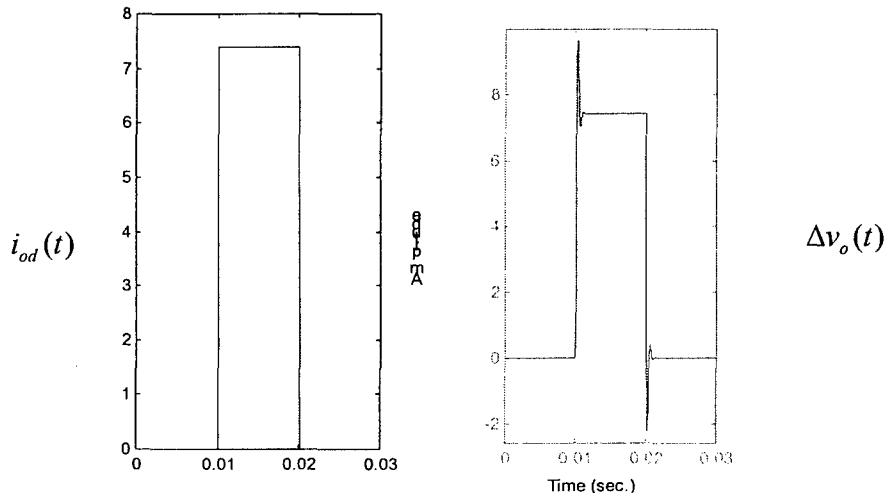


Figure 3.26. Time domain response of the upper-level filter

Table 3.14. Corresponding lower-level design

Design Variable	Optimized Value
C_1	11.913e-5F
C_2	6.7955e-5F
R_d	0.97387
L_d	1.4909e-5H
L_1	1.6058e-5H
L_2	1.3e-3H
Weight	0.45891

The frequency and time domain responses of the upper and lower level filter models are compared in Figures 3.27 and 3.28. From this comparison it is concluded that the optimized local level model adequately matches the global level model. Note that although no constraints were explicitly placed on the lower level design in the time domain, the time domain comparisons are nevertheless quite good.

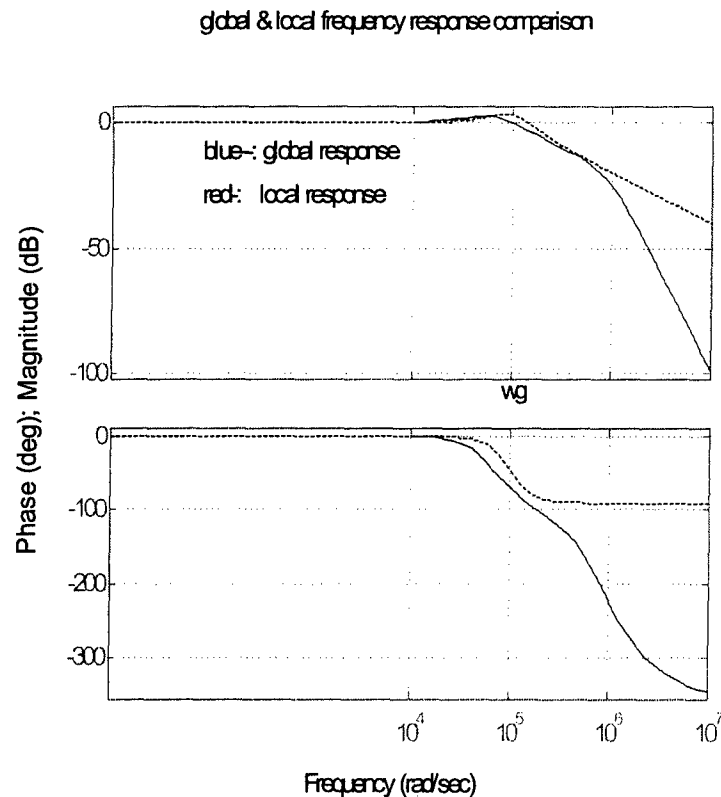


Figure 3.27. Comparison of upper and lower level frequency response

The optimized weight from local level optimization can be equated to the optimized weight of this upper level filter design. Namely:

$$\text{Weight}(L = 100\mu H, R = 1\Omega, C = 100\mu F) = \text{Optimized_local_level_weight} = 0.45891. \quad (3.76)$$

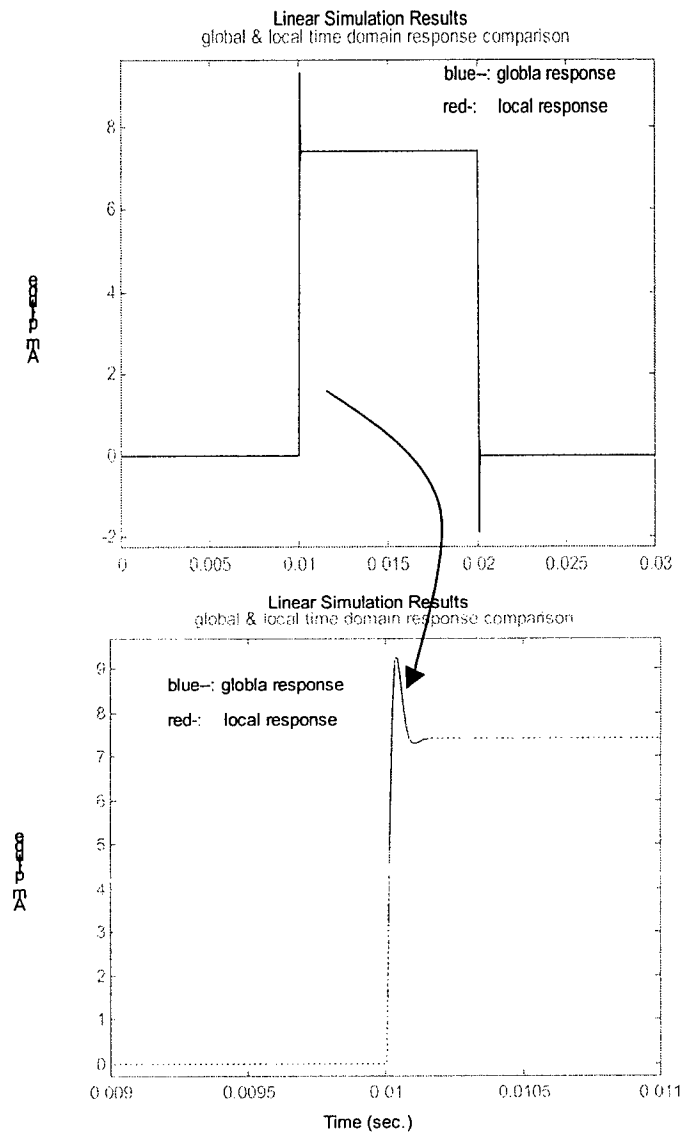


Figure 3.28. Comparison of upper and lower level time domain response

Construct filter design database

To populate the filter design database, the lower level optimization problem must be run for a number of different combinations of L , R , and C (design points) chosen from within the ranges given in Equations 3.69, through 3.71.

Step 1: Choose design points

The 10 combinations of L , R , and C that were chosen for the present work are given in Table 3.15.

Table 3.15. Chosen combinations of the global design variables

$L(\mu H)$	R	$C(\mu F)$
455.382	5.72	28.3815
455.382	3.146	1.113
455.382	3.146	28.3815
455.382	3.146	55.65
455.382	0.572	28.3815
910.4	5.72	1.113
910.4	5.72	55.65
910.4	3.146	28.3815
910.4	0.572	1.113
910.4	0.572	55.65

For each combination of the upper level design variables shown in table 3.15, the upper level simulation is run and the characteristic parameters that determine the lower level constraints (Equations 3.39 through 3.42) are determined (Table 3.16).

Table 3.16. Characteristic parameters corresponding to Table 3.15

Z_{IF}	Z_{OF}	δ_+	δ_-	ω_g
15.1479	15.3522	2.0613	1.12E-05	8.80E+03
9.9552	42.3863	16.2926	4.40E-07	4.44E+04
9.9552	16.3449	4.4709	1.12E-05	8.80E+03
9.9552	12.2395	2.9481	2.20E-05	6.28E+03
-4.8521	29.0466	17.0145	1.12E-05	8.80E+03
15.1479	43.2772	14.1902	8.80E-07	3.14E+04
15.1479	15.397	2.0899	4.40E-05	4.44E+03
9.9552	21.3559	6.4808	2.24E-05	6.22E+03
-4.8521	63.1086	33.9816	8.80E-07	3.14E+04
-4.8521	29.2134	17.0967	4.40E-05	4.44E+03

Step 2: Run lower level optimization

For each combination of L , R , and C , the local level optimization problem was solved and the corresponding optimized weight was obtained (Table 3.17).

Step3: Construct approximating function

Using the results of the lower level optimization (Table 3.17), an equation can be constructed that approximates the optimized filter weight as a function of L , R , and C . The equation in this case was generated using a stepwise regression procedure that chose a subset of regressors from a cubic polynomial. The resulting response surface equation was as follows:

$$\text{Weight} = (0.1032 + 0.08438*R + 0.002399*C + 0.001724*R*C - 0.5498e-6*C^3 - 0.1074e4*L*R^2 - 0.2205e-3*R^2*C - 0.1667e-4*R*C^2)^2. \quad (3.76)$$

Table 3.17a. Results of Lower Level Optimization Runs

<i>Variable</i>	$L=455.382$ $R=3.146$ $C=28.3815$	$L=455.382$ $R=3.146$ $C=55.65$	$L=455.382$ $R=3.146$ $C=1.113$	$L=455.382$ $R=0.572$ $C=28.3815$	$L=455.382$ $R=5.72$ $C=28.3815$
C_1	0.72889	0.66205	0.69709	0.82482	0.71615
C_2	2.4154	2.5913	2.1564	2.5166	1.5057
R_d	0.1315	0.1166	0.13712	0.1468	0.11549
n_d	0.33776	0.28239	0.30965	0.33825	0.35949
A_{cpd}	0.59496	0.58239	0.69519	0.63494	0.51914
C_{wd}	2	2	1.53	1.5678	1.6143
W_{wd}	8.2884	11.343	5.8369	6.946	9.5468
l_{gd}	0.10793	7.87E-02	0.11134	0.10101	7.60E-02
n_l	0.99732	0.77332	0.61736	0.38606	1.1496
A_{cpl}	0.94165	0.94097	1.0856	0.8434	0.8572
C_{wl}	0.41989	0.42592	0.44268	0.51468	0.25262
W_{wl}	0.57248	0.56912	0.5246	0.33788	0.41037
l_{gl}	8.81E-02	7.53E-02	8.92E-02	0.11639	7.73E-02
n_2	0.1	0.1	0.10001	0.1	0.1256
A_{cp2}	0.40208	0.36649	0.33543	0.28919	0.25443
C_{w2}	0.64137	0.67337	0.23257	2.2503	0.1
W_{w2}	2.8049	3.1195	0.62825	2.7674	1.6932
l_{g2}	3.3834	3.3305	3.7079	0.94563	5.788
<i>Weight</i>	0.23372	0.13249	0.10133	0.044439	0.21781

Table 3.17b. Results of Lower Level Optimization Runs

<i>Variable</i>	<i>L=910.4</i> <i>R=3.146</i> <i>C=28.3815</i>	<i>L=910.4</i> <i>R=0.572</i> <i>C=1.113</i>	<i>L=910.4</i> <i>R=0.572</i> <i>C=55.65</i>	<i>L=910.4</i> <i>R=5.72</i> <i>C=1.113</i>	<i>L=910.4</i> <i>R=5.72</i> <i>C=55.65</i>
C_1	0.66218	0.19189	0.46059	0.5539	0.59623
C_2	2.6074	0.62948	1.5758	1.9406	1.784
R_d	0.11576	0.1248	0.13593	0.11257	0.11806
n_d	0.20738	0.31209	0.6999	0.1848	0.26943
A_{cpd}	0.58224	0.34434	0.5103	0.50825	0.58854
C_{wd}	1.8296	0.45542	1.2803	1.4273	1.4285
W_{wd}	10.409	2.8412	1.0287	8.3997	9.3336
l_{gd}	7.86E-02	7.41E-02	0.14207	0.076345	6.91E-02
n_1	0.76315	0.43236	0.1	0.61982	1.3431
A_{cpl}	0.90424	0.50014	0.75921	0.81	0.81229
C_{wl}	0.41788	0.47933	0.47929	0.21857	0.22987
W_{wl}	0.55847	0.10189	0.1	0.52079	0.42435
l_{gl}	7.46E-02	0.10289	1.83E-02	9.42E-02	8.96E-02
n_2	0.1	0.1	0.1	0.26566	0.18056
A_{cp2}	0.37873	0.19491	0.15958	0.31777	0.26992
C_{w2}	0.37869	1.14	1.1	0.1	0.1
W_{w2}	2.8983	4.7031	22.189	0.42879	1.2918
l_{g2}	3.2989	0.63463	1.6875	5.9976	5.8311
<i>Weight</i>	0.11901	0.024352	0.046178	0.075848	0.26573

Combined Upper/Lower Optimization

Once the approximating function is constructed, it is possible to solve the combined upper/lower level optimization problem in an efficient manner. The result of the converged optimization process will be a minimum weight system design that satisfies all global and local constraints. The results obtained in the present case are presented in the following paragraphs.

3.6.2. Bi-Level Inductor Design Problem

While the work described in Section 3.6.1 was being performed, it was realized that the lower level optimization problem described in that section could be further simplified by another application of the bi-level optimization methodology. The lower level

optimization problem in Section 3.6.1 contained 18 design variables (see Table 3.14). Many of these variables describe physical dimensions and characteristics of the three inductors L_1 , L_2 , and L_d . For example, the variables n_d , A_{cpd} , C_{wd} , W_{wd} , and l_{gd} all specify the detailed design of inductor L_d . If one wishes to determine the behavior of the filter as a whole, it is not necessary to know the details of each inductor design: only the inductance, L , of each inductor is needed. This indicates that the design variables describing the inductor details can be removed from the filter design problem. If one wishes to compute the total weight of the filter, however, the weight of each inductor as a function of L is required. As before, it is possible to formulate a lower level design problem that will allow the minimum inductor weight to be computed as a function of the inductance, L , and the peak inductor current, $I_{L(pk)}$. This second optimal design problem constitutes the lower-level design level for this section. The formulation for the upper and lower level design problems is described in the following sections.

Upper-Level: Filter Design Problem

Given: operating conditions (Table 3.1)

Minimize: total filter weight

By varying: L_1 , L_2 , L_d , C_1 , C_2 , R_d

Such that:

- The magnitude of the input-output transfer function of the filter, $A_v(j\omega)$, remains between specified upper and lower bounds up to a passband edge frequency, ω_p (see Figure 3.29):

$$-1 \text{ dB} \leq |A_v(j\omega)| \leq 6 \text{ dB} \quad \text{for } 0 \leq \omega \leq \omega_p = 2\pi \cdot 5 \times 10^3 \text{ rad/sec.} \quad (3.77)$$

- The magnitude of the input-output transfer function, $A_v(j\omega)$, remains below an upper bound above a certain frequency, ω_{s1} (see Figure 3.29):

$$|A_v(j\omega)| < -60 \text{ dB} \quad \text{for } \omega > \omega_{s1} = 2\pi \cdot 50 \times 10^3 \text{ rad/sec} \quad (3.78)$$

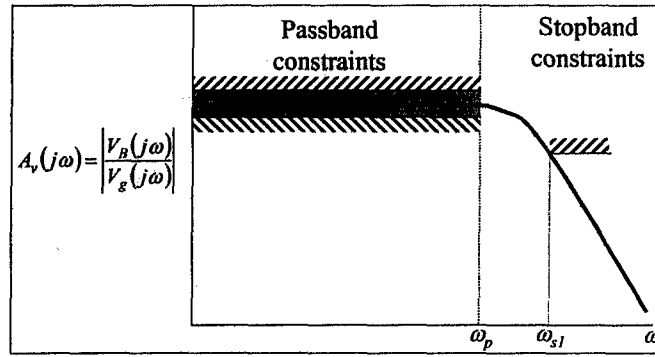


Figure 3.29. Definition of frequency domain constraints

- For a given load disturbance, the maximum transient excursion of the output voltage of the filter, Δv_B , is less than 20 V.

$$\Delta v_B < 20 \text{ V.} \quad (3.79)$$

- The output impedance of the filter, Z_{of} , must be less than the input impedance of the converter, Z_{iL} , in order to ensure stability of the interconnected system. Since Z_{iL} is given, sufficient separation between these two impedances can be enforced by requiring that the maximum output impedance of the filter satisfy:

$$Z_{o_max} = \max_{\omega} (|Z_{oF}(j\omega)|) < 15 \text{ dB}\Omega < Z_{iL}. \quad (3.80)$$

- To assure that the interaction between the filter and the power bus is stable, the minimum input impedance of the filter must exceed the maximum output impedance of the power bus, Z_{oC} . Since Z_{oC} is given, sufficient separation between these two impedances can be enforced by requiring that the minimum input impedance of the filter satisfy:

$$Z_{i_min} = \min_{\omega} (|Z_{iF}(j\omega)|) > 3 \text{ dB}\Omega > Z_{oC}. \quad (3.81)$$

Note that the upper-level design problem cannot be solved independently from the lower-level design problem – information from the local design problem is needed to compute the weight of each inductor in the filter. The lower-level design problem can be stated as follows:

Lower-Level: Inductor Design Problem

Given: $L, I_{L(pk)}$

Minimize: inductor weight

By varying: n, A_{cp}, C_w, W_w, l_g

Such that:

- The computed inductance:

$$L = \frac{\mu_o K_l C_w^2 n^2}{l_g + Z_p / \mu_r}, \quad (3.82)$$

is equal to the given inductance, L . Here, μ_o is the permeability of free space, μ_r is the permeability of ferrite, K_l is the aspect ratio of the core leg, and Z_p is the mean magnetic path length.

- The widths of the center leg, C_w , and of the window, W_w , are greater than 1 mm.
- The copper wire cannot have a cross-sectional area less than $7.29 \times 10^{-8} \text{ m}^2$.
- The current density in the windings of the inductor cannot be greater than maximum allowable current density for copper which was considered to be $5.5 \times 10^6 \text{ A/m}^2$.
- The window of the EE-core houses the windings and the bobbin. The area occupied by the windings is given by:

$$W_a = \frac{n A_{cp}}{F_w}, \quad (3.83)$$

where $F_w=0.4$ is the window fill factor. The window fill factor is included to account for imperfections in the windings on the bobbin. The area occupied by the bobbin in the window, using simple geometry, can be determined as:

$$W_b = W_{bob} K_2 W_w, \quad (3.84)$$

where W_{bob} is the thickness of the bobbin wall. Hence, the window is required to be large enough to accommodate the windings and the bobbin. This requirement is formulated as a constraint given by:

$$K_2 W_w^2 > W_a + W_b. \quad (3.85)$$

- In order to prevent the inductor core from running into saturation, the dimensions of the inductor should be such that the maximum allowable saturation flux density for a ferrite core material, $B_{sp} = 0.3 \text{ T}$, is not exceeded. The maximum flux density is determined as the ratio of the maximum flux to the area of cross section of the center leg. Hence, this constraint is given by:

$$B_{sp} > \frac{\Phi_{pk}}{A_{Cw}} = \frac{(\psi_{pk}/n)}{K_1 C_w^2} = \frac{(LI_{L(pk)}/n)}{K_1 C_w^2}. \quad (3.86)$$

By solving the inductor-level design problem, we can compute the minimum inductor weight as a function of L and $I_{L(pk)}$. Before trying to solve the overall filter design problem, the lower-level optimization problem must be solved for a range of different L and $I_{L(pk)}$ values and the results stored in a design database. Using the data stored in the database, response surface methodologies are used to construct a simple function (usually a polynomial) that approximates the inductor weight as a function of L and $I_{L(pk)}$.

Once the response surface function is obtained, the upper-level optimization problem can be run and the filter can be designed. Whenever the weight of any of the three inductors is required, L and $I_{L(pk)}$ are inserted into the response surface function and the required weight is efficiently computed.

Given the existence of the response surface function, the number of design variables in the present filter design problem is reduced from eighteen to six. Likewise, the number of constraints is reduced from twenty (five for each of the three inductors + the five from the filter as a whole) to five. This means that individual filter optimization problems can now be solved more efficiently and reliably. Filter design studies (which may entail solving a large number of filter optimization problems, each corresponding to different operating conditions, etc.) are more efficient as well, as the same inductor database can be reused for each optimization problem. In fact, the design database can potentially be reused for any electrical component that contains inductors.

Sample Results

In this section, preliminary results illustrating the global/local inductor design methodology are presented. First, the filter optimization problem was solved without any global/local decomposition. These results are presented in Table 3.18 (these results differ from those presented in section 3.3 because (1) a different current density for copper was used, (2) a slightly more accurate expression for L in terms of the inductor design variable was used). It should be noted that it took a number of different optimization "runs" to obtain these results – the optimization problem was very slow to converge especially with respect to the detailed inductor design variables. The detailed inductor design variables in Table 3.18 correspond to $L_1=25.6 \mu H$, $L_2=283.5 \mu H$, and $L_d=17.9 \mu H$.

Table 3.18 - Optimal filter design (no decomposition)

Variable Name	Value
C_1	$7.82 \mu F$
C_2	$31.96 \mu F$
R_d	$21.95 \mu F$
n_d	2.47
A_{cpd}	$.940 \times 10^{-6} m^2$
C_{wd}	$.287 \times 10^{-2} m^2$
W_{wd}	$.521 \times 10^{-2} m^2$
l_{gd}	$.504 \times 10^{-3} m^2$
N_1	3.00
A_{cpl}	$.144 \times 10^{-5} m^2$
C_{wl}	$.388 \times 10^{-2} m^2$
W_{wl}	$.679 \times 10^{-2} m$
l_{gl}	$.953 \times 10^{-3} m^2$
N_2	8.24
A_{cp2}	$.108 \times 10^{-5} m^2$
C_{w2}	$.681 \times 10^{-2} m^2$
W_{w2}	$.941 \times 10^{-2} m$
l_{g2}	$.200 \times 10^{-2} m^2$
Weight	0.151 kg

Next, the local inductor design problem was solved for different combinations of L and $I_{L(pk)}$ and the results were stored in a local design database. A third order polynomial in two dimensions was fit to the data; this polynomial approximates the optimal inductor weight as a function of L and $I_{L(pk)}$. This polynomial was then used in conjunction with the global design problem to generate the optimal filter design shown in Table 3.19.

Table 3.19 - Optimal filter design obtained using global/local methodology

Variable Name	Value
C_1	$7.79 \mu F$
C_2	$30.54 \mu F$
R_d	$22.61 \mu F$
L_1	$26.15 \mu H$
L_2	$277.44 \mu H$
L_d	$18.36 \mu H$
weight	0.153 kg

These results agree closely with those presented in Table 3.18, and were obtained with considerably less computational effort.

3.6.3. Future Work: Three-Level Filter Design Problem

4. Analysis and Optimization of Smart Actuators

The study of smart actuators in this research effort is limited to piezoelectric actuators used for active vibration control of aircraft surfaces. The study is motivated by the application of piezoelectric actuators for alleviating the “tail buffeting” problem in a twin tail aircraft [10]. The buffet loads acting on the tail surface cause excessive wear and tear that significantly reduce the lifetime of the aircraft and increase repair and maintenance costs. Piezoelectric actuators mounted at the root of the tail and on the surface are controlled to actively suppress the effect of the buffet loads on the tail surface. These actuators are electrically capacitive elements so that the load presented to the DC bus is almost purely reactive. Strain is induced in the actuation material by cycling charge in and out of the actuator. The drive electronics must be carefully designed, as these reactive loads require a significant amount of electrical energy to be cycled between the actuator and electronics. Furthermore, these materials also support reverse power flow by changing mechanical energy into electrical energy.

A detailed electromechanical model of a piezoelectric actuator is developed in this section. A simple mass-spring-damper system is used as the coupled mechanical structure. The linear model of the actuator is developed from the linear piezoelectric, constitutive equations. Modifications to the linear model to account for the anhysteretic nonlinearity between the polarization and the electric field are then included to develop the nonlinear model.

4.1 Modeling of the Actuator and Structure

The electromechanical model of the piezoelectric actuator coupled to a simple mechanical structure is developed in this section. The linear, constitutive equations of the actuator are used to develop the model. This model can be directly coupled to the dynamic model of the amplifier. Modifications to the linear model to account for the anhysteretic nonlinearity between the polarization and the electric field in the actuator are described.

The mechanical model of the actuator-structure is represented by a simple mass-spring-damper system acted on by a disturbance force f_{ext} as shown in Figure 4.1.

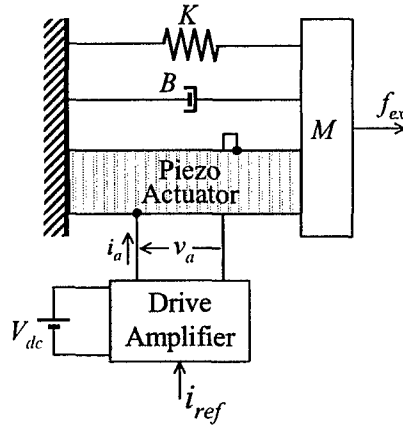


Figure 4.1. Schematic of amplifier driving the actuator-structure

A drive amplifier operating off a fixed dc voltage V_{dc} provides the power to the piezoelectric actuator. The coordinate system and the forces acting on the mass M are identified in Figure 4.2 where f_a is the force exerted by the actuator on the mass.

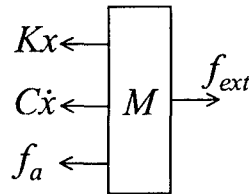


Figure 4.2. Freebody diagram of the mass

The equation of motion can then be written as:

$$M\ddot{x} + B\dot{x} + Kx = f_{ext} - f_a. \quad (4.1)$$

A block diagram representation of Equation (4.1) is shown in Figure 4.3.

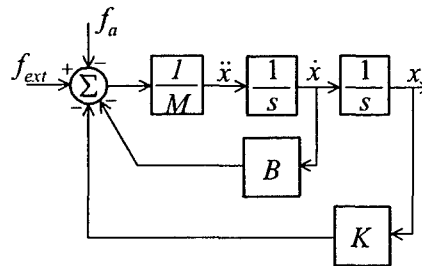


Figure 4.3. Block diagram representation of structure

The electromechanical model of the actuator is determined in the following. We assume that the actuator has a multilayered stack configuration as shown in Figure 4.4. Each layer is rectangular with width w , length l and thickness d . The actuator is formed by stacking n of these layers together. Contiguous layers are polarized in opposite directions and the voltage is applied to the layers as shown in Figure 4.4.

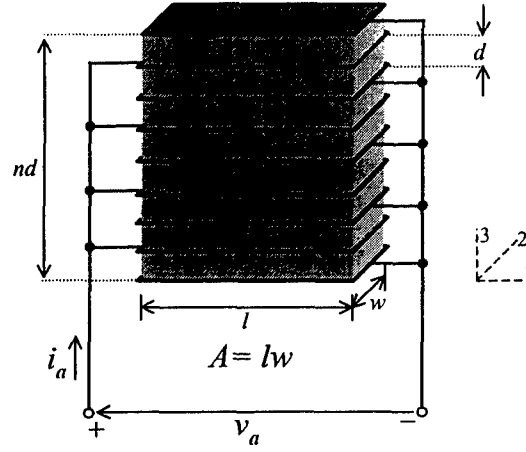


Figure 4.4. Actuator Configuration

The one-dimensional, linear, coupled, electromechanical, constitutive relations between the strain S_3 , stress T_3 , electric field E_3 , and electric displacement D_3 , are:

$$\begin{aligned} D_3 &= \epsilon_{33}E_3 + d_{33}T_3 \\ S_3 &= d_{33}E_3 + \frac{1}{Y_{33}}T_3, \end{aligned} \quad (4.2)$$

where ϵ_{33} is the dielectric permittivity, Y_{33} is elastic modulus and d_{33} is the transverse piezoelectric charge constant. The first index in the subscripts indicates the direction of the electrical component and the second index indicates the mechanical direction. The first equation in Equation (4.2) states that the electric displacement or polarization is the superposition of the direct piezoelectric effect and the applied field times the permittivity. The second equation states that the strain is the superposition of Hooke's law and the indirect effect where a mechanical deformation is caused due to the application of an electric field.

Using the geometry of the actuator, we can use Equation (4.2) to express the relationship between charge and voltage. Noting that charge is displacement per unit area, and electric field is voltage per unit length, the charge q_l entering each layer can be obtained as:

$$\frac{1}{lw}q_l = \epsilon_{33}\frac{v_a}{d} + d_{33}T_3. \quad (4.3)$$

Rewriting this equation we obtain:

$$\begin{aligned} q_l &= \epsilon_{33}\frac{lw}{d}v_a + d_{33}lwT_3 \\ &= C_l v_a + d_{33}lwT_3, \end{aligned} \quad (4.4)$$

where C_l represents the capacitance of each layer and v_a is the voltage across the terminals of the actuator. The total charge entering all the n layers of the actuator is then given by:

$$q = nq_l = nC_l v_a + d_{33}nlwT_3. \quad (4.5)$$

Solving Equation (4.3) for the voltage v_a we obtain:

$$v_a = \frac{1}{nC_l} q - \frac{d_{33}}{\epsilon_{33}} dT_3 = \frac{1}{C} q - \frac{d_{33}}{\epsilon_{33}} dT_3, \quad (4.6)$$

where

$$C = nC_l = \epsilon_{33} \left(\frac{nlw}{d} \right).$$

From Equation (4.6) the voltage across a piezoelectric actuator is the resultant of two components: 1) the direct capacitive effect, and 2) a contribution from the mechanical stress. Next we replace electric field by the voltage in the second equation in Equation (4.2) and substitute in voltage from Equation (4.6). We obtain

$$\begin{aligned} S_3 &= d_{33}E_3 + \frac{1}{Y_{33}}T_3 = d_{33} \frac{v_a}{d} + \frac{1}{Y_{33}}T_3 = \frac{d_{33}}{d} \left(\frac{1}{C} q - \frac{d_{33}}{\epsilon_{33}} dT_3 \right) + \frac{1}{Y_{33}}T_3 \\ &= \frac{1}{nlw} \frac{d_{33}}{\epsilon_{33}} q + \left(1 - \frac{Y_{33}d_{33}^2}{\epsilon_{33}} \right) \frac{1}{Y_{33}}T_3 \\ &= \frac{1}{nlw} \frac{d_{33}}{\epsilon_{33}} q + (1 - k^2) \frac{1}{Y_{33}}T_3. \end{aligned} \quad (4.7)$$

The electromechanical coupling coefficient k^2 is:

$$k^2 = \frac{Y_{33}d_{33}^2}{\epsilon_{33}}. \quad (4.8)$$

This constant is defined as the fraction of the input electrical energy that is mechanically deliverable.

To enter these equations into the block diagram, we rewrite Equation (4.7) as:

$$T_3 = \frac{Y_{33}}{1 - k^2} \left(S_3 - \frac{1}{nlw} \frac{d_{33}}{\epsilon_{33}} q \right). \quad (4.9)$$

The block diagram corresponding to these relationships is shown in Figure 4.5. The displacement in the structure induces a strain in the actuator according to

$$S_3 = K_1 x. \quad (4.10)$$

Similarly, the force applied to the structure by the actuator is derived from the stress in the actuator according to

$$f_a = K_2 T_3. \quad (4.11)$$

The constants K_1 and K_2 depend on the coupling between the actuator and the structure. They are determined by the location of the actuator, configuration of the actuator, bonding layers, modal coupling coefficients of the structure, and other factors.

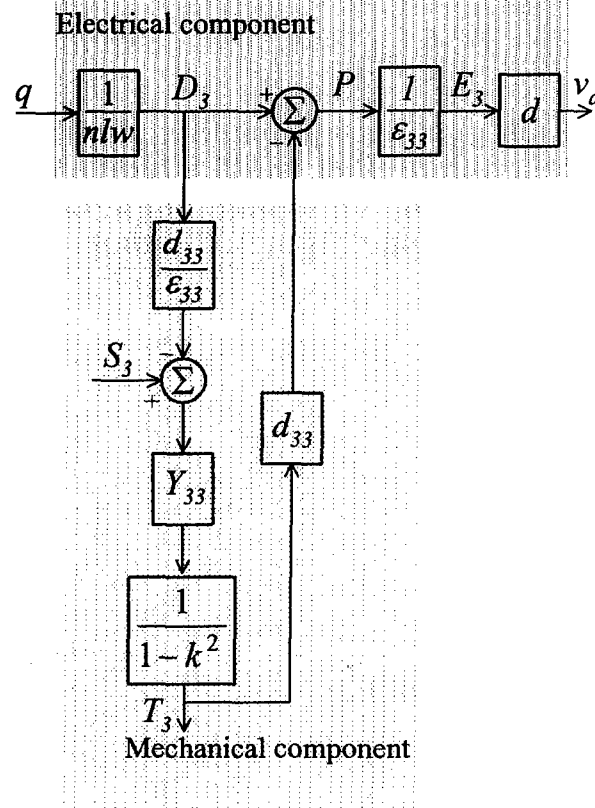


Figure 4.5. Electromechanical model of piezoelectric actuator

If we interpret the physical system represented by Figure 4.54 to be a stacked actuator (Figure 4.4) bonded rigidly to a mass, then the constants K_1 and K_2 are given by:

$$K_1 = \frac{1}{nd} \quad (4.12)$$

$$K_2 = lw.$$

Equations (4.10) and (4.11) allow us to couple the actuator equations in Figure 4.5 to the dynamics of the structure in Figure 4.3. The complete model is shown in Figure 4.6. The model shown in Figures 4.5 and 4.6 has been derived from the linear, coupled

constitutive equations (Equation (4.2)). The modifications in the model to account for the anhysteretic nonlinearity between the polarization and the electric field are described in the following section.

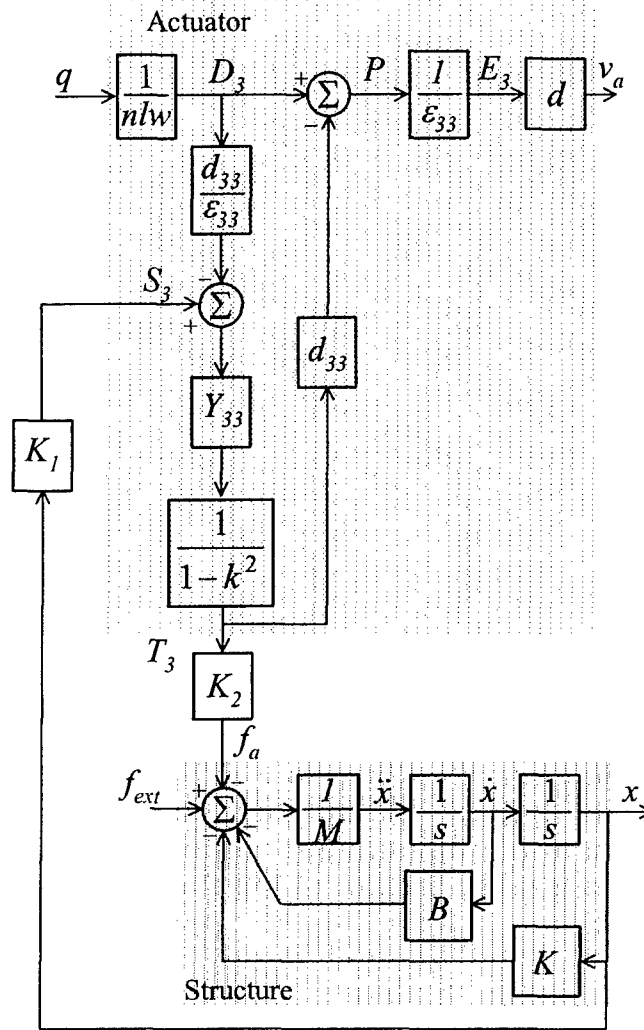


Figure 4.6. Complete electromechanical model of actuator-structure

4.1.1. Anhysteretic Nonlinearity

In the absence of interdomain coupling, the anhysteretic nonlinearity according to the Ising spin model between the polarization P , and the electric field E_3 , in the actuator is given by [11]:

$$P = P_s \tanh\left(\frac{E_3}{a}\right), \quad (4.13)$$

where P_s is the saturation polarization of the material of the actuator and a is a scaling electric field. However, in the block diagram shown in Figure 4.6 electric field in the actuator is determined from the polarization. Hence, inverting the nonlinearity given by

Equation (4.13) to conform to the block diagram shown in Figure 4.6, the electric field is determined as:

$$E_3 = a \tanh^{-1} \left(\frac{P}{P_s} \right). \quad (4.14)$$

This nonlinearity is shown graphically in Figure 4.7.

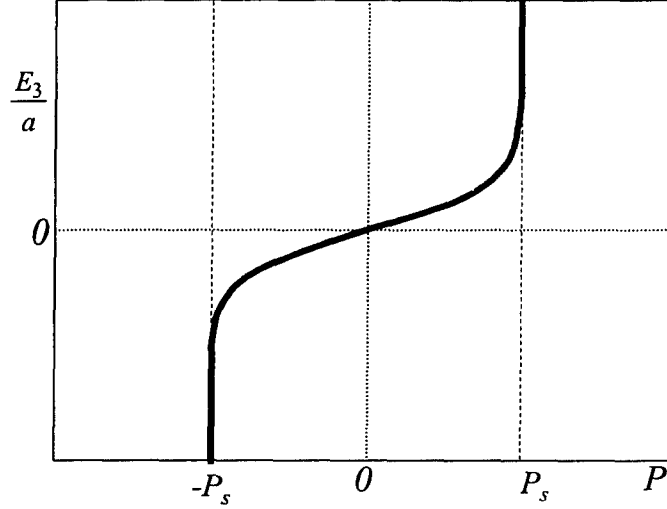


Figure 4.7. Inverse nonlinearity between polarization and electric field

The block diagram of the electromechanical model of the actuator and the structure with the nonlinearity is shown in Figure 4.8. Under the assumption that the polarization p , does not exceed the saturation polarization P_s a power series expansion can be used to represent the nonlinearity given by Equation (4.14). This power series expansion for the electric field is given by:

$$E_3 = a \left[\left(\frac{P}{P_s} \right) + \frac{1}{3} \left(\frac{P}{P_s} \right)^3 + \frac{1}{5} \left(\frac{P}{P_s} \right)^5 \right]. \quad (4.15)$$

The actuator model can be represented as a cascade combination of a linear transfer function between the charge and polarization and the nonlinearity between the polarization and the voltage as shown in Figure 4.9.

the polarization can be represented as

$$P(t) = P_m \cos(\omega t + \phi). \quad (4.17)$$

The voltage v_a , at the terminals of the actuator, from Figure 4.9, is then given by:

$$v_a(t) = d \left[\left(\frac{P_m}{P_s} \right) \cos(\omega t + \phi) + \frac{1}{3} \left(\frac{P_m}{P_s} \right)^3 \cos^3(\omega t + \phi) + \frac{1}{5} \left(\frac{P_m}{P_s} \right)^5 \cos^5(\omega t + \phi) \right]. \quad (4.18)$$

Using trigonometric identities it can be easily shown that v_a consists of the fundamental, third and fifth harmonics and can be expressed as:

$$v_a(t) = d \left[V_{m1} \cos(\omega t + \phi) + V_{m3} \cos(3\omega t + 3\phi) + V_{m5} \cos(5\omega t + 5\phi) \right], \quad (4.19)$$

where

$$\begin{aligned} V_{m1} &= \frac{1}{8} \left[8 \left(\frac{P_m}{P_s} \right) + 2 \left(\frac{P_m}{P_s} \right)^3 + \left(\frac{P_m}{P_s} \right)^5 \right] \\ V_{m3} &= \frac{1}{96} \left[8 \left(\frac{P_m}{P_s} \right)^3 + 6 \left(\frac{P_m}{P_s} \right)^5 \right] \\ V_{m5} &= \frac{1}{80} \left(\frac{P_m}{P_s} \right)^5. \end{aligned} \quad (4.20)$$

4.2 OPTIMIZATION OF THE DRIVE AMPLIFIER

The formulation of an optimization problem for the design of the drive amplifier for the piezoelectric actuator is the subject of this section. Switching power amplifiers are beginning to be recognized as promising alternatives for driving piezoelectric actuators [12-17]. It was shown in the previous section that these actuators exhibit capacitive electrical characteristics. In addition, it was shown that these actuators exhibit a hysteretic nonlinearity between the polarization and the electric field. Due to the reactive undamped electrical characteristics of the actuator, the drive amplifier is required to process almost zero real power and a considerable amount of reactive power circulates between the actuator and the amplifier.

The use of switching power amplifiers for driving piezoelectric actuators was discussed in [12-17]. High voltage switching amplifiers for piezoelectric actuators are discussed in [12,13]. The switching amplifiers for electrostrictors are reported in [14]. It has been noted that charge and current controlled amplifiers naturally reduce the distortion induced by the nonlinearities of the piezoelectric actuator [17,18]. A similar result for

electrostrictor actuators has been reported in [15,16]. This reduced distortion can have beneficial effects on the performance of the control system. Hence, the drive amplifier discussed in this section is configured as a current controlled amplifier. The topology of the amplifier chosen is that of a single-phase DC-AC inverter with a filter inductor connected on the AC side. The switching devices in the amplifier are controlled using the principle of pulse width modulation.

Optimization of drive electronics for piezoelectric actuators was addressed in [19]. However, a well-defined optimization procedure that takes into account the nonlinear characteristics of the actuator and yields physically meaningful designs of the individual components of the amplifier has not been proposed. The optimization formulation presented in this section is a first step in this direction.

4.2.1. Problem Definition

A switching amplifier driving a piezoelectric actuator attached to the structure is shown in Figure 4.10. The goal of the optimization procedure is to design the amplifier such that it has minimum weight for the given actuator and structure. It is assumed that the amplifier is configured as a current controlled amplifier. That is, the actuator is controlled by controlling the current flowing into it that is proportional to i_{ref} . (The actuator is not controlled by the voltage across it.)

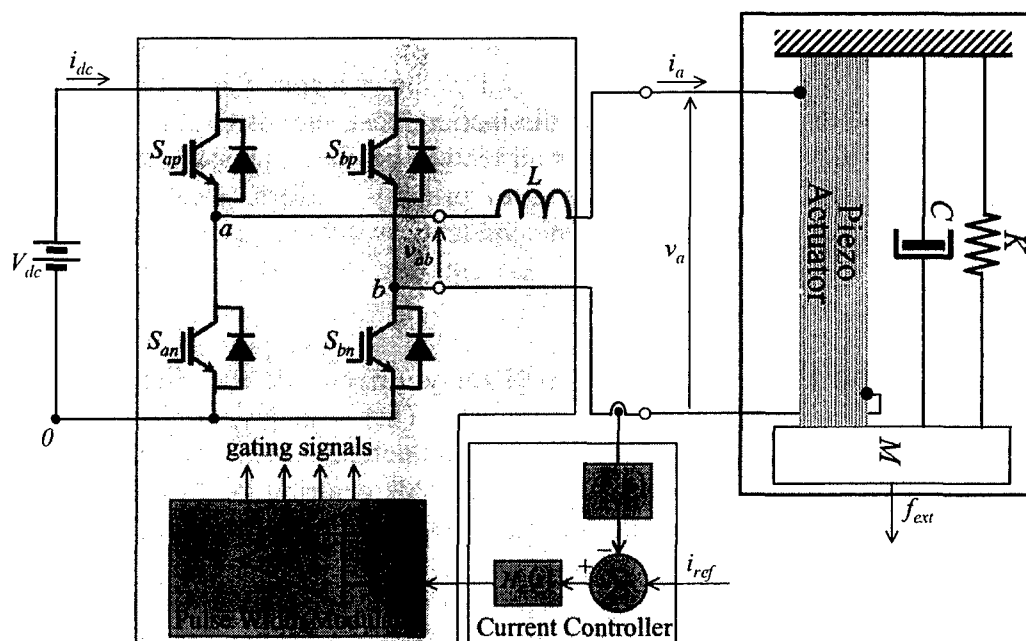


Figure 4.10. System Under Consideration

In the frequency domain, this performance specification is defined in the form of a transfer function shown in Figure 4.11.

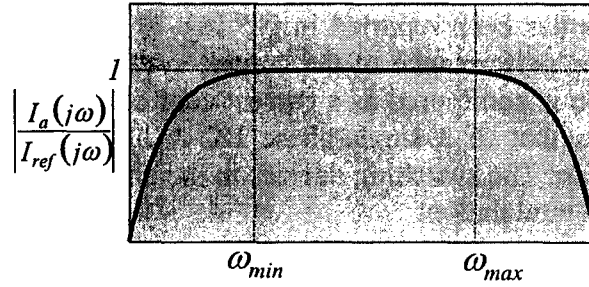


Figure 4.11. Regulation Specifications of Current Controller

It can be seen that the zero frequency is excluded from the passband in this amplifier topology. Clearly, this specification defines the frequency band over which the structure can be controlled. This data is part of the problem definition including frequencies ω_{min} and ω_{max} , which define the bandwidth of operation.

The amplifier is required to be able to drive the actuator to full stroke over the entire operational frequency range. Since the constitutive equations of the piezoelectric material has a saturation characteristic, this assumption implies that the amplifier must be able to deliver a maximum current over all frequencies in the bandwidth of the amplifier. This maximum current will be calculated below using a nonlinear model of the piezoelectric constitutive equations. This maximum current determines the required value of the bus DC voltage.

The main components of the amplifier are: 1) the switching power devices with the pulse width modulator, 2) the current controller, and 3) the inductor. Several implementation issues including voltage ratings, thermal dissipation, cost, etc. drive the selection of the power devices. However, these transistors all tend to be about the same size and weight. Since the performance of the amplifier is of primary concern, ideal switches in the optimization formulation replace the semiconductor switching devices. Hence, thermal considerations such as the design of the heat sink are excluded from the optimization problem.

The design of the current controller is largely driven by the frequency domain requirement on the amplifier given in Figure 4.11. That is to say, the current controller can be readily determined once the value of the inductance is known. Furthermore, the components of the current controller have a negligible contribution to the weight of the amplifier. Therefore, the current controller is also excluded from the optimization.

Hence the optimization problem presented in this section is specifically focused on the design of the inductor. Indeed, the inductor is by far the largest component over which the designer has control, and its value is impacted by the other parameters of the amplifier. Similar to the optimization of the sample system described in Section 3, the actual physical design of the inductor is considered, not only the selection of the inductance value.

The power transistor switches are used to control the average voltage and current that is delivered to the actuator. Due to the switching of these transistors, a ripple voltage and a

ripple current ride on top of these average waveforms. This ripple current acts as a disturbance signal on the actuator causing high frequency excitation and unwanted heating in the actuator. The magnitude of the ripple current is determined by the inductor size and the switching frequency of the amplifier. In the optimization process the maximum allowable ripple current is a constraint.

The formulation of the optimization problem consists of the following steps:

- Modeling the actuator and the amplifier
- Calculation of the DC bus voltage and current ripple
- Identification of the design variables
- Definition of the optimization constraints
- Definition of the objective function

Each of these steps is described in detail in the following sections.

It is straightforward to formulate the optimization problem. The main challenge is the determination of the current ripple. The current ripple can be ascertained from a simulation of the system in Figure 4.10, which includes the switching dynamics of the semiconductor power devices. These simulations are, however, computationally very expensive. Any optimization methodology that includes such a simulation would take prohibitively long to run. Therefore, it is necessary to develop a computationally cheap estimate of the switching ripple. A substantial amount of this section is devoted to this task.

4.2.2. Model Development

The development of the coupled nonlinear electromechanical model of the actuator and the structure to be used for the optimization problem was described in the previous section. The modeling of the drive amplifier shown in Figure 4.10 is briefly described in this section. The modulation algorithm and the switching waveform, which it engenders, are discussed. Then a simpler, “average” model of the power stage is introduced. A detailed description of the drive amplifier used in this discussion is shown in Figure 4.12.

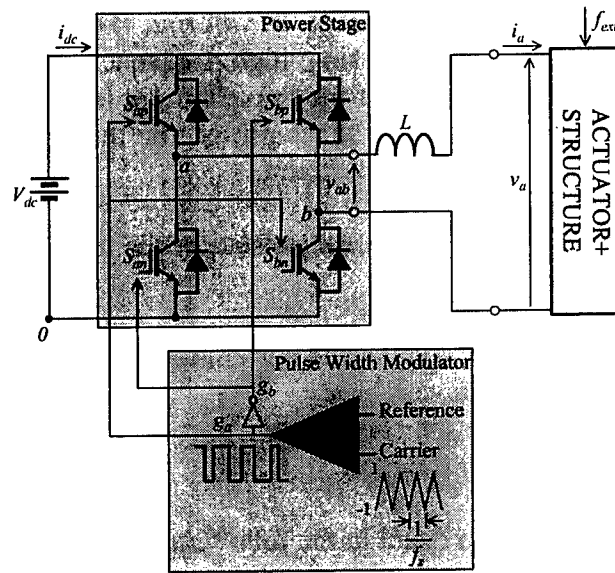


Figure 4.12. Single phase DC-AC inverter driving the actuator

In this amplifier, the current driving the piezoelectric actuator is synthesized by pulse width modulating the voltage from the DC source by appropriately controlling the semiconductor switches with the pulse width modulator. The inductor (in conjunction with the capacitive actuator load) filters the pulse width modulated voltage to deliver a current to the load that contains a fundamental component that is proportional to the reference input signal and that contains an acceptably small ripple.

A bipolar voltage v_{ab} , is synthesized from the DC voltage source V_{dc} , by operating the switches S_{ap} , S_{an} , S_{bp} and S_{bn} according to a technique called pulse width modulation (PWM)[20]. A reference signal is modulated with a triangular wave called the carrier signal as shown in Figure 4.13.

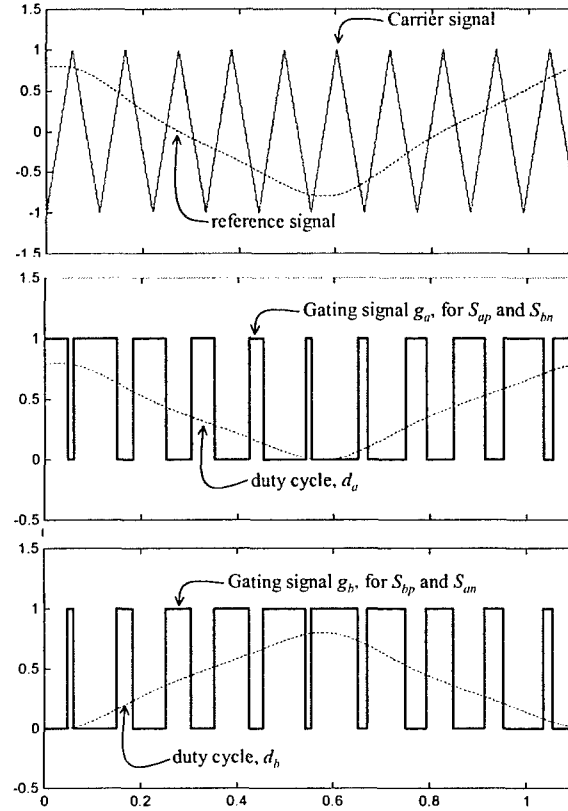


Figure 4.13. Pulse Width Modulation (PWM)

The frequency of the carrier signal is the switching frequency of the amplifier. The signals g_a and g_b are the gating signals generated by the pulse width modulator to drive the four switches of the amplifier. The gating signal g_a , turns on the switches S_{ap} and S_{bn} when the reference signal becomes greater than the carrier signal and turns them off when the reference signal becomes lesser than the carrier. The gating signal g_b , for S_{bp} and S_{an} is the logical inverse of the drive signal to S_{ap} and S_{bn} . The voltage v_{ab} , shown in Figure 4.14, at the output of the amplifier is then given by:

$$v_{ab} = \begin{cases} V_{dc} & \text{when } S_{ap} \text{ and } S_{bn} \text{ are on} \\ -V_{dc} & \text{when } S_{bp} \text{ and } S_{an} \text{ are on} \end{cases} \quad (4.21)$$

$$= g_a V_{dc} - g_b V_{dc}.$$

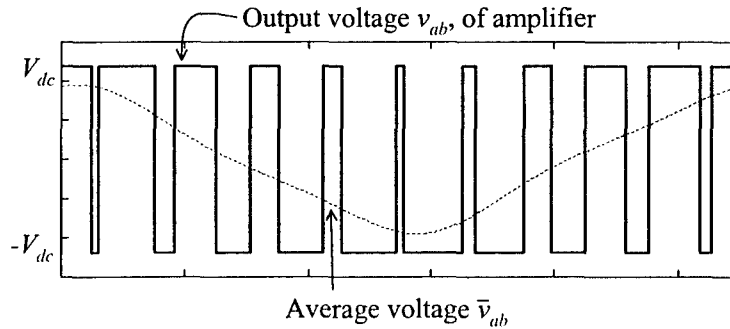


Figure 4.14. Pulse width modulated voltage v_{ab} and its average value \bar{v}_{ab}

The duty cycle of the gating signal is the fraction of the period for which the gating signal is high. The average value of the amplifier output can be obtained from (4.21) by replacing the control signals for the switches with the equivalent duty cycles of the gating signals as follows:

$$\bar{v}_{ab}(t) = (d_a(t) - d_b(t))V_{dc} = d_{ab}(t)V_{dc}. \quad (4.22)$$

From Equation (4.22), it can be seen that the duty cycles d_a and d_b can be replaced by a single duty cycle d_{ab} which multiplies the input DC voltage to obtain the average of the output voltage of the amplifier. Since the duty cycle d_{ab} cannot exceed unity, the maximum amplitude of the average value of the output voltage is equal to V_{dc} .

A typical waveform of this actuator current i_a is shown in Figure 4.15 where it is assumed that the reference input signal is sinusoidal.

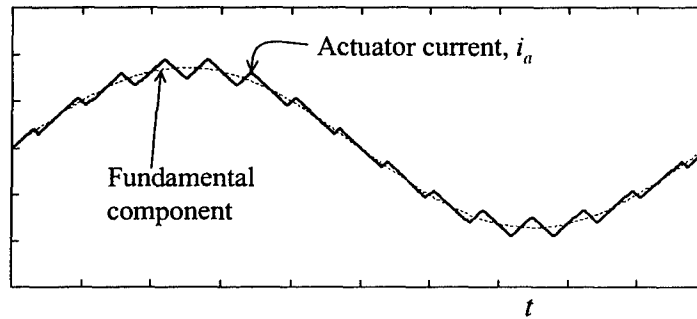


Figure 4.15. Typical waveform of current generated by the drive amplifier

It can be seen that the actuator current is nearly sinusoidal at the reference frequency. The deviation of the actual current from the desired fundamental component is called the switching ripple. It can be also shown that the average value of the input current to the amplifier is given by:

$$\bar{i}_{dc}(t) = d_{ab}(t)i_a(t) \quad (4.23)$$

Average Model of Amplifier

In order to incorporate a model of the switching amplifier into the optimization process, it is necessary to replace the switches to make the model computationally tractable. This simplified model, called an average model, neglects the switching ripple in the currents and voltages and reduces the model to a set of relationships between the average waveforms. This model is valid only over frequency ranges significantly lower than half the switching frequency of the amplifier [4]. The average model is shown in Figure 4.16.

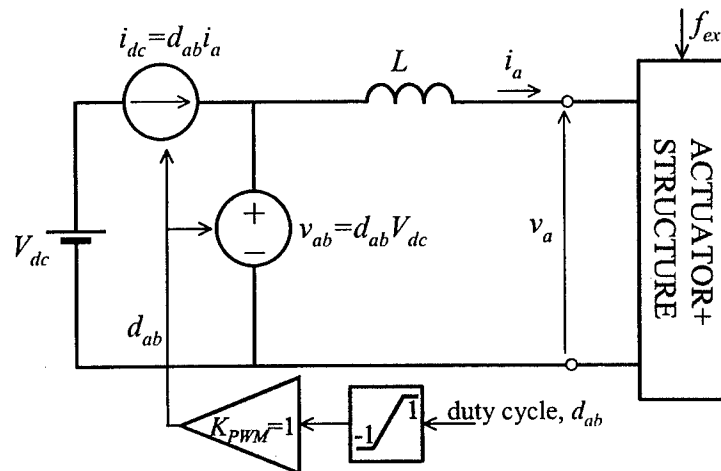


Figure 4.16. Average model of amplifier driving the actuator

A transfer function representation of the amplifier can be very easily obtained from the average model. A control block diagram representation coupling the models of the amplifier and the actuator is shown in Figure 4.17.

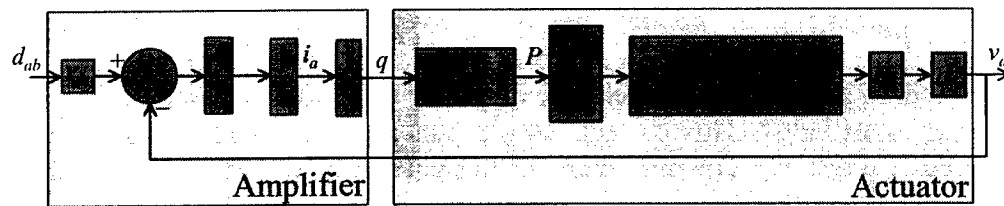


Figure 4.17. Block diagram of amplifier coupled to the actuator

The final component of the amplifier is the current controller. The block diagram of the closed loop system with a generic representation of the current controller is shown in Figure 4.18.

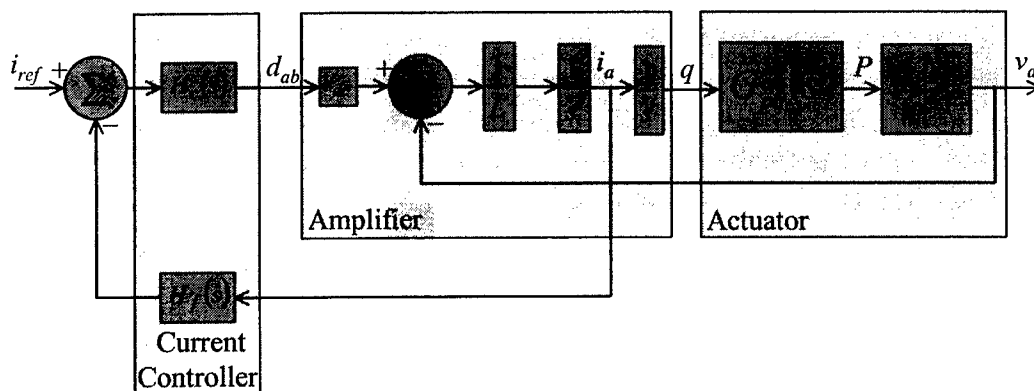


Figure 4.18. Block diagram of amplifier and actuator with current controller

This controller uses the current into the actuator as feedback to create an error signal with a reference input signal. The duty cycle command is then synthesized from the error signal. The current controller ensures that the fundamental component of the actuator

current follows the reference over the regulation bandwidth of the amplifier. In the analysis that follows, it is assumed that the fundamental component of the actuator current is identical to the reference current command.

The controller uses the current into the actuator as feedback to create an error signal with the reference input signal. The duty cycle command is then synthesized from the error signal. The design of the current controller depends on the inductance L , actuator specifications, DC input voltage V_{dc} and the switching frequency f_s . Given these parameters of the amplifier and the actuator, it is a straightforward exercise to design the current controller.

In most cases, the current controller can be implemented with analog operational amplifier circuits, whose weight is negligible compared to the weight of the overall system. Furthermore, the weight of the current controller is independent of the control gains. Therefore, the design of the current controller is excluded from the optimization formulation.

4.2.3. Determination of DC Bus Voltage

One of the requirements of the amplifier is to drive the actuator to full stroke over the bandwidth of the system. This requirement implies that the amplifier must produce enough current to saturate the piezoelectric amplifier when the duty cycle of the amplifier is at its maximum value. This current requirement, in turn, places a restriction on the minimum bus voltage V_{dc} . The minimum DC bus voltage is related to the inductance, and a simple expression that describes this relationship is required for the optimization methodology. The average model of the amplifier is used to determine the DC bus voltage neglecting the switching ripple in the actuator current and the voltage. This assumption is validated by the fact that the electromechanical power transfer between the amplifier and the actuator predominantly occurs at the frequency of the reference sinusoidal current, which is much lower than the switching frequency. The determination of the DC bus voltage goes through the following steps. First, the maximum current drawn by the actuator is determined. From this current, the voltage across the actuator using the nonlinear model is determined. The amplifier output voltage \bar{v}_{ab} , is then calculated as the sum of the actuator voltage and the voltage drop across the inductance. The DC bus voltage is finally determined such that the duty cycle does not exceed unity when \bar{v}_{ab} reaches its maximum amplitude.

A simplified block diagram of the average model of the amplifier and the actuator with the nonlinearity is shown in Figure 4.19.

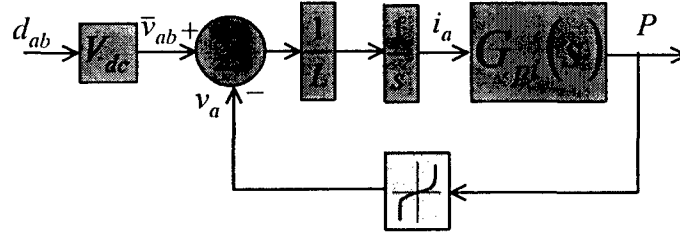


Figure 4.19. Simplified block diagram of amplifier-actuator with nonlinearity

To start with, it is assumed that the reference current command is selected to drive the actuator at its maximum deflection. As mentioned in the previous section, the current controlled amplifier is configured such that the fundamental component of the actuator current is identical to the reference current (Figure 4.11). Let this sinusoidal current be given by:

$$i_{ref}(t) = I_{max} \cos(\omega_F t) = i_a(t), \quad (4.24)$$

where ω_F is the frequency that results in the maximum deflection. From Figure 4.19, it can be seen that the actuator current and polarization are linearly related by a transfer function $G_{pi}(j\omega)$, whose magnitude response is shown in Figure 4.20. Hence, for the actuator current given by Equation (5.4), the polarization can be expressed as:

$$P(t) = P_s \cos(\omega_F t + \phi), \quad (4.25)$$

since the actuator is being driven to its maximum deflection.

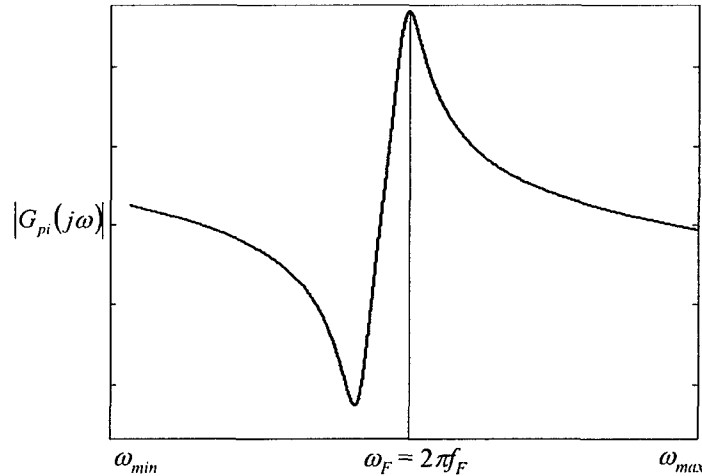


Figure 4.20. Actuator current to polarization transfer function

(In this case, the amplifier bandwidth is assumed to include the mechanical resonant frequency of the structure.) Using the relationship in Figure 4.20 between the current and polarization, the maximum current amplitude can be obtained as:

$$I_{\max} = \frac{P_s}{G_{PI}(j\omega_F)} \quad (4.26)$$

The next step is to determine the voltage across the actuator using the nonlinear constitutive equations of the piezoelectric material. Given the polarization in Equation (4.25) the actuator voltage, due to the nonlinearity, consists of the fundamental, third and fifth harmonics according to Equations 4.18, 4.19 and 4.20, because of the nonlinearity. Substituting $P_m = P_s$ in Equation (4.20), we obtain:

$$v_a(t) = d a \left[\frac{11}{8} \cos(\omega_F t + \phi) + \frac{7}{48} \cos(3\omega_F t + 3\phi) + \frac{1}{80} \cos(5\omega_F t + 5\phi) \right] \quad (4.27)$$

The voltage \bar{v}_{ab} , at the output of the amplifier is the sum of the actuator voltage and the drop across the inductor given by. This is given by:

$$\bar{v}_{ab}(t) = L \frac{di_a(t)}{dt} + v_a(t). \quad (4.28)$$

Substituting for $i_a(t)$ from Equation (4.24) and for $v_a(t)$ from Equation (4.27), we obtain:

$$\begin{aligned} \bar{v}_{ab}(t) = d a \left[\frac{11}{8} \cos(\omega_F t + \phi) + \frac{7}{48} \cos(3\omega_F t + 3\phi) + \frac{1}{80} \cos(5\omega_F t + 5\phi) \right] \\ + \omega L I_{\max} \sin(\omega_F t). \end{aligned} \quad (4.29)$$

It can be seen from Equation (4.29) that, in order to guarantee the sinusoidal actuator current given by Equation (4.24), the current controller (Figure 4.18) needs to synthesize a duty cycle command d_{ab} , such that the third and fifth harmonic components of the amplifier output voltage \bar{v}_{ab} , are identical to those of the actuator voltage v_a . According to Equation (4.22), the duty cycle $d_{ab}(t)$ can be written as:

$$d_{ab}(t) = \frac{1}{V_{dc}} \bar{v}_{ab}(t). \quad (4.30)$$

The minimum DC bus voltage required is then determined such that the duty cycle given by Equation (4.30) does not exceed its maximum allowable amplitude $d_{ab,\max}$ when the amplifier output voltage \bar{v}_{ab} , reaches its maximum amplitude. The minimum DC bus voltage is hence obtained as:

$$V_{dc} = \frac{1}{d_{ab,\max}} \max [\bar{v}_{ab}(t)]. \quad (4.31)$$

4.2.4. Estimation of Actuator Current Ripple

The next step in the analysis is to determine the current ripple. Specifications on the harmonic content of the actuator current are used as optimization constraints to determine the values of inductance and switching frequency. This analysis is complicated by the nonlinear constitutive equations of the actuator. One approach for determining the current ripple is to directly simulate the nonlinear system. This method is computationally too expensive for optimization, however. Therefore, the size of the current ripple is estimated by computing the amplitudes of the components of the Fourier series of the actuator current.

The switching of the power transistors causes the voltage v_{ab} in Figure 4.14 to be a pulse width modulated square wave. The Fourier decomposition of the voltage v_{ab} can be given as:

$$v_{ab}(t) = \sum_{k=1}^{\infty} V_{abk} \cos(\omega_k t + \vartheta_k). \quad (4.32)$$

A typical harmonic spectrum of the amplifier output voltage is shown in Figure 4.21. The first, third and the fifth harmonics of the voltage v_{ab} , are given by Equation (4.28). Since the actuator current has no third and fifth harmonics, the third and fifth harmonic components of the amplifier output voltage v_{ab} , are identical to those of the actuator voltage v_a , and do not contribute to the ripple in the actuator current. Hence, the ripple in the actuator current is due to the voltage harmonics whose frequencies are in the switching frequency range.

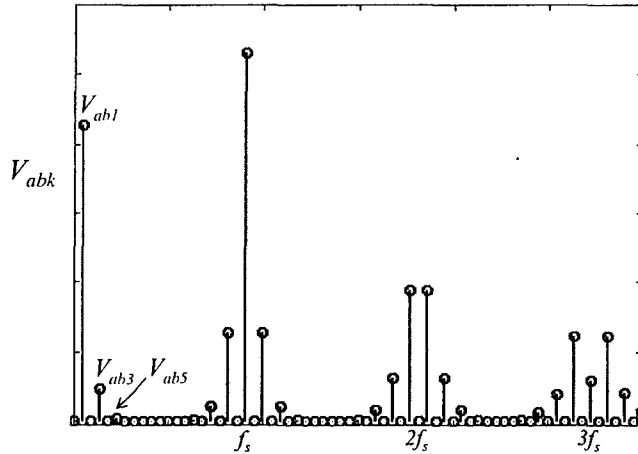


Figure 4.21. Harmonic spectrum of amplifier output voltage v_{ab}

The Fourier decomposition of the actuator current can be expressed as:

$$i_a = I_{\max} \cos(\omega_F t) + \sum_{k=2}^{\infty} I_{ak} \cos(\omega_k t + \theta_k). \quad (4.33)$$

It is assumed that the fundamental component of the actuator current i_a is identical to i_{ref} . The polarization and actuator voltage can also be expressed in a similar fashion as:

$$P(t) = P_s \cos(\omega_F t + \phi) + \sum_{k=2}^{\infty} P_k \cos(\omega_k t + \phi_k) \quad (4.34)$$

$$v_a(t) = \sum_{k=1}^{\infty} V_{ak} \cos(\omega_k t + \varphi_k).$$

The harmonic components of v_a for $k=1,3$ and 5 are given by Equation (4.27). In the following analysis, complex phasor notation of sinusoidal steady state variables is used to determine the Fourier components of the actuator current. Rewriting Equation (4.28) in complex phasor notation:

$$V_{abk} e^{j\vartheta_k} = V_{ak} e^{j\varphi_k} + \omega_k L I_{ak} e^{j\left(\vartheta_k + \frac{\pi}{2}\right)}. \quad (4.35)$$

The amplitudes I_{ak} of the actuator current are then obtained from Equation (5.15) as:

$$I_{ak} = \frac{1}{\omega_k L} \left(V_{abk} e^{j\left(\vartheta_k - \vartheta_k - \frac{\pi}{2}\right)} - V_{ak} e^{j\left(\varphi_k - \vartheta_k - \frac{\pi}{2}\right)} \right). \quad (4.36)$$

To obtain the Fourier series components of the actuator current, the corresponding components of the actuator voltage are required according to Equation (4.36). Typical switching waveforms of the actuator current, actuator voltage and the polarization are shown in Figure 4.22. It can be seen that the polarization and the voltage across the actuator have negligible switching ripple. The reasons for this are explained in the following.

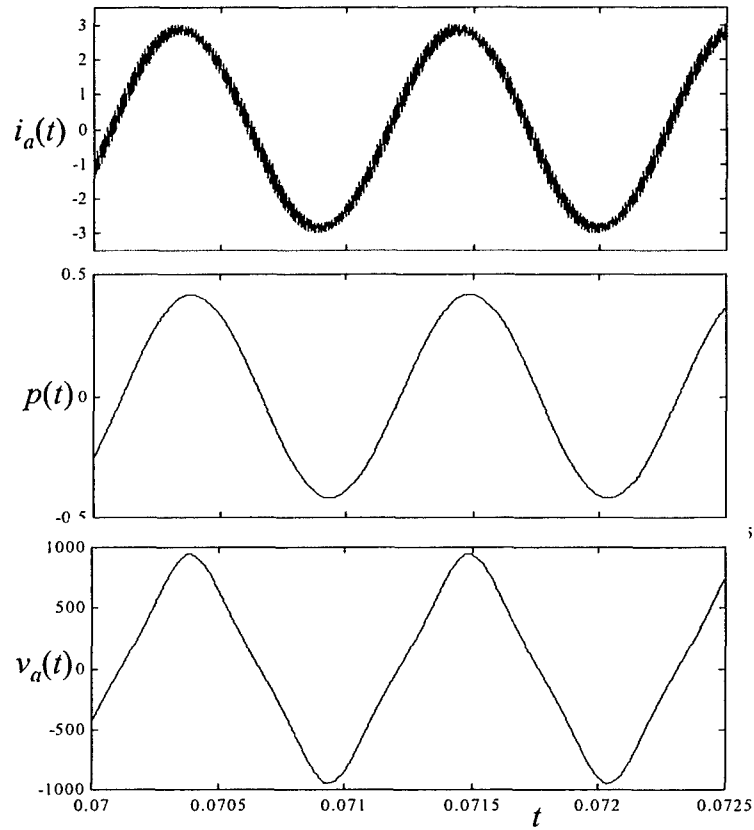


Figure 4.22. Switching waveforms of actuator current i_a , duty cycle d_{ab} , and actuator voltage v_a .

An expanded view of magnitude of the transfer function $G_{pi}(s)$, from the actuator current to the polarization is shown in Figure 4.23. Since the switching frequency has to be significantly higher than ω_{max} , it can be seen from Figure 4.23, that harmonics of the current in the switching frequency range are sufficiently attenuated by the actuator. Hence, it can be assumed that the harmonic components at the switching frequency range of the polarization are equal to zero.

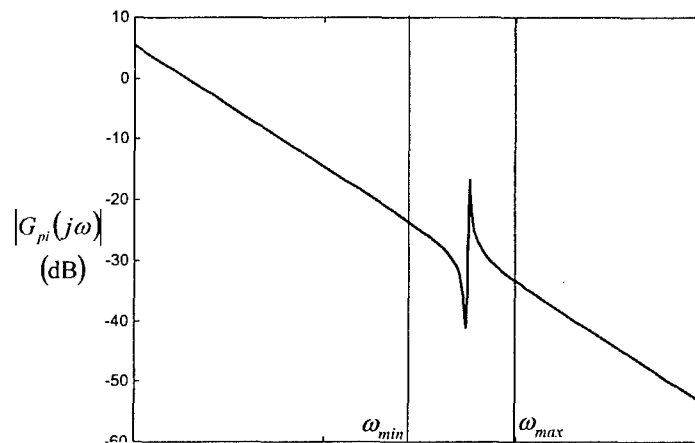


Figure 4.23. Expanded of transfer function $G_{pi}(s)$ from actuator current to polarization

In addition, the actuator voltage can also be assumed to be devoid of any components in the switching frequency range. As a result, we have:

$$\begin{aligned} P_k &= 0 \text{ for } k \geq 2 \\ V_{ak} &= 0 \text{ for } k \geq 6. \end{aligned} \quad (4.37)$$

Hence, (4.36) reduces to:

$$I_{ak} = \frac{1}{\omega_k L} V_{abk} \text{ for } k \geq 6. \quad (4.38)$$

4.2.5. Formulation of optimization problem

The optimization problem is now formulated using the calculations in the previous sections. The design variables are identified, the constraints are set up and the objective function is defined.

Design Variables

The design variables for the optimization problem are the variables associated with the design of the inductor. The inductors are assumed to be typical EE cores as in the optimization formulation of sample system described in Section 3. The design variables associated with the inductor are given in Table 4.1.

Table 4.1. Design variables associated with inductor design

Variable name	Description
n	Number of turns
A_{cp}	Cross sectional area of winding
C_w	Center leg width
W_w	Window width
l_g	Airgap length

Constraints

The optimization constraints are subdivided into performance and physical constraints as explained in the following subsections.

Performance Constraints

The first performance constraint is the maximum allowable current ripple. Because the current ripple is a nonlinear function, the actuator current is expressed as a Fourier series (Equation (4.33)), and then the current ripple is measured as total harmonic distortion.

The *THD* is the percentage ratio of the distortion component of the actuator current to its fundamental component [20]. It is defined as:

$$THD = 100 \frac{I_{dis}}{I_{a1}}, \quad (4.39)$$

where I_{a1} is the rms value of the fundamental component of the actuator current and I_{dis} is the rms value of the distortion component. The fundamental component of the actuator current is assumed to be identical to the reference command. According to Equation (4.33), the distortion component is given by:

$$I_{dis} = \sum_{h=2}^{\infty} \frac{I_{ah}^2}{2}. \quad (4.40)$$

Hence, the *THD* of the amplifier used at full capacity can be expressed as:

$$THD = 100 \sqrt{\frac{\sum_{k=2}^{\infty} I_{ak}^2}{I_{\max}^2}}. \quad (4.41)$$

An upper bound is imposed on the *THD* of the actuator current to size the inductor at the specified switching frequency.

The *THD* of the actuator current is a function of the switching frequency and the amplitude and the frequency of the fundamental component of the actuator current. To begin with, the switching frequency is fixed at a specified value. The amplitude and frequency of the fundamental component of the actuator current are determined from the mechanical model according to Equation (4.26) and Figure 4.20. The average amplifier output voltage \bar{v}_{ab} then is determined for this maximum current amplitude from Equation (4.29). The DC bus voltage is then determined from Equation (4.31) using the maximum duty cycle. For this DC bus voltage the duty cycle d_{ab} , is determined from Equation (4.30). This duty cycle is then modulated with the triangular carrier at the switching frequency as shown in Figure 4.13 to generate the pulse width modulated output voltage v_{ab} as shown in Figure 4.14. The Fourier components V_{abh} , of the pulse width modulated voltage v_{ab} are then determined. Finally, the Fourier series components of the actuator current are determined from Equation (4.36) where the inductance is determined from Equation (3.4). The *THD* of the actuator current is then determined from Equation (4.41).

Physical Constraints

The physical constraints are defined to guarantee physically meaningful dimensions for the core and windings used in the inductor and they are the same as those defined in Section 3.

Objective Function

The objective function is the weight of the inductor determined in a similar fashion to the Section 3. That is,

$$J = W_L. \quad (4.42)$$

The weight of an inductor is determined as the sum of the weights of iron and copper used in the core and windings, respectively:

$$W_L = W_{fe} + W_{cu}. \quad (4.43)$$

4.2.6. Optimization Results

The results of the optimization problem are presented in this section. The bandwidth requirements and relevant specifications of the actuator are given below in Table 4.2.

Table 4.2. Operating Conditions

Variable	Value
Operating bandwidth	$\omega_{min} = 2\pi 700 \text{ rad/sec} < \omega < \omega_{max} = 2\pi 1200 \text{ rad/sec}$
Saturation Polarization, P_s	0.425 C/m^2
Coercive Electric Field, a	6.4 MV/m
Mass of Structure, M	200 kg
Damping of Structure, B	$2.56 \times 10^4 \text{ N-s/m}$
Stiffness of Structure, K	$5.4 \times 10^9 \text{ N/m}$
DC Bus Voltage, V_{dc}	1186 V (determined from Equation (5.11))

Optimization was performed using the VisualDOC optimization software [7] using the Modified Method of Feasible Directions algorithm [8]. The definition of the constraints and the objective function were coded in MATLAB. Constraint derivatives were computed using finite differences. Depending on the initial design used to start the optimization iterations, convergence was obtained within approximately 200 function evaluations. The optimizations were achieved in approximately 10 minutes on a 500 MHz Pentium II PC. For this problem, it was found that there were not any local minima in the design space, and the optimizer converged to the global minima irrespective of the choice of the initial design.

A family of optimal designs was obtained by varying the upper bound on the THD of the actuator current for switching frequencies of 100 kHz and 200 kHz. The inductance values plotted as a function of the THD of the actuator current for the two values of switching frequency is shown in Figure 4.24. It can be seen that the inductance increases as the upper bound on the THD decreases for a given switching frequency. In addition, the inductance value required to meet a given THD specification reduces as the switching frequency increases.

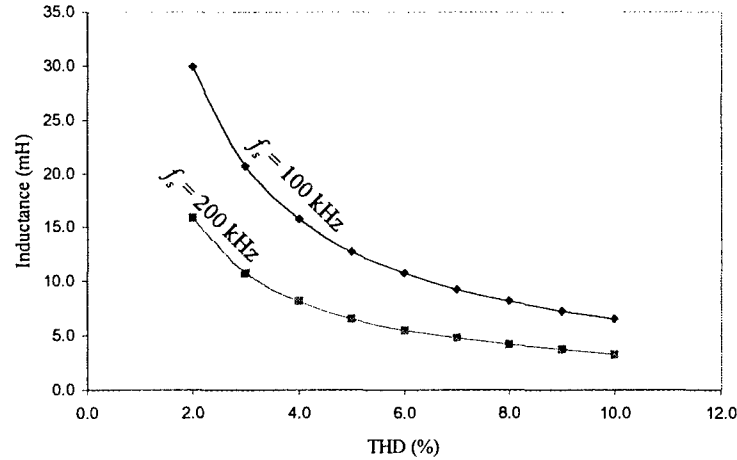


Figure 4.24. Inductance value vs THD of actuator current

The weight of the inductor as a function of the inductance value is plotted in Figure 4.25.

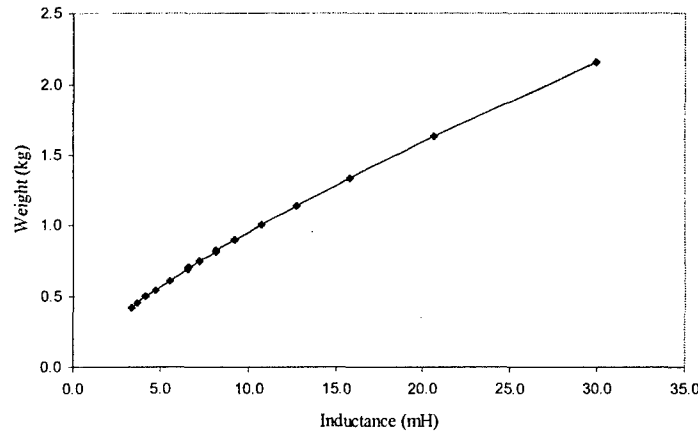


Figure 4.25. Weight of the inductor vs inductance value

The weight of an inductor is proportional to the energy stored, which in turn is proportional to inductance value and to the square of the peak inductor current. Since the peak current is approximately constant (determined by the maximum polarization), the weight of the inductance varies almost linearly with inductance.

4.3 Active damping using piezoelectric actuators

In this section, a control law to make the piezoelectric actuator actively damp the structure is proposed. It is illustrated that controlling the current through the actuator to be proportional to the acceleration of the structure naturally results in an increase in the damping of the mechanical system without a change to the stiffness of the structure. Specifically, it is shown analytically that controlling the current into the actuator to be proportional to the acceleration of the structure results in an increase in the damping of the mechanical structure without a change to the stiffness of the structure. The coupled electromechanical model of the actuator and the structure developed in Section 4.1 is

used in this section for the development of the control law and for the analysis of its implications on the design of the drive amplifier and the power flow characteristics between the actuator and the amplifier. The structure is assumed to be acted on by a sinusoidal external disturbance force. It is shown that, due to the active damping, the piezoelectric actuator absorbs mechanical power injected into the system by the external disturbance force and redirects it back to the electrical source. Hence, there is a net flow of electrical power from the actuator to the electrical source. In addition, due to the capacitive electrical characteristics of the actuators, there is a considerable amount of reactive power circulating between the actuator and the amplifier. A detailed analysis of the electromechanical power transfer characteristics is presented in this section. The anhyseretic nonlinearity in the actuator is, however, neglected in this analysis in order to exemplify the dependence of the power flow characteristics on the material properties of the actuator and the structure. Estimates of the peak current and voltage in the actuator are also determined. These peak values are used in the design of the drive amplifier.

4.3.1. Active damping of structure

In this section, a control law to add damping to the structure shown in Figure 4.1 is presented. Beginning with the electromechanical model in Figure 4.6, it is shown that the natural control law to increase damping in the structure is acceleration feedback to a current controlled amplifier. From Figure 4.6, the force F_a exerted by the actuator on the structure is given by:

$$\begin{aligned} f_a &= \frac{Y_{33}K_1K_2}{1-k^2}x - \frac{d_{33}}{\epsilon_{33}} \frac{1}{nlw} \frac{Y_{33}K_2}{1-k^2}q \\ &= K_a x - \frac{d_{33}}{\epsilon_{33}} \frac{1}{nlw} \frac{1}{K_1} K_a q, \end{aligned} \quad (4.44)$$

where K_a is the equivalent stiffness of the actuator and is given by:

$$K_a = \frac{Y_{33}K_1K_2}{(1-k^2)}. \quad (4.45)$$

Substituting Equation (4.44) into Equation (4.1) we obtain:

$$M\ddot{x} + B\dot{x} + Kx = f_{ext} - K_a x + \frac{d_{33}}{\epsilon_{33}} \frac{1}{nlw} \frac{1}{K_1} K_a q \quad (4.46)$$

or

$$M\ddot{x} + B\dot{x} + (K + K_a)x = f_{ext} + \frac{d_{33}}{\epsilon_{33}} \frac{1}{nlw} \frac{1}{K_1} K_a q.$$

So the addition of the actuator to the system increases the stiffness of the structure as expected.

Furthermore, Equation (4.46) also clearly shows how to introduce feedback from the structure to increase the damping. If the charge into the piezoelectric actuator is made a function of the velocity as:

$$q = -K_f \dot{x}, \quad (4.47)$$

then the closed loop equation becomes:

$$M\ddot{x} + \left(B + \frac{d_{33}}{\epsilon_{33}} \frac{1}{nlw} \frac{1}{K_1} K_a K_f \right) \dot{x} + (K + K_a) x = f_{ext}. \quad (4.48)$$

Differentiating Equation (4.47):

$$\dot{i}_a = \dot{q} = -K_f \ddot{x}, \quad (4.49)$$

which shows that the damping can also be increased by feeding back acceleration to current into the actuator. This configuration of the feedback law is attractive because current amplifiers are easier to construct than charge amplifiers. Also, the output signal of an accelerometer can be used without any integration. Of course, this control law will not work at zero frequency. That is, the control system will not act as a positioning system.

The block diagram of the complete system after introducing the acceleration feedback is shown in Figure 4.26. This block diagram assumes there is a current controlled amplifier with unity gain in the loop.

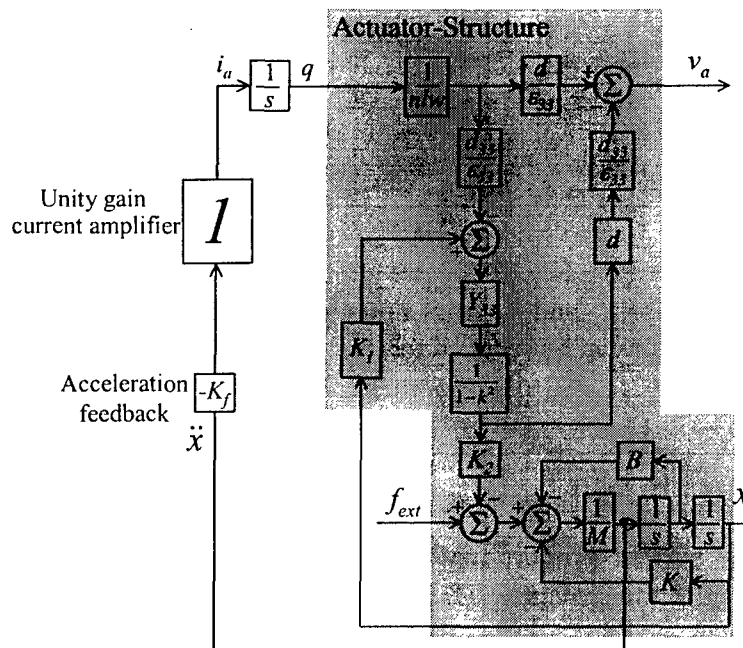


Figure 4.26. Block diagram of closed loop system

Rewriting Equation (4.48) in the standard form,

$$\ddot{x} + \left(B + \frac{d_{33}}{\epsilon_{33}} \frac{1}{nlw} \frac{1}{K_1} K_a K_f \right) \frac{1}{M} \dot{x} + \left(\frac{K + K_a}{M} \right) x = \frac{1}{M} f_{ext} \quad (4.50)$$

$$\ddot{x} + 2(\zeta + \zeta_a) \omega_n \dot{x} + \omega_n^2 x = \frac{1}{M} f_{ext},$$

where

$$\omega_n = \sqrt{\frac{K + K_a}{M}} \quad (4.51)$$

is the resonant frequency of the structure with the actuator,

$$\zeta = \frac{B/M}{2\omega_n} \quad (4.52)$$

is the damping of the uncontrolled structure and,

$$\zeta_a = \frac{\frac{d_{33}}{\epsilon_{33}} \frac{1}{nlw} \frac{1}{K_1} K_a K_f / M}{2\omega_n} \quad (4.53)$$

is the active damping added by the actuator.

Using Equation (4.45), the expression for the active damping ζ_a can be simplified as:

$$\zeta_a = \frac{\frac{d_{33}}{\epsilon_{33}} \frac{1}{nlw} \frac{1}{K_1} K_a K_f / M}{2\omega_n} = \frac{\frac{d_{33}}{\epsilon_{33}} \frac{1}{nlw} \frac{1}{K_1} \frac{Y_{33} K_1 K_2}{1 - k^2} K_f}{2\omega_n M} \quad (4.54)$$

Using the expressions for K_1 and K_2 from Equation (4.13), the active damping introduced by the controlled actuator can be reduced to:

$$\zeta_a = \frac{1}{nd_{33}} \frac{k^2}{1 - k^2} K_f \frac{1}{2\omega_n M} \quad (4.55)$$

Thus, making the current proportional to the acceleration of the structure introduces additional damping to the structure. The effects of actively damping the structure on the power flow between the external disturbance and the electrical input will be analyzed in the next section.

4.3.2. Amplifier Requirements

In the previous section, a control law to add damping to the structure was proposed. The primary electrical requirements of the amplifier needed to drive this system are determined in this section. First, the peak voltages and currents drawn by the actuator in closed loop are derived. These estimates are critical to the design of the amplifier. It is assumed that the structure is subjected to a sinusoidal disturbance force and the peak current and voltage are obtained from a frequency domain analysis. The damping of the uncontrolled structure ζ , is assumed to be zero. It can be shown the current and voltage in the actuator both reach their maximum amplitudes when the frequency of the external force is ω_n . The following analysis is, in this sense, worst case.

In the previous section, it was shown that the proposed control law required a current controlled amplifier. A schematic of such an amplifier driving the actuator is shown in Figure 4.27.

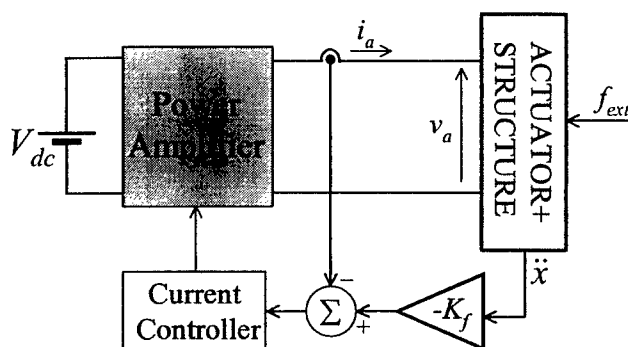


Figure 4.27. Schematic of amplifier driving the actuator

The amplifier is driven from a constant voltage source. It is forced by the current controller to synthesize the current to be driven into the actuator in response to the command from the acceleration feedback. Typical current i_a , and voltage v_a waveforms at the terminals of the actuator are shown in Figure 4.28 for a sinusoidal disturbance f_{ext} at the resonant frequency ω_n of the structure. Due to the capacitive nature of the actuator the current and voltage at the actuator terminals are oscillatory. In particular, the amplifier must be able to sink current.

The components of the amplifier must be capable of withstanding the peak values of current and voltage. The amplifier components should be sized according to the input DC voltage V_{dc} and the peak current required to be driven into the actuator under typical operating conditions.

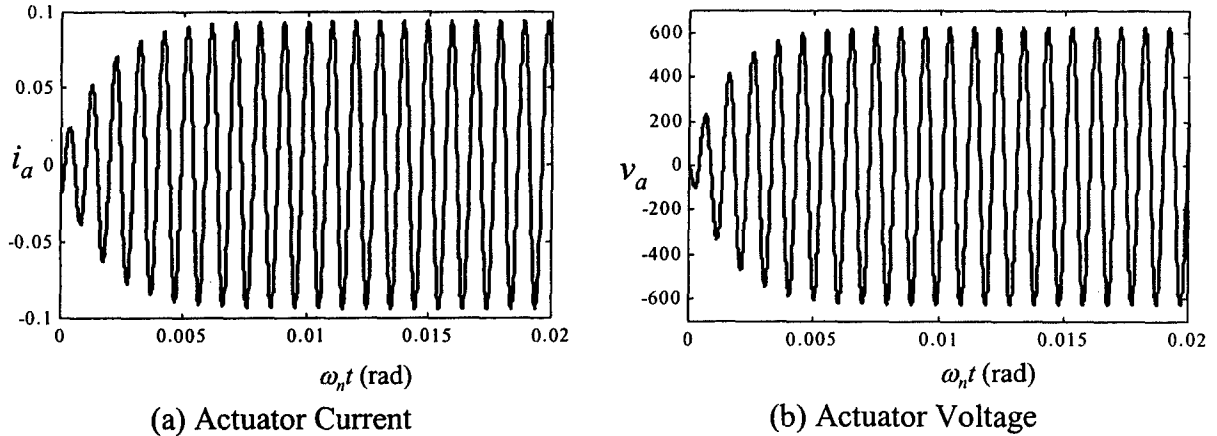


Figure 4.28. Instantaneous current and voltage at actuator terminals

To determine the peak current and voltage at the actuator terminals, a simplified representation of Figure 4.27 as shown in Figure 4.29 is used.

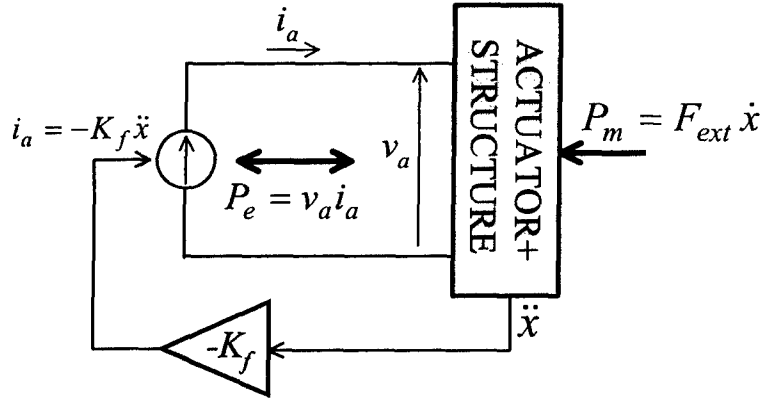


Figure 4.29. Simplified representation of the controlled actuator-structure

The power amplifier is made to appear as an ideal current source/sink to the actuator. Mechanical power is injected into the actuator/structure from the external disturbance and electrical power is injected from the amplifier.

In the following analysis the peak current and voltage into the terminals of the actuator will be determined. The basic idea is to inject a sinusoidal disturbance force into the system, and then determine the voltage and current at the terminals of the actuator as a function of this sinusoidal disturbance force. Sinusoidal steady state analysis is used and the analysis is based on the block diagram in Figure 4.26. From Equation (4.50), the displacement $X(s)$ of the structure can be obtained as:

$$X(s) = \frac{1}{s^2 + 2(\zeta + \zeta_a)\omega_n s + \omega_n^2} \frac{F_{ext}(s)}{M}. \quad (4.56)$$

The current is directly proportional to the acceleration of the structure due to the feedback introduced and is given by:

$$I_a(s) = -s^2 K_f X(s) = \frac{-s^2 K_f}{s^2 + 2(\zeta + \zeta_a)\omega_n s + \omega_n^2} \frac{F_{ext}(s)}{M}. \quad (4.57)$$

It can be seen that the current amplitude reaches its maximum value when the structure is excited at its resonant frequency. This maximum amplitude can be obtained from Equation (4.57) and is:

$$I_{a, \max} = \left| I_a(j\omega) \right|_{\substack{\omega=\omega_n \\ \zeta=0}} = \frac{\omega_n}{\left(\frac{k^2}{1-k^2} \frac{1}{nd_{33}} \right)} \left| F_{ext}(j\omega) \right|. \quad (4.58)$$

The denominator in Equation (4.58) is determined by the material parameters of the actuator. It can be observed, that as the coupling coefficient decreases, the peak current increases. As d_{33} increases, the maximum current increases. Finally, as the number of layers increases, the maximum current increases because the actuator gets bigger.

Through a similar analysis, the maximum voltage across the actuator terminals can be determined. The voltage v_a at the terminals of the actuator is the resultant of the capacitive effect of the actuator and the contribution from the mechanical strain. With reference to Figure 4.26, the voltage is given by:

$$\begin{aligned} V_a(s) &= \frac{1}{\epsilon_{33}} \frac{d}{nlw} \frac{I_a(s)}{s} - \frac{d_{33}}{\epsilon_{33}} d \left(\frac{Y_{33}}{1-k^2} \right) \left(K_1 X(s) - \frac{d_{33}}{\epsilon_{33}} \frac{1}{nlw} \frac{I_a(s)}{s} \right) \\ &= \frac{1}{1-k^2} \frac{1}{C} \frac{1}{s} \frac{I_a(s)}{s} - \frac{d_{33}}{\epsilon_{33}} \frac{d}{K_2} K_a X(s). \end{aligned} \quad (4.59)$$

Substituting for $X(s)$ from Equation (4.56) and for $I_a(s)$ from Equation (4.57), the expression for the voltage $V_a(s)$ in terms of the external disturbance F_{ext} is obtained as follows:

$$\begin{aligned} V_a(s) &= \frac{1}{C_{blk}} \frac{I_a(s)}{s} - \frac{d_{33}}{\epsilon_{33}} \frac{d}{K_2} K_a X(s) = - \left(\frac{sK_f}{C_{blk}} + \frac{d_{33}}{\epsilon_{33}} \frac{d}{K_2} K_a \right) X(s) \\ &= \frac{-1}{s^2 + 2(\zeta + \zeta_a)\omega_n s + \omega_n^2} \left(\frac{sK_f}{C_{blk}} + \frac{d_{33}}{\epsilon_{33}} \frac{d}{K_2} K_a \right) \frac{F_{ext}(s)}{M}, \end{aligned} \quad (4.60)$$

where

$$C_{blk} = \varepsilon_{33} \left(\frac{nlw}{d} \right) (1 - k^2) \quad (4.61)$$

is the equivalent blocked capacitance of the actuator.

Similar to the actuator current, the voltage reaches its maximum amplitude at ω_n . This maximum amplitude determined from Equation (4.60) is given by Equation (4.62):

$$V_{a,max} = |V_a(j\omega)|_{\omega=\omega_n, \zeta=0} = \sqrt{\frac{1}{K_f^2 \omega_n^2} + \frac{1}{\frac{1}{nd_{33}} \frac{k^2}{1-k^2} C_{blk}}} |F_{ext}(j\omega)|. \quad (4.62)$$

Using the expression for the maximum current into the actuator, Equation (4.62) can be further simplified as:

$$V_{a,max} = |V_a(j\omega)|_{\omega=\omega_n, \zeta=0} = \sqrt{\frac{|F_{ext}(j\omega)|^2}{K_f^2 \omega_n^2} + \frac{I_{a,max}^2}{\omega_n^2 C_{blk}^2}}. \quad (4.63)$$

It can be seen from Equation (4.63) that the maximum voltage is determined as a sum of the capacitive voltage drop and a component contributed by the feedback constant and the external disturbance force.

Due to constraints imposed by material properties, there is a specified maximum allowable voltage across the actuator and the value determined from Equation (4.62) should not exceed this maximum allowable voltage. The amplifier components need to be designed such that this maximum amplitude can be safely supplied to the actuator. Finally, the relationship between the maximum voltage delivered to the actuator and the value of the DC bus voltage V_g supplying the amplifier in Figure 4.27 will affect the topology of the amplifier.

4.3.3. Power Flow Analysis

A detailed analysis of the electromechanical power transfer between the amplifier and actuator structure is presented in this section. Sinusoidal steady state analysis is used as in the previous section using Figure 4.26 to obtain expressions for the real and reactive components of the mechanical power from the external disturbance force and the electrical power from the constant current source. The dependence of the power flow characteristics on the material properties and active damping introduced is described. It is assumed that $\zeta=0$, as in the previous section. It can be easily verified that the average mechanical and electrical powers reach their maximum values when the frequency of the sinusoidal excitation is ω_n . Furthermore, their magnitudes decrease as the amount of the active damping introduced by the control system increases.

Using the expressions for the actuator current and voltage from Equations (4.45) and (4.48), the actuator impedance can be obtained as:

$$Z_a(j\omega) = \frac{V_a(j\omega)}{I_a(j\omega)} = \frac{1}{j\omega C_{blk}} - \frac{1}{\omega^2} \frac{d_{33}}{\epsilon_{33}} \frac{d}{K_2} \frac{K_a}{K_f}. \quad (4.64)$$

It can be seen that the electrical impedance of the actuator consists of a reactive part due to the capacitive nature of the actuator and a negative resistive part. The negative resistive part is a manifestation of the active damping introduced to the acceleration feedback. The effect of this negative real part will be explained in the following analysis of power flow. The apparent electrical power is given by:

$$\begin{aligned} P_e(j\omega) &= V_a(j\omega) I_a^*(j\omega) = Z_a(j\omega) I_a(j\omega) I_a^*(j\omega) = |I_a(j\omega)|^2 Z_a(j\omega) \\ &= \frac{(K_f^2 \omega^4)}{(\omega_n^2 - \omega^2)^2 + 4(\zeta + \zeta_a)^2 \omega^2 \omega_n^2} \left| \frac{F_{ext}(j\omega)}{M} \right|^2 \left(\frac{1}{j\omega C_{blk}} - \frac{1}{\omega^2} \frac{d_{33}}{\epsilon_{33}} \frac{d}{K_2} \frac{K_a}{K_f} \right). \end{aligned} \quad (4.65)$$

To calculate the mechanical power into the system, the velocity of the structure is required. From Equation (4.44), the velocity can be obtained as:

$$\dot{X}(s) = \frac{s}{s^2 + 2(\zeta + \zeta_a)\omega_n s + \omega_n^2} \frac{F_{ext}(s)}{M}. \quad (6.23)$$

Now the apparent mechanical power is given by:

$$P_m(j\omega) = F_{ext}(j\omega) (-j\omega X^*(j\omega)) = \frac{-j\omega}{(\omega_n^2 - \omega^2) - 2j(\zeta + \zeta_a)\omega\omega_n} \frac{|F_{ext}(j\omega)|^2}{M}. \quad (6.24)$$

These power quantities are complex, indicating that there is a real net power flow through the system and a circulating reactive power component between the amplifier and the actuator/structure. To illustrate this point, the instantaneous and average mechanical power fed into the structure by a sinusoidal disturbance force with an amplitude of 1000N is shown in Figure 4.30.

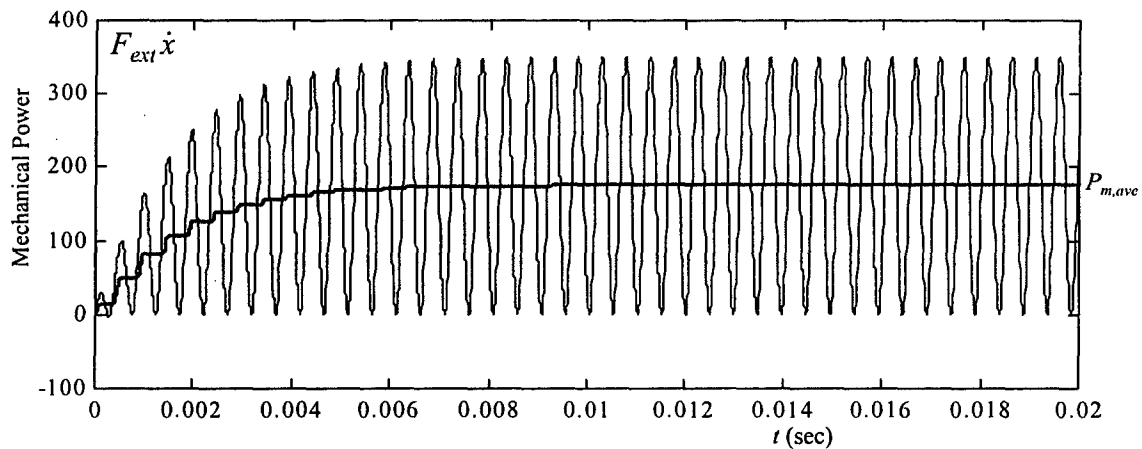


Figure 4.30. Instantaneous and average mechanical power from external disturbance

In steady state, average mechanical power is being injected into the system as shown by Figure 4.30 as long as the system is actively damped ($\zeta_a > 0$).

The corresponding instantaneous and average electrical powers at the terminals of the actuator are shown in Figure 4.31. These graphs show that there is a large oscillating power flow compared to the real power flow. This characteristic is typical of piezoelectric actuators, and must be accounted for in the design of the amplifier. Second, these graphs show a net real power flow from the actuator/structure to the amplifier. This net power flow accounts for the damping introduced by the control loop.

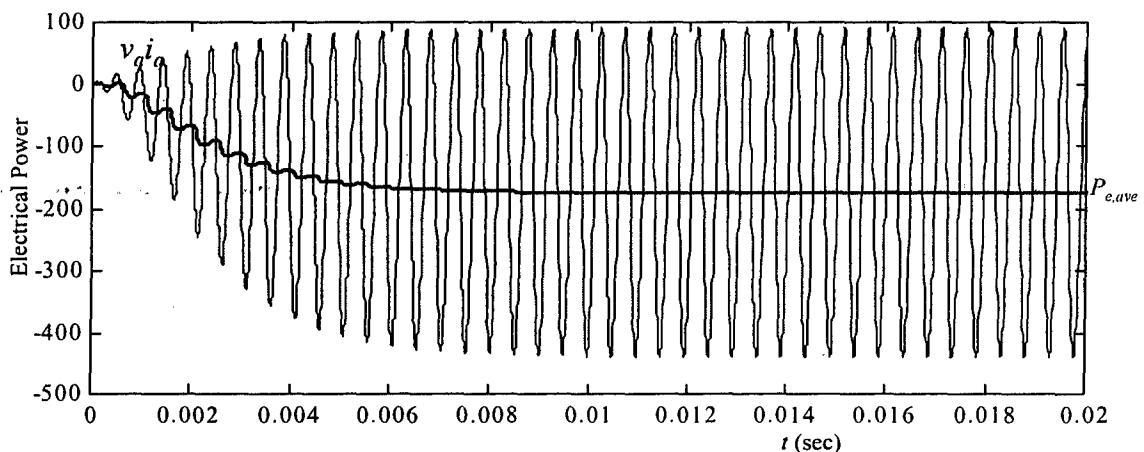


Figure 4.31. Instantaneous and average electrical power at actuator terminals

The average power is obtained by taking the real part of the apparent power. The average electrical power is:

$$\begin{aligned}
P_{e,ave}(\omega) &= \text{Re}[V_a(j\omega)I_a^*(j\omega)] = |I_a(j\omega)|^2 \text{Re}[Z_a(j\omega)] \quad (4.68) \\
&= \frac{1}{(\omega_n^2 - \omega^2)^2 + 4(\zeta + \zeta_a)^2 \omega^2 \omega_n^2} \left(-\frac{d_{33}}{\varepsilon_{33}} \frac{d}{K_2} K_a K_f \omega^2 \right) \left| \frac{F_{ext}(j\omega)}{M} \right|^2 \\
&= \frac{1}{(\omega_n^2 - \omega^2)^2 + 4(\zeta + \zeta_a)^2 \omega^2 \omega_n^2} \left(-\frac{d_{33}}{\varepsilon_{33}} \frac{1}{nlw} \frac{1}{K_1} K_a K_f \omega^2 \right) \left| \frac{F_{ext}(j\omega)}{M} \right|^2 \\
&= \frac{-2\zeta_a \omega_n \omega^2}{(\omega_n^2 - \omega^2)^2 + 4(\zeta + \zeta_a)^2 \omega^2 \omega_n^2} \frac{|F_{ext}(j\omega)|^2}{M},
\end{aligned}$$

where Equation (4.51) has been used. The average mechanical power is given by:

$$\begin{aligned}
P_{m,ave}(\omega) &= \text{Re}[F_{ext}(j\omega)(-j\omega X^*(j\omega))] = \frac{2(\zeta + \zeta_a)\omega_n \omega^2}{(\omega_n^2 - \omega^2)^2 + 4(\zeta + \zeta_a)^2 \omega^2 \omega_n^2} \frac{|F_{ext}(j\omega)|^2}{M} \quad (4.69) \\
&= \frac{2\zeta \omega_n \omega^2}{(\omega_n^2 - \omega^2)^2 + 4(\zeta + \zeta_a)^2 \omega^2 \omega_n^2} \frac{|F_{ext}(j\omega)|^2}{M} \\
&\quad + \frac{2\zeta_a \omega_n \omega^2}{(\omega_n^2 - \omega^2)^2 + 4(\zeta + \zeta_a)^2 \omega^2 \omega_n^2} \frac{|F_{ext}(j\omega)|^2}{M}.
\end{aligned}$$

It can also be seen from Equations (4.68) and (4.69) that the average electrical power at the actuator terminals is the portion of the total average input power from the external disturbance that is consumed by the active damping ζ_a introduced by the controlled actuator. The rest of the mechanical power is dissipated in the damping of the structure. This observation is supported by Figures 4.30 and 4.31 ($\zeta=0$). This means that there is an average flow of power from the actuator-structure to the electrical source. This result is similar to the result obtained in [21] which shows that active damping manifests itself in enabling the actuator absorb the injected mechanical energy and funnel it to the electrical source. The ideal current amplifier in this model absorbs this electrical power.

It can be seen from Equation (4.55) that the acceleration feedback constant K_f depends on the active damping ratio ζ_a , the electromechanical coupling coefficient k^2 and the physical dimensions of the actuator according to:

$$K_f = 2\zeta_a \omega_n M \left(nd_{33} \frac{1-k^2}{k^2} \right). \quad (4.70)$$

Since the active damping ratio is related to the real power flow, it is not surprising that the real power flow depends on the acceleration feedback constant. Figure 4.32 shows the real electrical power as a function of frequency for a range of values of K_f . The damping ζ of the uncontrolled structure is assumed to be zero in Figure 4.32.

It can be seen that the real electrical power reaches its maximum value at the resonant frequency ω_n for all values of K_f as mentioned above. As K_f and hence ζ_a decreases, the profile of the real power becomes more concentrated around ω_n approaching an impulse for $K_f = \zeta_a = 0$.

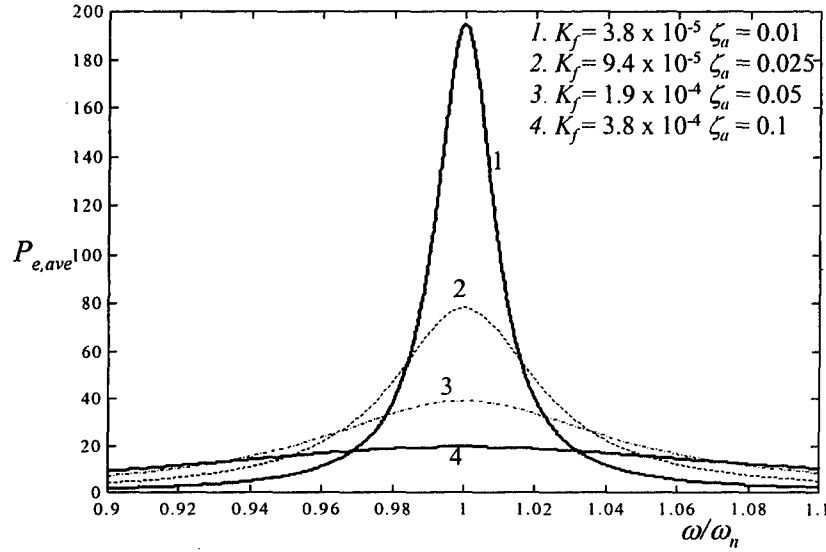


Figure 4.32. Variation of real power with acceleration feedback constant

It is not surprising that the feedback gain affects the real power flow primarily in the frequency band around the natural frequency, because that is where the control action is concentrated. From Equations (4.68) and (4.46), the maximum value of the real electrical power for a given value of K_f can be expressed as:

$$\max_{\omega, \zeta} [P_{e,ave}(\omega)] = P_{e,ave}(\omega) \Big|_{\omega=\omega_n, \zeta=0} = \frac{-1}{2\zeta_a \omega_n} \frac{|F_{ext}(j\omega)|^2}{M} = -\frac{I_{\max} |F_{ext}|}{K_f} \quad (4.71)$$

Hence, the maximum real electrical power decreases with increase in the feedback constant and hence the active damping introduced as seen in Figure 4.32.

The electromechanical coupling coefficient of the actuator affects the active damping and the resonant frequency of the structure as can be seen from Equations (4.45), (4.50) and (4.54). The effect of the coupling coefficient on the feedback constant for varying values of active damping can also be determined from Equation (4.70). It can be seen that the acceleration feedback constant K_f required to achieve a given value of active damping ratio ζ_a decreases as the coupling coefficient increases.

Hence, for the given external excitation the average power that the electrical source is required to absorb so as to achieve a reference active damping ratio decreases as the coupling coefficient decreases. This is illustrated in Figure 4.33, which shows the average electrical power absorbed by the current amplifier at the resonant frequency of the structure. The negative values of average power in Figure 4.33 indicate that the power is flowing back through the current amplifier back to the electrical source. It can be seen that as the coupling coefficient increases, there is a decrease in the real power flow back into the amplifier.

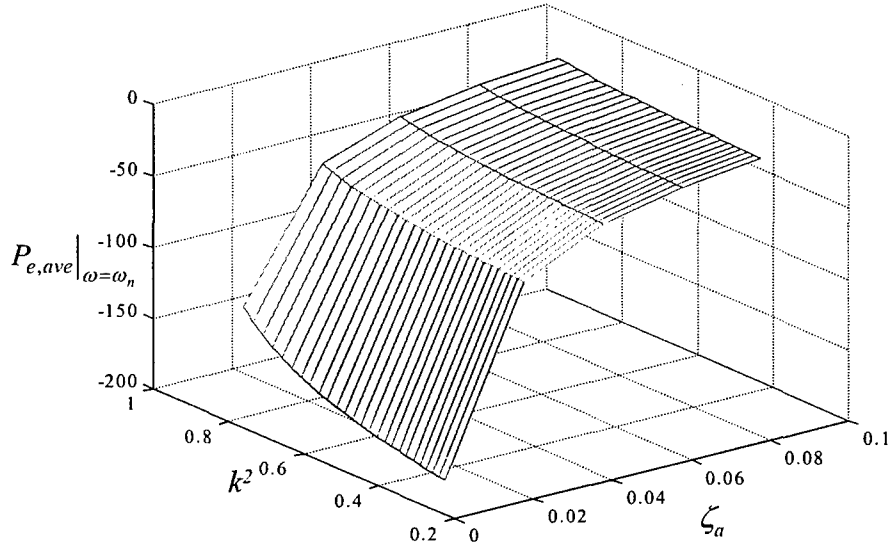


Figure 4.33. Average electrical power at the resonant frequency as a function of k^2 and ζ_a

The complex part of the apparent power implies that there is a considerable amount of reactive power circulates between the actuator and the electrical source. This circulating power can be observed from Figure 4.31. This reactive power results in the current and voltage at the actuator terminals to be oscillatory as shown in Figure 4.27. Since these oscillating currents and voltages are considerably larger than the real power flow, it is necessary to design the amplifier to account for these components. The reactive component of the electrical power is given by:

$$\begin{aligned}
 P_{e, \text{reac}}(\omega) &= \text{Im}[V(j\omega)I^*(j\omega)] = |I_a(j\omega)|^2 \text{Im}[Z_a(j\omega)] = -\frac{|I_a(j\omega)|^2}{\omega C_{blk}} \\
 &= \left[\frac{-\omega^3 K_f^2 / C_{blk}}{(\omega_n^2 - \omega^2)^2 + 4(\zeta + \zeta_a)^2 \omega^2 \omega_n^2} \right] \left| \frac{F_{\text{ext}}(j\omega)}{M} \right|^2.
 \end{aligned} \tag{4.72}$$

The reactive components of the mechanical power is given by:

$$P_{m, \text{reac}}(\omega) = \text{Im} \left[F_{\text{ext}}(j\omega) (-j\omega X^*(j\omega)) \right] \quad (4.73)$$

$$= \left[\frac{-\omega(\omega_n^2 - \omega^2)}{(\omega_n^2 - \omega^2)^2 + 4(\zeta + \zeta_a)^2 \omega^2 \omega_n^2} \right] \frac{|F_{\text{ext}}(j\omega)|^2}{M}.$$

It can be seen from Equation (4.73) that when the disturbance frequency is the same as the resonant frequency ω_n , the reactive component in the mechanical power, as expected, becomes zero. The reactive component of the electrical power, however, reaches its maximum at the resonant frequency according to Equation (4.71). Using the expression for the maximum actuator current given by Equation (4.46) the peak reactive power can be obtained as:

$$P_{e, \text{reac}}(j\omega) \Big|_{\zeta=0, \omega=\omega_n} = -\frac{I_{\text{max}}^2}{\omega_n C_{\text{blk}}} = \frac{-\omega_n / C_{\text{blk}}}{\left(\frac{1}{d_{33}} \frac{k^2}{1-k^2} \right)^2} |F_{\text{ext}}(j\omega)|^2. \quad (4.74)$$

The peak reactive power is independent of the active damping introduced and is determined by the material constants of the actuator. Figure 4.34 shows the reactive electrical power as a function of the real electrical power over a frequency range $0.1\omega_n$ to $10\omega_n$ for different values of K_f . It can be seen that the peak values of the real and reactive powers increase with decreasing ζ_a as can be expected from Equations (4.68) and (4.69). The amplifier must be designed such that it can handle the real power and capacitive reactive power under worst case operating conditions. Worst case occurs when the actuator is driven at the mechanical resonant frequency where the real and reactive power at the actuator terminals reach their peak operating values.

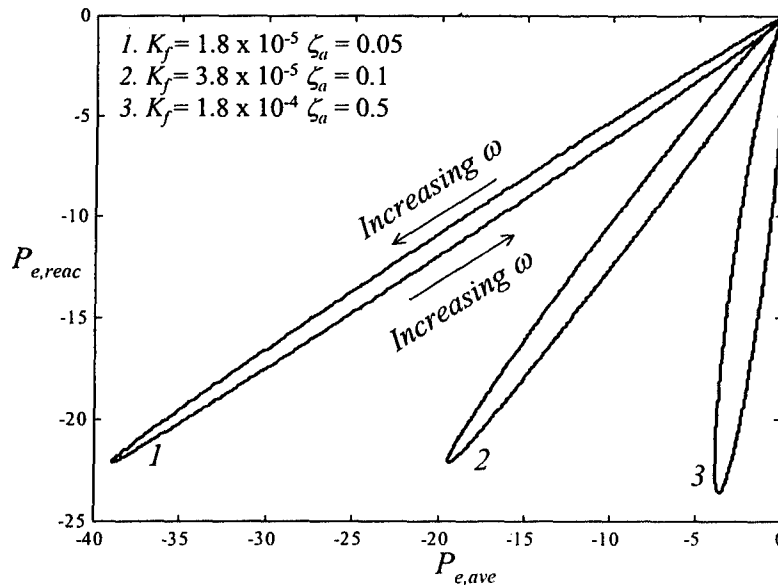


Figure 4.34. Reactive power vs. real power for different ζ_a

Figure 4.35 shows the reactive power at the actuator terminals at the resonant frequency as a function of ζ_a and the coupling coefficient k^2 . As expected from Equation (4.73), the reactive power does not vary with the damping ratio but decreases with increasing k^2 since a higher value of the coupling coefficient results in a greater energy conversion efficiency.

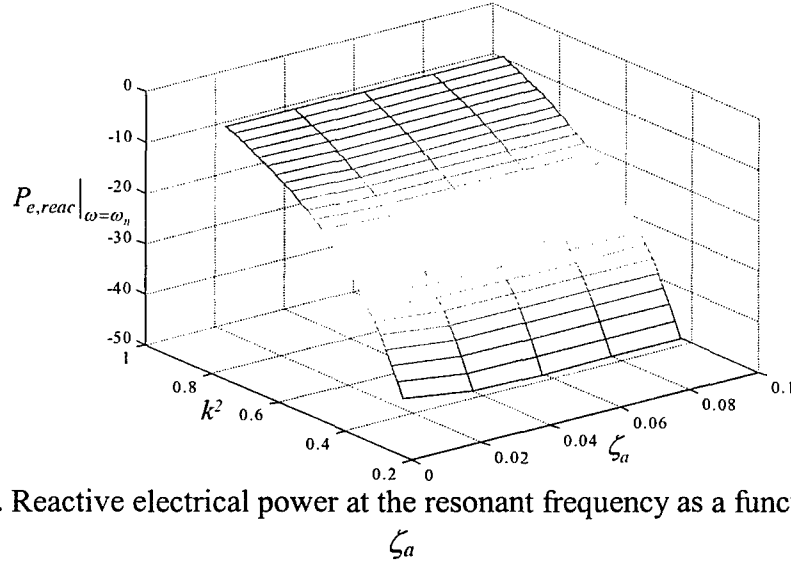


Figure 4.35. Reactive electrical power at the resonant frequency as a function of k^2 and ζ_a

5. Bifurcation Analysis and Optimization

5.1 Multivariable Impedance Ratio Criterion

The baseline power distribution system shown in Figure 2.1 consists of several complex systems that interact with each other. One of critical operational requirements is the stability and robustness of the power distribution system. Hence, in addition to ensuring the stability of individual subsystems, it is necessary to guarantee minimal interaction between interconnected subsystems and avoid unstable operation due to the integration of subsystems. This section is devoted to the study of techniques to analyze the stability and interaction between interconnected subsystems.

In the optimization formulations presented in Section 3, the classical Middlebrook impedance ratio criterion was used to ensure stability of interconnected subsystems by requiring that the terminal impedances of the individual subsystems at the interconnection be sufficiently separated. However, the impedance ratio criterion is applicable only to a SISO case and hence cannot be directly applied to study interaction in three phase systems because of their multivariable nature. In this chapter, the impedance ratio criterion is extended to a multivariable setting to make it applicable to three phase and single-phase AC interfaces. A multivariable impedance ratio criterion, defined in terms of the singular values of the terminal impedance matrices at the interconnection is proposed.

Studies of input filter interaction in three phase rectifiers were performed in [22,23], but the results presented therein were not applied to three phase AC-DC converters in general. The design of input filters for power factor correction circuits was introduced in [24]. The factors affecting the choice of the filter topology for power factor correction circuits were outlined. In [25], the three-phase converter was treated as a multivariable system and criteria for the stability of the interconnected filter-converter system were derived based on the eigenvalue loci and singular values of the relevant transfer function matrices. However, the analysis presented in [25] did not clearly identify the effects of the inclusion of the input filter on the performance indices of the system. The analysis presented here is general but is described using the example of a three-phase boost rectifier represented by its average model in rotating dq coordinates [27].

The organization of this section is as follows: The Middlebrook Impedance Ratio criterion is described in section 5.1.1. In section 5.1.2, the basic control objectives of a generic PFC converter are presented. A filter topology suitable for PFC converters as proposed in [24] is chosen as an example for the analysis. The effects of the filter components on the existence and variation of the operating conditions of the converter are detailed. In section 5.1.3, a three-phase boost rectifier with a conventional two-channel controller is used as an example to study the effect of the input filter on the performance and stability of the rectifier system. Expressions for the loop gain, output impedance and audio-susceptibility are derived. Section 5.1.4 introduces the dq -model of a balanced three phase input filter. The effect of the input filter on the performance indices of the rectifier identified in section 5.1.3 is determined. The traditional minor loop gain, "Ratio of the output impedance of the filter to the input impedance of the converter" is introduced. A multivariable criterion for the stability of the interconnected system is derived. The stability criterion is then reduced to a sufficient condition based on the singular values of the impedance matrices in section 5.1.5. Simplifying approximations that enable the system designer to draw on physical insights to relate to the singular values are then made. Simulation results are shown to illustrate the results derived from the analysis.

5.1.1. Middlebrook Impedance Ratio Criterion

A generic subsystem interface formed by connecting two electrical subsystems in the aircraft power distribution system is shown in Figure 5.1. Each subsystem is represented by a standard two-port model as shown in Figure 5.1.

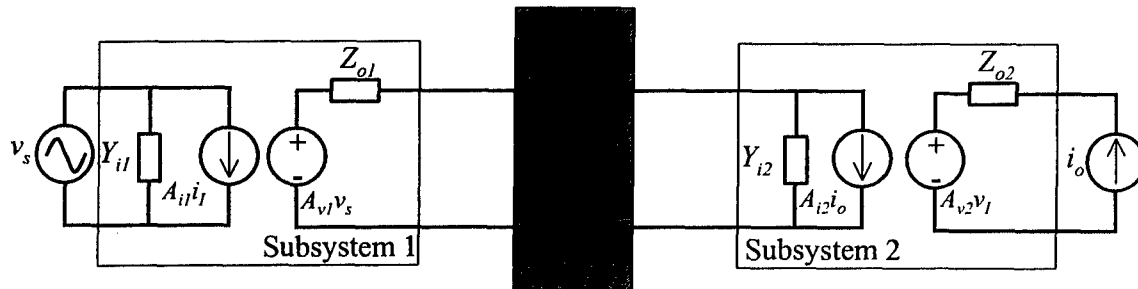


Figure 5.1. Generic Subsystem Interface

The current i_I , and voltage v_I , at the interface are given by:

$$\begin{aligned} i_I &= A_{i2}i_o + Y_{i2}v_I, \\ v_I &= A_{v1}v_s - Z_{o1}i_I. \end{aligned} \quad (5.1)$$

From Equation (5.1), it can be seen that the interconnection results in a feedback loop as shown in Figure 5.2.

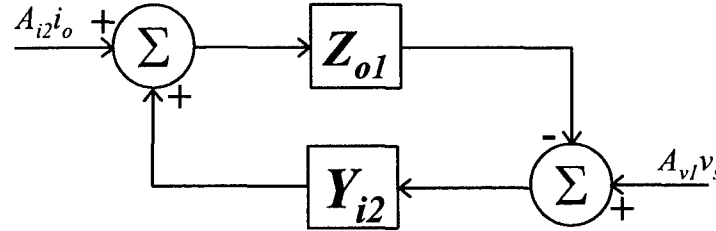


Figure 5.2. Feedback loop at the interface due to interconnection of subsystems 1 and 2

The stability of the interconnected system depends on the stability of the feedback loop. The sufficient condition for the stability of the feedback loop and hence of the interconnected system is given by the small gain theorem. According to the small gain theorem, the feedback loop is stable if the loop gain is less than unity as given below:

$$\|Z_{o1}(j\omega)\| \cdot \|Y_{i2}(j\omega)\| \ll 1. \quad (5.2)$$

This expression can be rewritten as:

$$\|Z_{o1}(j\omega)\| \ll \frac{1}{\|Y_{i2}(j\omega)\|} = \|Z_{i2}(j\omega)\|. \quad (5.3)$$

This simple expression says that the magnitude of the output impedance of subsystem 1 (filter) must everywhere be less than the input impedance of subsystem 2 (converter). Equation (5.3) is traditionally known as the Impedance Ratio Criterion.

5.1.2. Input Filter Interaction in Three-Phase AC-DC Converters

AC-DC converters both three phase and single phase, are basically posed with two control objectives: (1) tight regulation of output DC voltage and (2) regulation of input power factor to unity. The power drawn by the converter from the AC source is, hence, purely real and is equal to the power required by the load on the DC side. The schematic of a three-phase AC-DC converter supplied from an AC source through an input filter is shown in Figure 5.3. v_b and v_c , not shown in Figure 5.3, represent the voltages of phase b and c at the converter input.

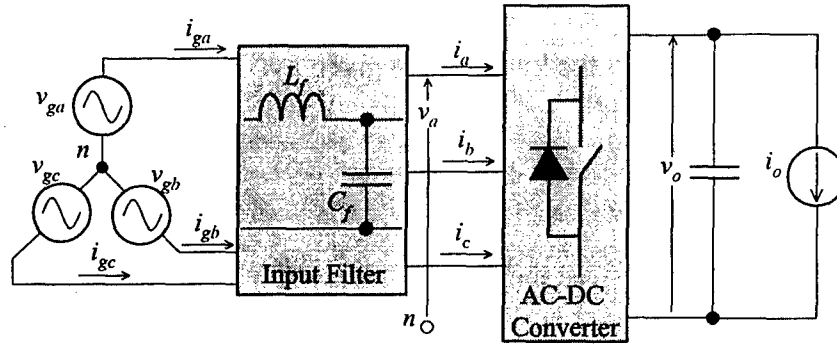


Figure 5.3. Schematic of three-phase AC-DC Converter with input filter

In the absence of an input filter, the voltage $v_{ga} = v_a$ and the current $i_{ga} = i_a$. With the power factor regulated to unity, the current i_{ga} and the voltage v_{ga} are in phase. The phasor diagram showing the voltages and currents at sinusoidal steady state are shown in Figure 5.4a. With the inclusion of the input filter, if the input current is required to be in phase with the voltage, as in Figure 5.4b, the converter must be forced to draw a current that is not in phase with the voltage at its input.

Thus, some reactive power has to be circulated between the converter and the input filter to achieve unity power factor at the source. Figure 5.5 shows a block diagram of a three-phase rectifier fed from an AC source through an input filter.

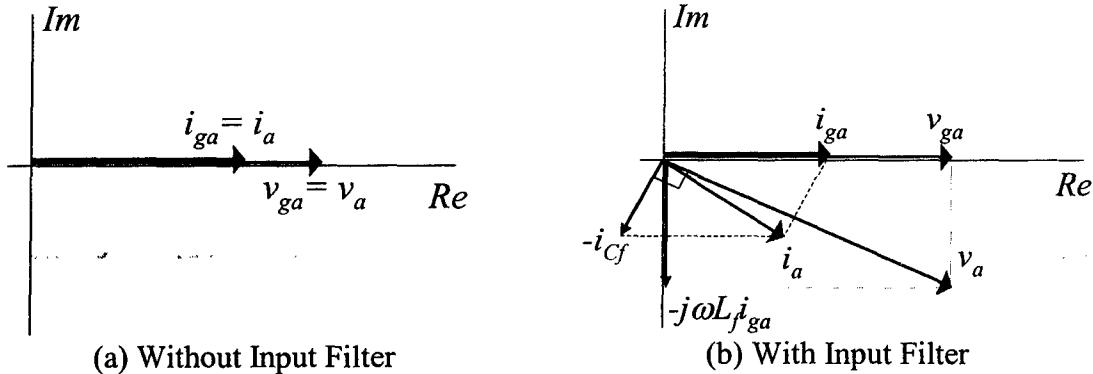


Figure 5.4. Phasor Diagram of phase current and voltage with and without input filter

The rectifier, input filter and the AC source are represented by their corresponding dq models.

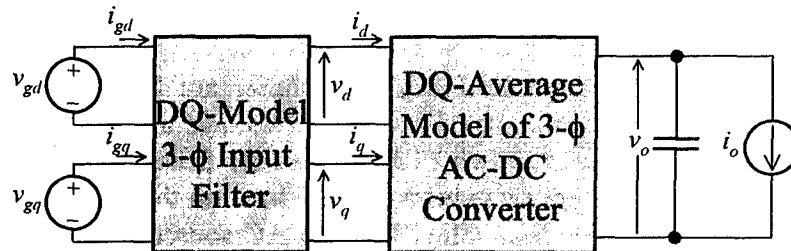


Figure 5.5 DQ-Model of a three-phase rectifier fed from an AC source

The real and reactive powers supplied by the source are given by:

$$P = \left(\frac{1}{2} \right) (v_{gd} i_{gd} + v_{gq} i_{gq}) \quad (5.4)$$

$$Q = \left(\frac{1}{2} \right) (v_{gq} i_{gd} - v_{gd} i_{gq}).$$

Regulating the power factor to unity at the input requires driving the reactive power Q to zero. This results in the following relationship between the input voltages and currents:

$$\frac{v_{gd}}{i_{gd}} = \frac{v_{gq}}{i_{gq}}. \quad (5.5)$$

If the d-axis is synchronized with the zero crossing of the phase α voltage, then $v_{gq}=0$ thus resulting in $i_{gq}=0$ for zero reactive power. The rectifier is usually controlled by a two-channel compensator, one channel for output voltage regulation and the other for regulating i_q to I_{qref} to achieve unity power factor. In the absence of an input filter, $v_{gd,q}=v_{d,q}$ and $i_{gd,q}=i_{d,q}$. Hence, regulating i_q to 0 will ensure unity power factor at the input.

However, as mentioned before, with the inclusion of the input filter, it is necessary to circulate some reactive power between the filter and the converter to achieve unity power factor at the input. This translates to regulating i_q to a value different from zero, dependent on the magnitude of the real power supplied to the load, the input voltage and the component values of the input filter. However, the circulating reactive power between the converter and the input filter may result in larger currents to flow through the switches of the converter if the filter components are not appropriately sized. In addition, the inclusion of the input filter appreciably changes the operating point of the rectifier.

Existence and Stability of Equilibrium Solutions

The input filter schematic shown in Figure 5.6 is used as an example for the interaction analysis to be presented in the following. This topology was chosen according to the directions presented in [24] for PFC circuits.

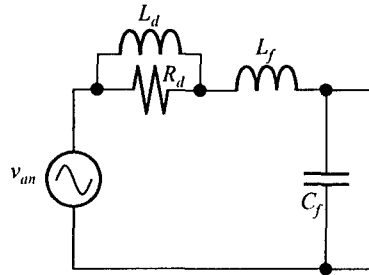


Figure 5.5. Schematic of input filter used in the analysis

Since the dc output voltage of the rectifier is tightly regulated, for a given load, the real power supplied by the rectifier and hence, drawn at the output of the filter (assuming a lossless converter) is constant. If i_q is regulated such that $i_{gq}=0$, the real power P is then given by the equation:

$$P = \frac{1}{2} \left(V_{gd} I_{gd} - I_{gd}^2 R_d \frac{(\omega/\omega_d)^2}{1 + (\omega/\omega_d)^2} \right), \quad (5.6)$$

$$\text{where } \omega_d = \frac{R_d}{L_d}.$$

From Equation (5.6), it can be seen that real equilibrium solutions exist for the interconnected system if and only if the following condition is satisfied:

$$\frac{V_{gd}^2}{8R_d} > P \frac{(\omega/\omega_d)^2}{1 + (\omega/\omega_d)^2}. \quad (5.7)$$

Uppercase letters in Equations (5.6) and (5.7) represent the operating point values of the corresponding variables. The operating point values for the input voltages and currents of the converter are given in Equation (5.8):

$$\begin{aligned} V_d &= V_{gd} - I_{gd} R_d \frac{(\omega/\omega_d)^2}{1 + (\omega/\omega_d)^2}, \\ V_q &= -\omega L_f I_{gd} - I_{gd} R_d \frac{(\omega/\omega_d)}{1 + (\omega/\omega_d)^2}, \\ I_d &= I_{gd} + \omega C_f V_q, I_q = -\omega C_f V_d. \end{aligned} \quad (5.8)$$

Figures 5.7 and 5.8 show the effects of changing R_d and C_f on the q-axis input current I_q to the rectifier, power dissipated in the filter, reactive power and the input current drawn by the rectifier. The control design for the rectifier is usually done at a single operating point given by $V_d=V_{gd}$, $V_q=V_{gq}=0$, $I_d=2P/V_d$, $I_q=0$. The filter components must hence be chosen such that the variation in the operating point after the inclusion of the input filter is not appreciable.

It is obvious from Equation (5.8) that C_f does not affect the power loss in the resistor. Increasing R_d reduces the power loss in the filter, at the cost of reduction in damping. To achieve the same damping ratios with a higher R_d requires a higher L_d and hence a bigger filter.

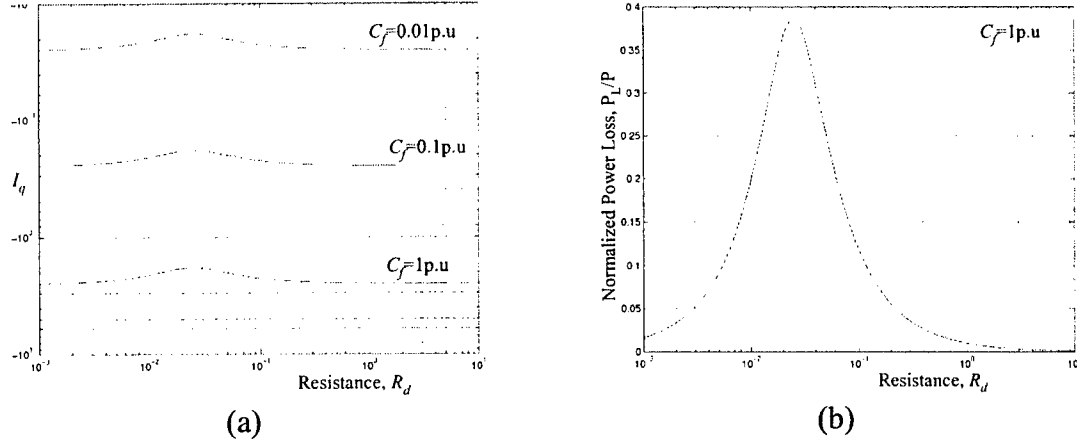


Figure 5.6. (a) Variation of I_q as a function of R_d for different values of C_f .
(b) Variation of power loss in filter as a function of R_d .

The variation of the resonant frequency, bandwidth and the damping ratios of the filter as a function of the component values are well known and hence, are not included here. A comparison of different filter topologies for PFC circuits is presented in [24].

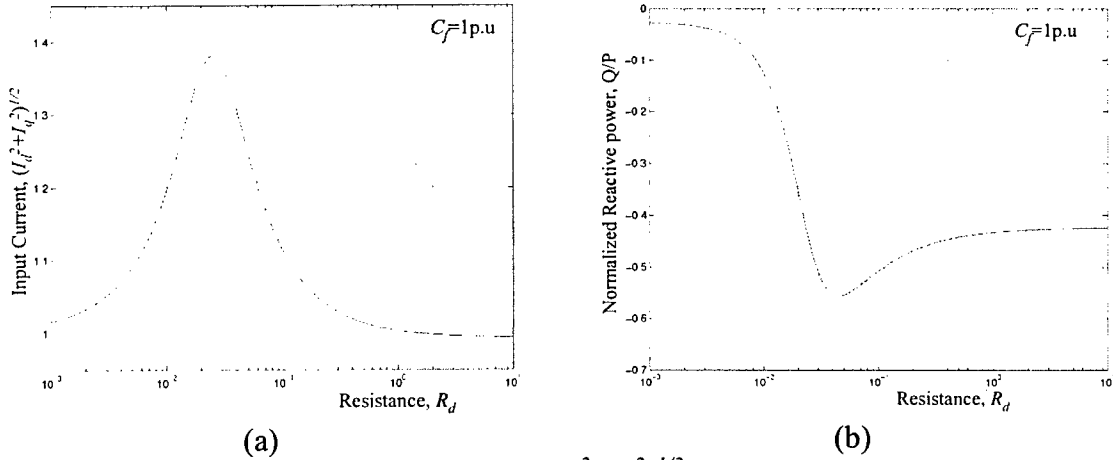


Figure 5.7. (a) Variation of $(I_d^2 + I_q^2)^{1/2}$ as a function of R_d .
(b) Variation of reactive power as a function of R_d .

5.1.3. Three Phase Boost Rectifier

The three-phase boost rectifier is chosen as an example to illustrate the variation of loop gain, output impedance and stability of the system due to the interaction with the input filter. The average model of the three-phase boost rectifier in rotating dq-coordinates [26] is given by Equation (5.9):

$$L \frac{di_d}{dt} = v_d - d'_d v_o \quad (5.9)$$

$$L \frac{di_q}{dt} = v_q - d'_q v_o$$

$$C \frac{dv_o}{dt} = \left(\frac{1}{2} \right) (d'_d i_d + d'_q i_q) - i_o.$$

If the duty cycles d_d and d_q are modified as follows:

$$d_d = d'_d + \frac{\omega L i_q}{v_o}, d_q = d'_q - \frac{\omega L i_d}{v_o}, \quad (5.10)$$

and the state equations reduce to:

$$\begin{aligned} L \frac{di_d}{dt} &= v_d - d'_d v_o \\ L \frac{di_q}{dt} &= v_q - d'_q v_o \\ C \frac{dv_o}{dt} &= \left(\frac{1}{2} \right) (d'_d i_d + d'_q i_q) - i_o. \end{aligned} \quad (5.11)$$

For notational simplicity, the primes for the modified duty cycles are dropped and they are used as the original duty cycles. Linearizing the system of differential equations around an operating point, we get:

$$\frac{d}{dt} \begin{bmatrix} \hat{i}_d \\ \hat{i}_q \\ \hat{v}_o \end{bmatrix} = \begin{bmatrix} 0 & 0 & -\frac{D_d}{L} \\ 0 & 0 & -\frac{D_q}{L} \\ \frac{D_d}{2C} & \frac{D_q}{2C} & 0 \end{bmatrix} \begin{bmatrix} \hat{i}_d \\ \hat{i}_q \\ \hat{v}_o \end{bmatrix} + \begin{bmatrix} -\frac{V_o}{L} & 0 \\ 0 & -\frac{V_o}{L} \\ \frac{I_d}{2C} & \frac{I_q}{2C} \end{bmatrix} \begin{bmatrix} \hat{d}_d \\ \hat{d}_q \end{bmatrix} + \begin{bmatrix} \frac{1}{L} & 0 & 0 \\ 0 & \frac{1}{L} & 0 \\ 0 & 0 & -\frac{1}{C} \end{bmatrix} \begin{bmatrix} \hat{v}_d \\ \hat{v}_q \\ \hat{i}_o \end{bmatrix}. \quad (5.12)$$

The variables D_d , D_q , I_d , I_q and V_o denote the operating point values of corresponding duty cycles, currents and voltage. The transfer function representation of the linearized system of equations given by Equation (7.12) is given below:

$$\begin{bmatrix} I_d(s) \\ I_q(s) \\ V_o(s) \end{bmatrix} = \begin{bmatrix} G_{idd} & G_{idq} \\ G_{iqd} & G_{iqq} \\ G_{vod} & G_{voq} \end{bmatrix} \begin{bmatrix} D_d(s) \\ D_q(s) \end{bmatrix} + \begin{bmatrix} Y_{dd} & Y_{dq} & A_{id} \\ Y_{qd} & Y_{qq} & A_{iq} \\ A_{vd} & A_{vq} & Z_o \end{bmatrix} \begin{bmatrix} V_d(s) \\ V_q(s) \\ I_o(s) \end{bmatrix}. \quad (5.13)$$

The boost rectifier is usually controlled by a two channel compensator, one for the regulation of the output voltage v_o and the other for the q -axis input current i_q . A block diagram representation of a controlled three-phase boost rectifier system is shown in Figure 5.9.

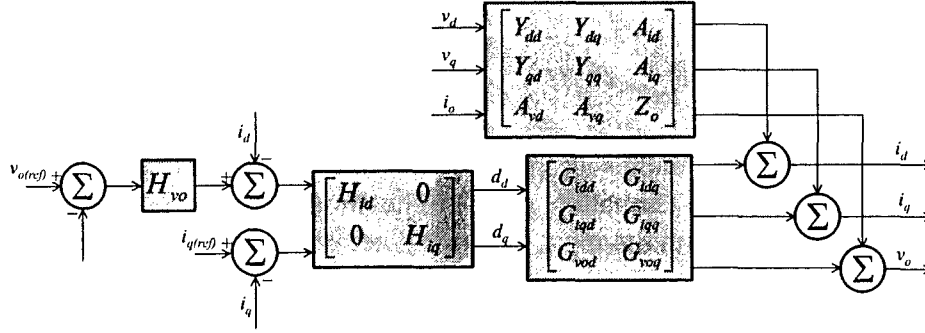


Figure 5.8. Block diagram of the controlled 3-Φ boost rectifier

H_{vo} represents the output voltage controller and H_{id} and H_{iq} , the current controllers. The output variables I_d , I_q and V_o are determined below after making the following definitions:

$$\begin{bmatrix} I_d \\ I_q \end{bmatrix} = I_c, \begin{bmatrix} V_d \\ V_q \end{bmatrix} = V_c, \begin{bmatrix} G_{idd} & G_{idq} \\ G_{iqd} & G_{iqq} \end{bmatrix} = G_{id}, \begin{bmatrix} G_{vod} & G_{voq} \end{bmatrix} = G_{vd}, \quad (5.14)$$

$$\begin{bmatrix} Y_{dd} & Y_{dq} \\ Y_{qd} & Y_{qq} \end{bmatrix} = Y_i, \begin{bmatrix} A_{vd} & A_{vq} \end{bmatrix} = A_v, \begin{bmatrix} A_{id} \\ A_{iq} \end{bmatrix} = A_i,$$

$$\begin{bmatrix} H_{id} & 0 \\ 0 & H_{iq} \end{bmatrix} = H_i, H_v = \begin{bmatrix} H_{id} H_{vo} \\ 0 \end{bmatrix}$$

$$\begin{bmatrix} D_d \\ D_q \end{bmatrix} = -[H_i \quad H_v] \begin{bmatrix} I_c \\ V_o \end{bmatrix} \quad (5.15)$$

$$\begin{aligned} \begin{bmatrix} I_c \\ V_o \end{bmatrix} &= -\begin{bmatrix} G_{id} \\ G_{vd} \end{bmatrix} [H_i \quad H_v] \begin{bmatrix} I_c \\ V_o \end{bmatrix} + \begin{bmatrix} Y_i & A_i \\ A_v & Z_o \end{bmatrix} \begin{bmatrix} V_c \\ I_o \end{bmatrix} \\ &= \begin{bmatrix} I + G_{id} H_i & G_{id} H_v \\ G_{vd} H_i & 1 + G_{vd} H_v \end{bmatrix}^{-1} \begin{bmatrix} Y_i & A_i \\ A_v & Z_o \end{bmatrix} \begin{bmatrix} V_c \\ I_o \end{bmatrix}. \end{aligned}$$

The reference vector is omitted from the Equation (5.14) because it does not affect the loop gain. The loop gain in Equation (5.15), is not a single transfer function as in the case of a DC-DC converter, but a transfer function matrix given by:

$$T(s) = \begin{bmatrix} G_{id} H_i & G_{id} H_v \\ G_{vd} H_i & G_{vd} H_v \end{bmatrix}. \quad (5.16)$$

The diagonal elements of $T(s)$ represent the current and voltage loop gains and the off-diagonal elements, the coupling between the two channels. The characteristic polynomial, the eigenvalues of which determine the stability of the closed loop system is given by:

$$\begin{aligned}\Phi_{CL} &= \det(I + T(s)) \\ &= \det((I + G_{id}H_i)(1 + G_{vd}H_v) - G_{id}H_vG_{vd}H_i).\end{aligned}\quad (5.17)$$

The closed loop output impedance, audiosusceptibility, and input admittance determined from Equation (5.15) are given in Equation (5.18). The modifications in the above expressions due to the interaction with the input filter are determined in the next section.

$$\begin{aligned}\begin{bmatrix} Y_i & A_i \\ A_v & Z_o \end{bmatrix}^{CL} &= (I + T(s))^{-1} \begin{bmatrix} Y_i & A_i \\ A_v & Z_o \end{bmatrix} \\ (I + T(s))^{-1} &= \begin{bmatrix} S^{-1}(1 + G_{vd}H_v) & -S^{-1}G_{id}H_v \\ -G_{vd}H_iS^{-1} & \frac{(I + G_{vd}H_iS^{-1}G_{id}H_v)}{(1 + G_{vd}H_v)} \end{bmatrix} \\ S &= (I + G_{id}H_i)(1 + G_{vd}H_v) - G_{id}H_vG_{vd}H_i.\end{aligned}\quad (5.18)$$

5.1.4. Effect of Input Filter on Rectifier Performance

The circuit schematic of one phase of a typical input filter is shown in Figure 5.6. The corresponding state space representation of one phase is given by Equation (5.19):

$$\begin{aligned}\dot{x} &= A_f x + B u \\ y &= C_f x.\end{aligned}\quad (5.19)$$

The dq model of the input filter derived based on the directions presented in Section 3 is shown in Figure 5.10. The corresponding state space representation of the dq model is given by Equation (5.20).

$$\begin{aligned}\begin{bmatrix} \dot{x}_d \\ \dot{x}_q \end{bmatrix} &= \begin{bmatrix} A_f & \omega_s I \\ -\omega_s I & A_f \end{bmatrix} \begin{bmatrix} x_d \\ x_q \end{bmatrix} + \begin{bmatrix} B_f & 0 \\ 0 & B_f \end{bmatrix} \begin{bmatrix} u_d \\ u_q \end{bmatrix} \\ \begin{bmatrix} y_d \\ y_q \end{bmatrix} &= \begin{bmatrix} C_f & 0 \\ 0 & C_f \end{bmatrix} \begin{bmatrix} x_d \\ x_q \end{bmatrix}\end{aligned}\quad (5.20)$$

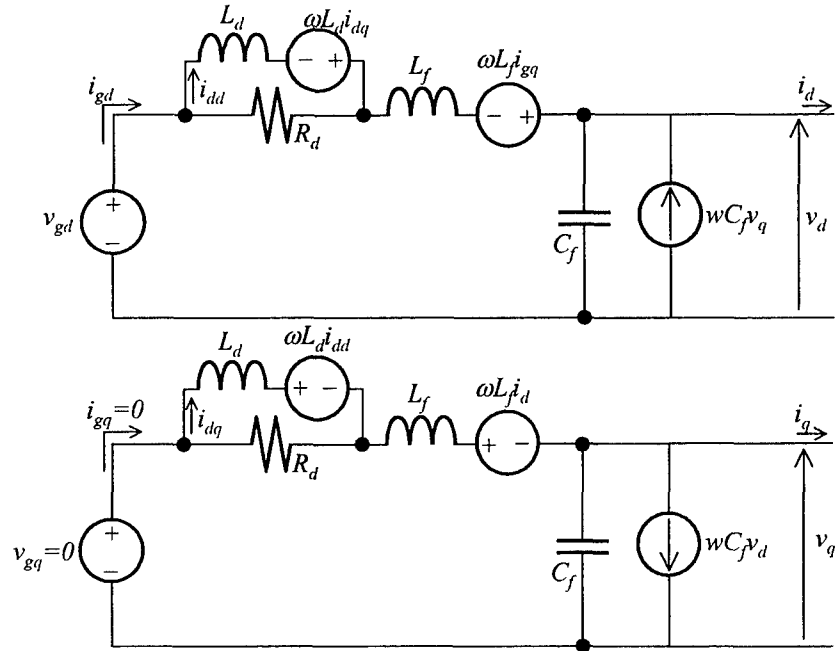


Figure 5.9. *DQ*-Equivalent circuit model of three phase input filter

The transfer function representation of the Equation (5.20) is then:

$$\begin{bmatrix} Y_d(s) \\ Y_q(s) \end{bmatrix} = \begin{bmatrix} M(s) & N(s) \\ -N(s) & M(s) \end{bmatrix} \begin{bmatrix} U_d(s) \\ U_q(s) \end{bmatrix}, \quad (5.21)$$

where

$$\begin{aligned} M(s) &= C_f (sI - A_f) \left[(sI - A_f)^2 + \omega_s^2 I \right]^{-1} B_f \\ N(s) &= \omega_s C_f \left[(sI - A_f)^2 + \omega_s^2 I \right]^{-1} B_f, \end{aligned} \quad (5.22)$$

and ω_s is the angular frequency of the input supply voltage. Figure 5.11 shows how the input filter affects the input currents and output voltage of the boost rectifier.

Due to the interaction with the input filter, Equation (5.15) gets modified as follows:

$$\begin{bmatrix} I_c \\ V_o \end{bmatrix} = \begin{bmatrix} I + G_{id}H_i + Y_iZ_{of} & G_{id}H_v \\ G_{vd}H_i + A_vZ_{of} & 1 + G_{vd}H_v \end{bmatrix}^{-1} \begin{bmatrix} Y_iH_f & A_i \\ A_vH_f & Z_o \end{bmatrix} \begin{bmatrix} V_g \\ I_o \end{bmatrix}. \quad (5.23)$$

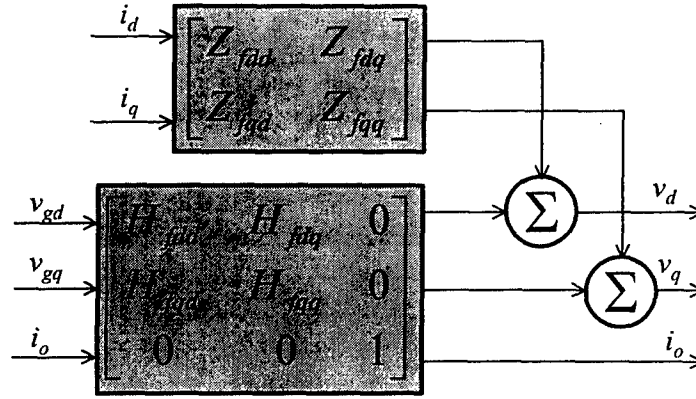


Figure 5.10. Effect of input filter on output variables of the rectifier

The characteristic polynomial is given by Equation (5.24). The last part of Equation (5.24) is obtained from the expression derived in Equation (5.18) for the closed loop input admittance.

$$\begin{aligned}
 \Phi_{CL(filt)} &= \det((I + G_{id}H_i + Y_iZ_{of})(1 + G_{vd}H_v)) \\
 &\quad - G_{id}H_v(G_{vd}H_i + A_vZ_{of}) \\
 &= \det(I + T(s)) \times \\
 &\quad \det\left(I + \left((I + G_{id}H_i)^{-1}Y_i - \frac{G_{id}H_vA_v}{\det(I + T(s))}\right)Z_{of}\right) \\
 &= \det(I + T(s))\det(I + Y_i^{CL}Z_{of})
 \end{aligned} \tag{5.24}$$

The origin of the minor loop gain, “ $Y_i^{CL}Z_{of}$ ” can be clearly seen in Equation (5.24). The stability of the interconnected system is now given by stability of the controller loops and of the minor loop due to the interaction. Thus, the stability of interconnection is determined by the zeros of $\det(I + Y_i^{CL}Z_{of})$. It is obvious that the smaller the “magnitude” of the minor loop gain is compared to unity, lesser is the effect of the interaction due to the input filter on the performance and stability of the converter.

5.1.5. Sufficient Condition for Stability

According to the multivariable Nyquist criterion [27], the interconnected system is internally stable if the number of counterclockwise encirclements of the origin made by the Nyquist contour of $\det(I + Y_i^{CL}Z_{of})$ is equal to the number of right half plane poles of Y_i^{CL} and Z_{of} . Since Y_i^{CL} and Z_{of} are transfer function matrices, it is quite difficult to relate their individual elements to the characteristic polynomial $\det(I + Y_i^{CL}Z_{of})$. Hence, the criterion for stability must be simplified so that it lends itself to direct physical insight and can be used efficiently in a design procedure. In the following, a sufficient condition for stability is derived based on the singular values of input admittance Y_i^{CL} , and output impedance Z_{of} matrices. From Figure 5.9 and Equation (5.15), the voltage at the output terminals of the filter can be determined as given by Equation (5.25). Equation (5.25)

shows the existence of a feedback loop as shown in Figure 5.2, the only difference in this case being that the elements of the feedback loop are transfer function matrices.

$$\begin{bmatrix} V_d \\ V_q \end{bmatrix} = \left[I + \underbrace{\begin{bmatrix} Z_{fdd} & Z_{fdq} \\ Z_{fqd} & Z_{fqq} \end{bmatrix}}_{Z_{of}} \underbrace{\begin{bmatrix} Y_{dd}^{CL} & Y_{dq}^{CL} \\ Y_{qd}^{CL} & Y_{qq}^{CL} \end{bmatrix}}_{Y_i^{CL}} \right]^{-1} \underbrace{\begin{bmatrix} H_{fdd} & H_{fdq} \\ H_{fqd} & H_{fqq} \end{bmatrix}}_{\begin{bmatrix} V_{sd} \\ V_{sq} \end{bmatrix}} \begin{bmatrix} V_{gd} \\ V_{gq} \end{bmatrix} \bigg|_{I_o=0} \quad (5.25)$$

$$\begin{bmatrix} V_d \\ V_q \end{bmatrix} = \left[I + Z_{of} Y_i^{CL} \right]^{-1} \begin{bmatrix} V_{sd} \\ V_{sq} \end{bmatrix}$$

According to the small gain theorem, a sufficient condition for stability is to ensure that the product of the incremental gains of the systems comprising the feedback loop is less than unity for all ω . The incremental gain of a linear, time invariant, stable system is its maximum singular value. The theory of singular values of a matrix and its application to the study of multivariable systems has been well established [27]. In simple terms, the singular values of a matrix represent its “modulus” or “gain” similar to the modulus of a scalar constant. Hence, the sufficient condition for stability is given by:

$$\bar{\sigma}(Y_i^{CL}(j\omega)) \bar{\sigma}(Z_{of}(j\omega)) < 1. \quad (5.26)$$

The sufficient condition for stability also turns out to be the condition that ensures minimal interaction between the input filter and the converter as shown:

$$\left| \det(I + Y_i^{CL}(j\omega) Z_{of}(j\omega)) \right| \leq \left(1 + \bar{\sigma}(Y_i^{CL}(j\omega)) \bar{\sigma}(Z_{of}(j\omega)) \right)^2. \quad (5.27)$$

Hence, satisfying Equation (5.26) not only ensures the stability of the minor loop gain (and hence of the integrated system), but also that its modulus is closer to 1 than to zero so that the characteristic polynomial given by Equation (5.24) is not appreciably different from that given by Equation (5.17).

Simplifying Approximations

In this section, approximate expressions for the singular values of Y_i^{CL} and Z_{of} are derived based on the knowledge of the physical properties of the system. The three-phase rectifier, as mentioned before, regulates i_q to a reference value to provide unity power factor at the input. This reference value is determined as a function of the real power P , supplied by the rectifier and the input voltage. It provides a tightly regulated DC output and hence constant power for a given load. Thus, a simplified model of the rectifier that is valid at low frequencies can be represented as shown in Figure 5.12.

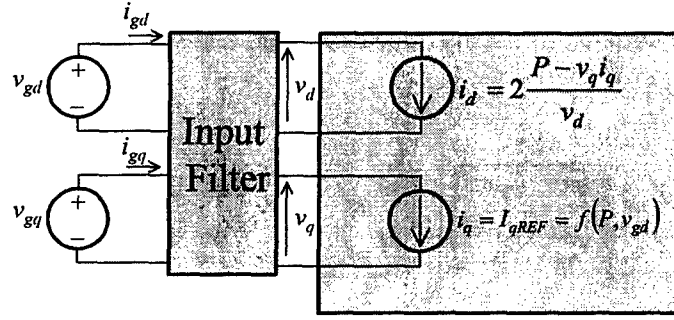


Figure 5.11. Low frequency model of 3-Φ rectifier with input filter

The function f , in Figure 5.12, used to determine I_q is static with no time dependent dynamics. Hence, the input admittance of the rectifier and its singular values according to Figure 5.12 are then given by:

$$Y_i^{CL} \approx Y_i^{DC} = \begin{bmatrix} Y_{dd} & Y_{dq} \\ 0 & 0 \end{bmatrix} = \begin{bmatrix} -2 \frac{P - V_q I_q}{V_d^2} & 2 \frac{I_q}{V_d} \\ 0 & 0 \end{bmatrix} \quad (5.28)$$

$$\bar{\sigma}(Y_i^{CL}) \approx \bar{\sigma}(Y_i^{DC}) = \sqrt{|Y_{dd}|^2 + |Y_{dq}|^2}.$$

The output impedance of the input filter, from Equation (5.21), is given by:

$$Z_{of} = \begin{bmatrix} M(s) & N(s) \\ -N(s) & M(s) \end{bmatrix} \quad (5.29)$$

$$\begin{aligned} \bar{\sigma}(Z_{of}(j\omega)) &= \sqrt{|M(j\omega)|^2 + |N(j\omega)|^2 + 2|\text{Im}(M^*(j\omega)N(j\omega))|} \\ &\leq |M(j\omega)| + |N(j\omega)|. \end{aligned}$$

$M(s)$ and $N(s)$ are as defined in Equation (5.21) with the appropriate choice of B_f and C_f matrices. It can be easily shown that the imaginary parts of the eigenvalues of the dq -model of the filter are symmetrically displaced from the values for the single-phase model by the angular frequency ω_s of the input voltages.

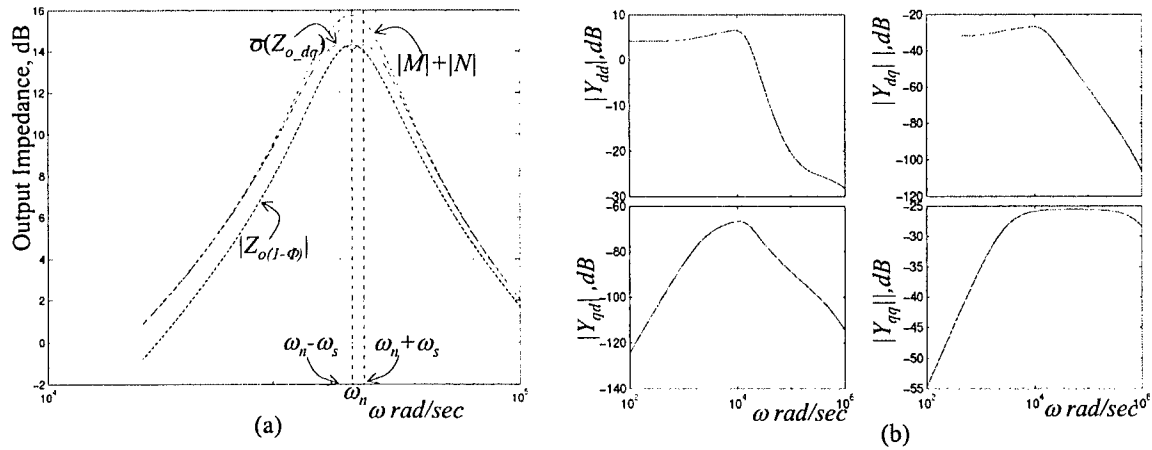


Figure 5.12. (a) Output Impedance of Input Filter (b) Input Admittance of Boost Rectifier

Figure 5.13 shows the input admittance and output impedance transfer functions of the boost rectifier and input filter respectively to illustrate the approximations made in Equations (5.28) and (5.29).

Simulation Results

The interaction between the input filter and the converter is shown in Figure 5.14 for two sets of parameter values for the input filter, one that results in appreciable impedance overlap and hence strong interaction (Figure 5.14a) and another with no impedance overlap and minimal interaction (Figure 5.14b). The singular values of the input admittance and output impedance of the rectifier and the filter respectively are plotted as a function of frequency. The voltage loop gain of the rectifier with and without the input filter is also shown in Figure 5.14 to illustrate the effect of the interaction due to the input filter. It can be seen that the voltage loop gain of the rectifier is unaffected by the input filter when the impedance overlap is minimal. On the other hand, a significant impedance overlap results in an appreciable degradation of the voltage loop gain of the rectifier. However, this does not necessarily cause the system to become unstable because the impedance ratio criterion is only a sufficient condition for stability.

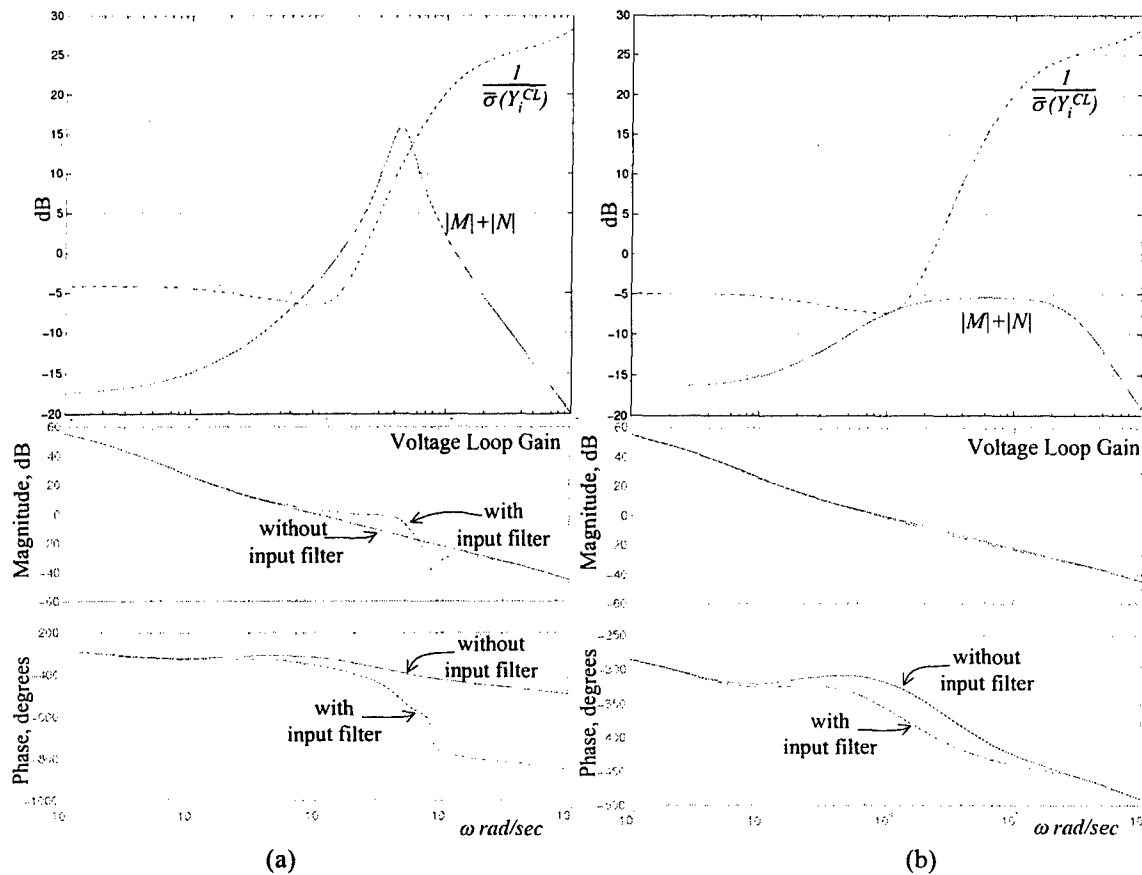


Figure 5.13. Impedance overlap and voltage loop gain of the rectifier system with and without input filter (a) Strong Interaction (b) Minimal interaction

5.2 Stability under bidirectional power flow

The impedance ratio criterion used to guarantee minimal interaction and stability of interconnected systems is based on the linearized models of subsystems around a nominal operating point. It guarantees only local stability in a small neighborhood of the equilibrium point. Hence, the behavior of the system when subjected to a large disturbance cannot be predicted using such linear analysis techniques. Methods that accommodate the nonlinear characteristics of the system must then be used to obtain a global understanding of the system behavior. The use of nonlinear methods for the stability and subsystem interaction analysis of interconnected systems is discussed in this chapter.

It was shown in Section 4.3 that the piezoelectric actuator could actively damp the mechanical structure by controlling the actuator current to be proportional to the acceleration of the structure. It was also shown that the actuator, in actively damping the structure, absorbs the mechanical energy fed from the external disturbance force and redirects it back to the electrical source. As a result, there is a net flow of real power back

to the DC bus from the actuator in addition to the circulating reactive power due to the capacitive nature of the actuator. It is critical to determine if this regenerative power has any detrimental effects on the stability of the drive amplifier. To this end, the analysis of the stability of an integrated system consisting of a regulated power converter with an input filter under bidirectional power flow is presented in this section. The analysis is simplified in that it is assumed that there is no circulating reactive power at the converter output. It is found that the forward direction of power flow is more critical from a stability point of view. In other words, the flow of power in the reverse direction does not destabilize the system if stability is maintained in the forward direction.

5.2.1. Stability under Bidirectional Power Flow

A simple nonlinear system consisting of a regulated power converter modeled as a constant power load followed by an input filter is used for the study [28]. Figure 5.15 shows a simplified schematic of a regulated power converter with an input filter.

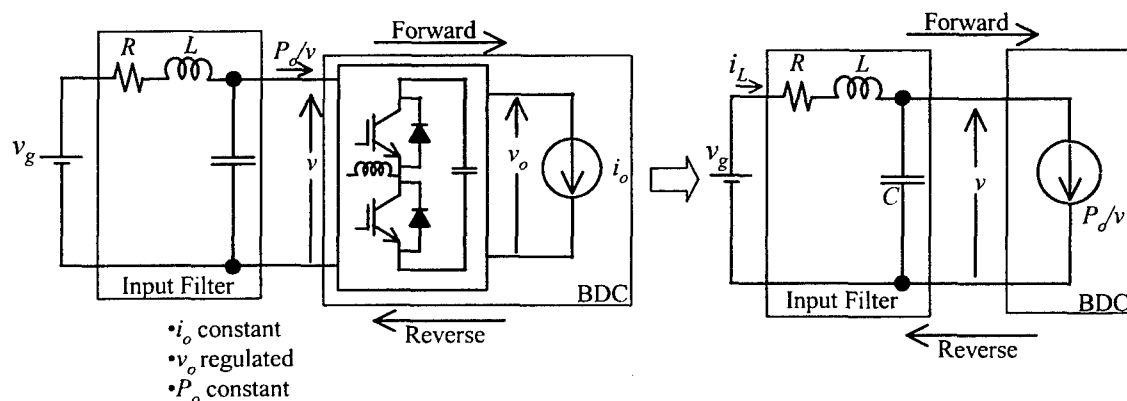


Figure 5.15. Regulated Converter with Input Filter

The stability of this interconnected system under conditions of bidirectional power flow will be investigated in this section. This system consists of a regulated bidirectional power converter connected to a source through an input filter. The output of the converter is connected to an ideal load modeled by a current source. Under constant load conditions, the power delivered to the load is constant because the output voltage of the converter is regulated. The regulated converter thus appears as a constant power load to a system that is connected at its input. The constant power curve of this converter is shown in Figure 5.16 by the solid curve when the power is flowing to the load. When the load is regenerating power, the constant power curve is shown by the dotted line in the fourth quadrant of the graph. The constant power curves in Figure 5.16 show that the system in Figure 5.15 is fundamentally a nonlinear system, and that the converter and load appears as a negative impedance to the source when the power is flowing in the forward direction as shown. When the direction of power flow reverses, the input impedance of the converter subsystem changes sign as can be clearly observed in Figure 5.16.

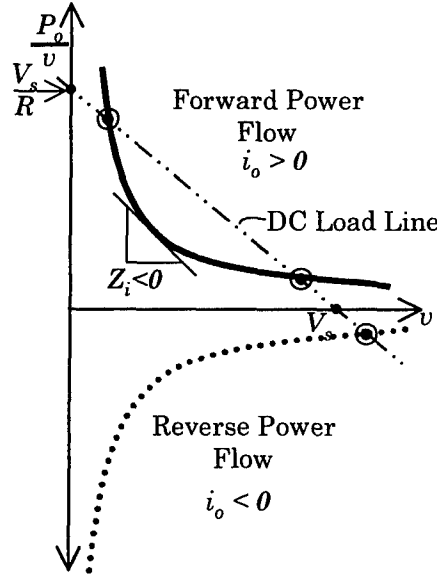


Figure 5.16. Constant Power Characteristics of a Regulated Power Converter

The state equations for the system shown in Figure 5.16 are given below:

$$\begin{aligned} L \frac{di_L}{dt} &= v_g - Ri_L - v \\ C \frac{dv}{dt} &= i_L - \frac{P_o}{v} \end{aligned} \quad (5.30)$$

The equilibrium solutions for the system are given by:

$$\begin{aligned} I_{Le} &= \frac{P_o}{V_e} \\ V_e &= \frac{V_g}{2} \left(1 \pm \sqrt{1 - 4R \frac{P_o}{V_g^2}} \right) \end{aligned} \quad (5.31)$$

The equilibrium points for the system are also determined from the points of intersection between the DC load line and the constant power characteristics of the power converter. This is illustrated in Figure 5.16. Equilibrium solutions exist as long as the load line intersects the constant power curve. In the forward direction, the load lines for $R \leq V_g^2 / 4P_o$ intersect the constant power curve. Equilibrium points do not exist for $R > V_g^2 / 4P_o$. On the other hand, there exist equilibrium points for all values of R in the reverse direction. This can be inferred from the expressions for the equilibrium solutions in Equation (5.31). Real equilibrium solutions for V_e exist only for $R \leq V_g^2 / 4P_o$. However, for reverse power flow when P_o is negative equilibrium solutions exist for all values of R .

The stability of the equilibrium points depends on the parameter values. To make the stability analysis practical meaningful, the constant power characteristic of the regulated power converter is redrawn to have a finite area under it as shown in Figure 5.17 [28,29].

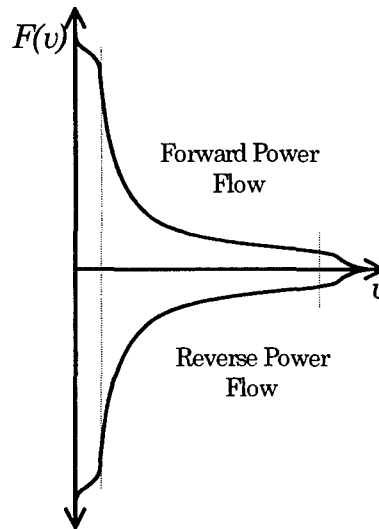


Figure 5.17 Constant Power Characteristics of a Regulated Power Converter

The criterion for complete stability is given below:

Definition Complete Stability [28]: A system is said to be “completely stable” if there exist finitely many equilibrium solutions and every solution for the system equations approaches an equilibrium solution.

Theorem (Brayton and Moser): A dynamic system described by the state equations:

$$\begin{aligned}\dot{x} &= -Ax + Bu \\ \dot{y} &= Dx - f(y),\end{aligned}\tag{5.32}$$

with the following conditions:

1. A is symmetric and positive definite
2. $B = -D^T$
3. The Jacobian df/dy is symmetric and $B^T A^{-1} y + f(y) = \text{Grad } G(y)$

The latter condition is true if:

1. $\|A^{-1}B\| < 1$
2. $G(y) \rightarrow \infty$ as $|y| \rightarrow \infty$.

To fit the system in Figure 5.15 within the framework of the theorem given above, the following definitions are made:

$$\begin{aligned}
x &:= i_L & y &:= \sqrt{\frac{C}{L}}(v - V_g) \\
A &:= -\frac{R}{L} & B = -D &= -\frac{1}{\sqrt{LC}} \\
f(y) &= \frac{1}{\sqrt{LC}} F\left(\sqrt{\frac{L}{C}} + V_g\right),
\end{aligned} \tag{5.34}$$

where $F(v)$ is as shown in Figure 5.17.

Test for Stability:

$$\begin{aligned}
1. \quad & \|A^{-1}B\| < 1 \Rightarrow \sqrt{\frac{L}{C}} < R \\
2. \quad & G(y) = \frac{1}{2RC} y^2 + \frac{1}{\sqrt{LC}} \int_0^y F\left(\sqrt{\frac{L}{C}}\sigma + V_g\right) \cdot d\sigma.
\end{aligned} \tag{5.35}$$

If $F(v)$ is as shown in Figure 5.17, $G(y) \rightarrow \infty$ as $|y| \rightarrow \infty$ and complete stability is ensured if:

$$\sqrt{\frac{L}{C}} < R. \tag{5.36}$$

Thus, the stability region can be defined for the forward direction as shown in Figure 5.18. The forward direction of power flow is hence, most critical from the stability standpoint (i.e.) as long as stability is guaranteed in the forward direction, it is preserved in the reverse direction up to the same power level. The reversal of power flow results in the input impedance of the converter system changing sign. The reasons for potential instability due the negative input impedance of the converter thus cease to exist during regeneration.

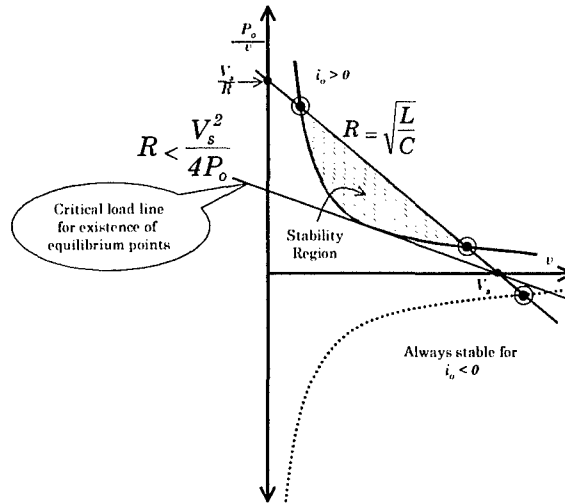


Figure 5.18. Stability of Equilibrium Solutions

This result can be further corroborated by the impedance ratio criterion. Nyquist contours of the loop gain $Z_{o1}Y_{i2}$ are shown in Figure 5.19 as a function of the load current.

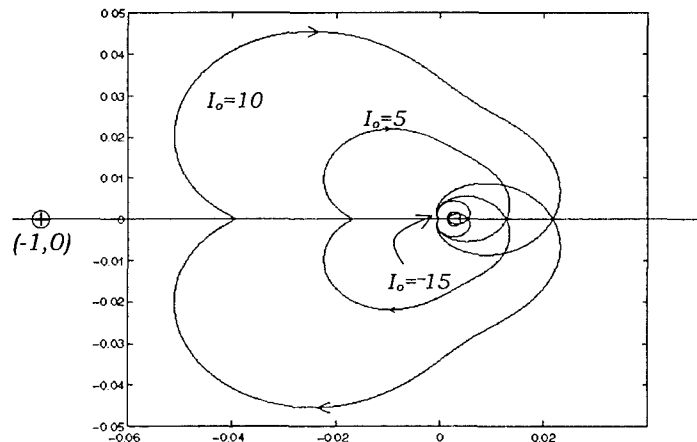


Figure 5.19. Stability of Interconnected System under reversal of power flow

Z_{o1} and Y_{i2} represent the output impedance and the input admittance respectively of the input filter and power converter respectively. It can be seen that the Nyquist plots move further away from the $(-1, 0)$ as the load current changes sign and hence reverses the power flow. The foregoing analysis thus suggests that the overall system stability is determined by the stability of the system when the power is flowing in the forward direction.

5.3 Bifurcation Methods

The use of nonlinear methods to study the global stability and interaction behavior of interconnected systems is continued in this section with the application of bifurcation methods. The term “Bifurcation” is used to indicate a qualitative change in the properties of a system as a function of one or more parameters known as bifurcation parameters. The changes typically are in the number, type and stability of solutions to the dynamic

equations that describe system behavior. Typically, a system is said to bifurcate when its equilibrium point loses stability at a given operating condition. These analysis methods are then primarily concerned in the post-bifurcation behavior of the system. That is, they provide information about the characteristics of the system after the equilibrium point loses stability. Linear analysis methods, however, can only predict the loss of stability of the equilibrium point.

In bifurcation problems, it is useful to consider a space comprising the state variables and the bifurcation parameters. Bifurcation points are identified in this space by observing changes in system properties as a function of a chosen set of bifurcation parameters. A physical understanding of the subsystem being analyzed motivates the choice of bifurcation parameter(s).

The use of bifurcation methods for the study of global stability is demonstrated using two examples of interconnected systems. The interaction between a regulated DC-DC buck converter and an EMI input filter is studied first. The buck converter is represented by its average model in order to capture only the system level, low frequency interactions with the input filter. The damping resistance in the input filter is chosen as the bifurcation parameter. The bifurcation behavior of the system is studied as the damping resistance varies. The results are then compared with those obtained from the application of the impedance ratio criterion. The second example deals with the study of interaction at the DC bus of a simplified power distribution represented as a single source-single load system. The source subsystem is a three-phase boost rectifier that feeds the 270V DC bus of the power distribution system. The rectifier is represented by its average model in rotating dq coordinates synchronized with the input line voltages. The load subsystem is a regulated DC-DC buck converter with a front-end input filter. The load converter is modeled as a constant power load similar to that studied in [28]. The voltage controller gain of the three-phase boost rectifier is chosen as the bifurcation parameter as it is directly related to the voltage regulation bandwidth of the rectifier. The dependence of the bifurcation behavior of the system as a function of the total power at the DC bus is discussed. The applicability of these methods to a practical design procedure is explored.

5.3.1. Input Filter Interaction

The circuit schematic of a regulated DC-DC buck converter with an input filter is shown in Figure 5.20 [30].

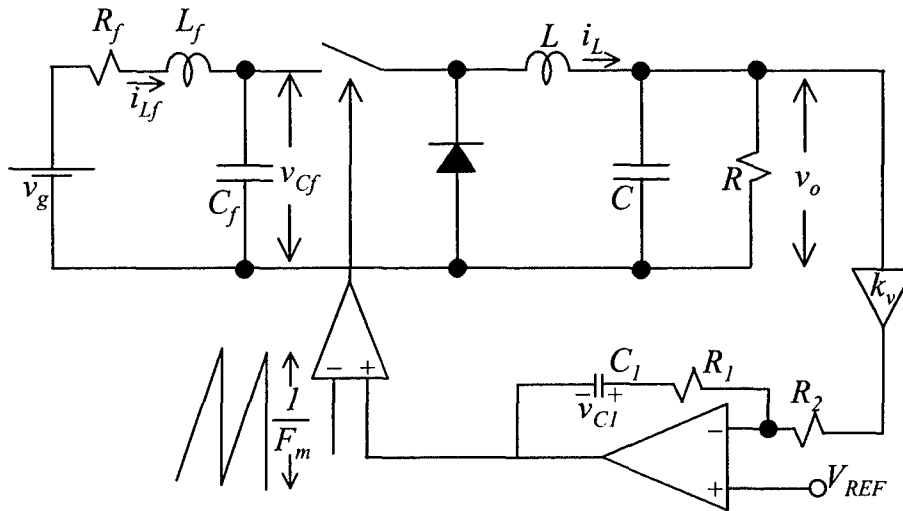


Figure 5.20. DC-DC Buck Converter with Input Filter

The resistance R_f in the input filter is chosen as the bifurcation parameter and the system behavior as a function of R_f is studied. The converter is regulated by a simple PI voltage controller as shown in Figure 5.20. The integrated filter converter system with the PWM switch in Figure 9.1 replaced by its average model is shown in Figure 5.21. Since the bifurcation analysis is performed on the average model of the converter, interactions with frequencies in the switching frequency range between the converter and the filter cannot be captured by this method.

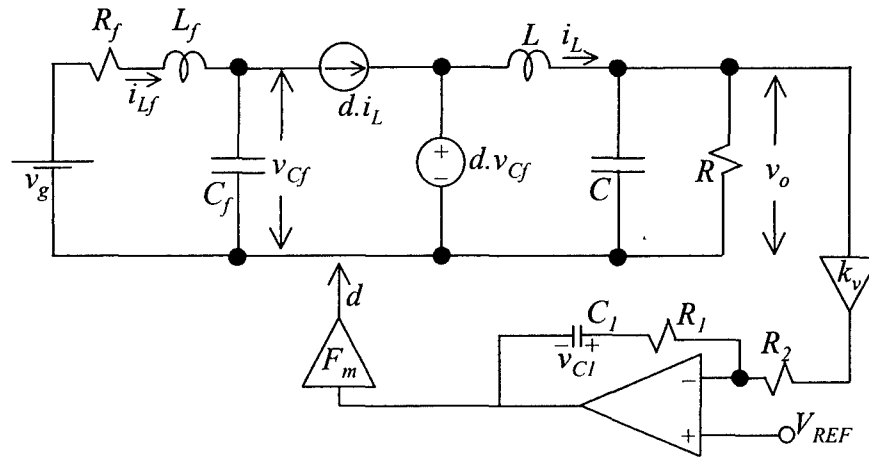


Figure 5.21. Average Model of DC-DC Buck Converter with Input Filter

Denoting the gain R_1/R_2 by h_o , the dynamic state space equations of the average model shown in Figure 5.21 are given below:

$$\begin{aligned}
L \frac{di_L}{dt} &= (1+h_o) F_m V_{REF} v_{Cf} - h_o k_v F_m v_o v_{Cf} - F_m v_{C1} v_{Cf} - v_o \\
C \frac{dv_o}{dt} &= i_L - \frac{v_o}{R} \\
L_f \frac{di_{Lf}}{dt} &= v_g - R_f i_{Lf} - v_{Cf} \\
C_f \frac{dv_{Cf}}{dt} &= i_{Lf} - (1+h_o) F_m V_{REF} i_L + h_o k_v F_m i_L v_o + F_m v_{C1} i_L \\
C_1 \frac{dv_{C1}}{dt} &= \frac{1}{R_1} (k_v v_o - V_{REF}).
\end{aligned} \tag{5.37}$$

The duty cycle d , is given by:

$$d = \left[(1+h_o) V_{REF} - h_o k_v v_o - v_{C1} \right] F_m. \tag{5.38}$$

To reduce notational clutter, the state equations for the system are written as:

$$\dot{x} = f(x; R_f), \tag{5.39}$$

where x , represents the state vector $[i_L \ v_o \ i_{Lf} \ v_{Cf} \ v_{C1}]^T$. The equilibrium solutions $x_e = [I_{Le} \ V_{oe} \ I_{Lfe} \ V_{Cfe} \ V_{Cle}]^T$ for the system are determined by setting the state derivatives in Equation (5.37) equal to zero and solving the resulting system of algebraic equations.

$$0 = f(x; R_f) \Rightarrow x = x_e \tag{5.40}$$

The equilibrium solutions are given by:

$$\begin{aligned}
I_{Le} &= \frac{V_{REF}}{k_v} \cdot \frac{1}{R} \\
V_{oe} &= \frac{V_{REF}}{k_v} \\
I_{Lfe} &= \frac{\left(\frac{V_{REF}}{k_v}\right)^2 \cdot \frac{1}{R}}{V_g \pm \sqrt{V_g^2 - 4 \frac{R_f}{R} \left(\frac{V_{REF}}{k_v}\right)^2}} \\
V_{Cfe} &= V_g \pm \sqrt{V_g^2 - 4 \frac{R_f}{R} \left(\frac{V_{REF}}{k_v}\right)^2} \\
V_{Cle} &= V_{REF} - \frac{V_{REF}}{k_v} \cdot \frac{1}{V_g \pm \sqrt{V_g^2 - 4 \frac{R_f}{R} \left(\frac{V_{REF}}{k_v}\right)^2}}.
\end{aligned} \tag{5.41}$$

The loci of the equilibrium solutions as a function of R_f is shown in Figure 5.22.

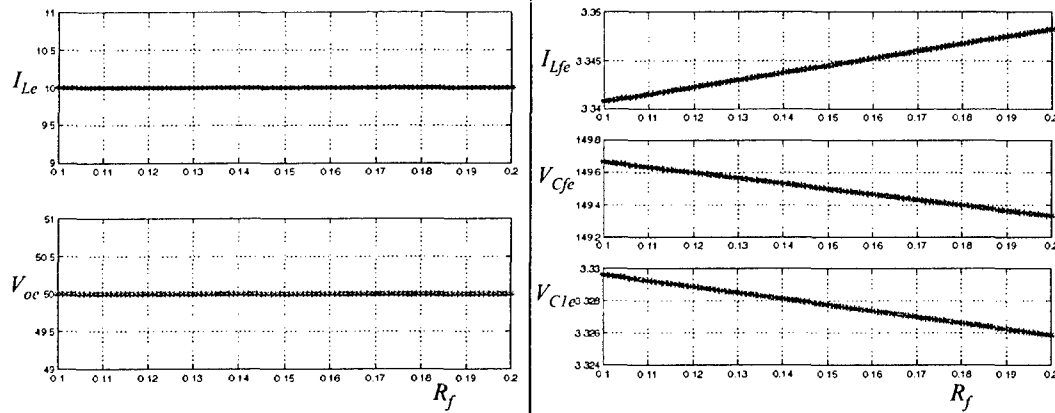


Figure 5.22. Loci of Equilibrium Solutions as a Function of R_f

The linearized system equations around the equilibrium solutions defined by Equation (5.41) are given by Equation (5.42). The location of the eigenvalues of the linearized system determines the stability of the system in the neighborhood of the equilibrium point x_e .

$$J(x_e; R_f) = \left. \frac{\partial f(x; R_f)}{\partial x} \right|_{x=x_e} \tag{5.42}$$

As the eigenvalues move in the complex plane as a function of the control parameter, the system loses stability for a particular value of R_f in one of two ways as shown in Figure 5.23.

An eigenvalue moves to the right half plane through the origin. This is called a static bifurcation. A pair of complex conjugate eigenvalues moves to the right half plane with non-zero imaginary parts. This is called a dynamic or Andronov-Hopf bifurcation.

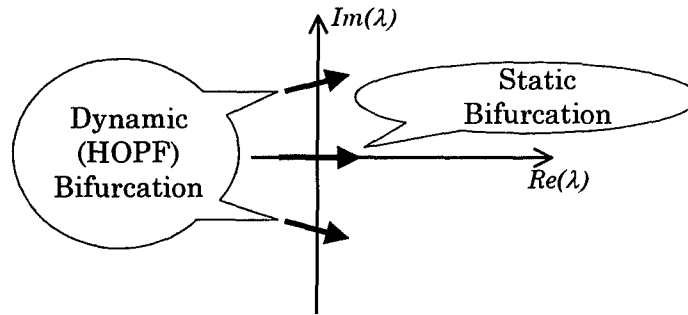


Figure 5.23. Loss of System Stability

The loci of eigenvalues of the linearized system for the DC-DC buck converter with input filter is shown in Figure 5.24. It can be seen that a pair of complex conjugate eigenvalues λ_1 and λ_2 , move to the right half of the complex plane with non-zero imaginary parts. The system thus suffers a dynamic Andronov-Hopf bifurcation. An Andronov-Hopf bifurcation indicates the existence of periodic solutions. The stability of the periodic solutions near the bifurcation point is determined by the type of bifurcation.

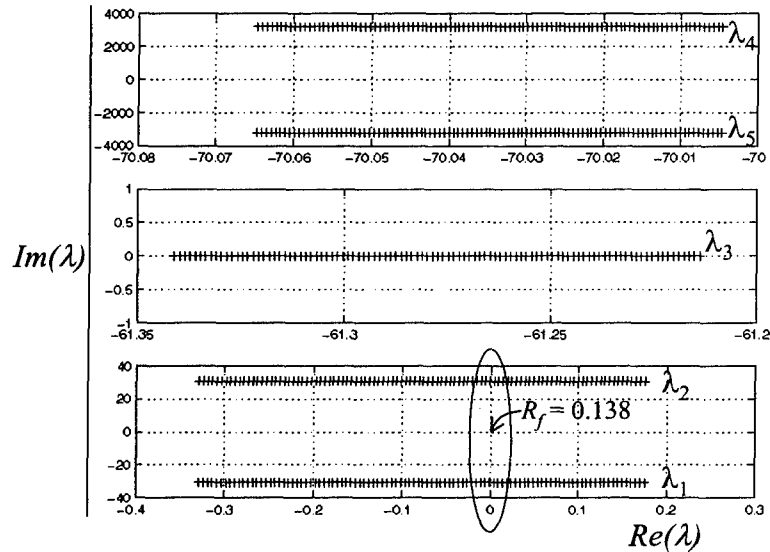


Figure 5.24. Loci of Eigenvalues of Linearized System as a function of R_f

A Hopf bifurcation is further classified as supercritical and subcritical. By using perturbation methods, “Normal Form” equations [31] that describe the behavior of the system near the bifurcation points are derived. The generic normal form equations for a Hopf bifurcation are given below:

$$\begin{aligned}\dot{a} &= \mu a + \alpha a^3 \\ \dot{\theta} &= \omega + \beta a^2.\end{aligned}\tag{5.43}$$

Depending on the sign of α , the bifurcation is supercritical or subcritical. A negative α indicates a supercritical Hopf and a positive α , a subcritical Hopf. A subcritical Hopf bifurcation is characterized by unstable periodic solutions bifurcating from the Hopf point. A supercritical Hopf bifurcation would, on the other hand, have stable periodic solutions bifurcating from the Hopf point. For the system under study, the bifurcation was found to be subcritical. The complete bifurcation diagram of the DC-DC buck converter with input filter is shown in Figure 5.25. The periodic solutions that bifurcate from the Hopf point are numerically constructed using shooting methods. A branch of periodic solutions as a function of the control parameter R_f can then be traced using one of several methods such as sequential, arc-length or pseudo arc-length continuation. The stability of the bifurcating periodic solutions is determined using Floquet theory. The construction, branch continuation and determination of stability of periodic solutions are explained in detail in the following section.

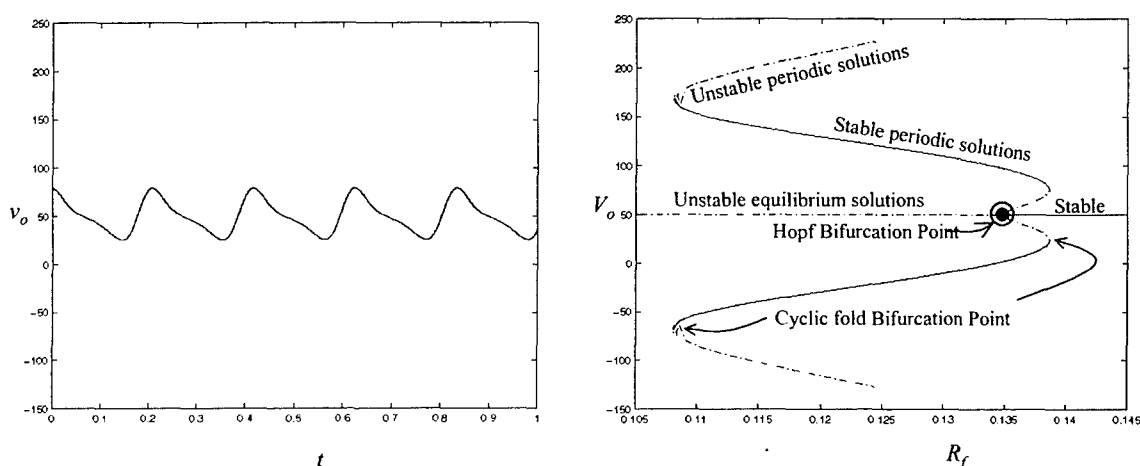


Figure 5.25. Bifurcation Diagram of DC-DC Buck Converter with Input Filter

Construction and Stability of Periodic Solutions

The construction of periodic solutions basically involves the determination of initial conditions, x_o and a solution, $x(t; x_o)$ with a minimal period T for the system equations (Equation (5.37)) such that $x(T; x_o) = x_o$. To absorb the problem of determining the minimal period T of the periodic solutions into that of the initial conditions x_o , the following transformations are performed on the state equations.

$$\begin{aligned}
t &= \tau T \\
\frac{dx}{dt} &= \frac{dx}{d\tau} \cdot \frac{d\tau}{dt} = \frac{1}{T} \frac{dx}{d\tau} \\
\Rightarrow x' &= \frac{dx}{d\tau} = T \frac{dx}{dt} = T \cdot \dot{x} = T \cdot f(x; R_f).
\end{aligned} \tag{5.44}$$

The augmented state equations with initial conditions are given below in Equation (5.45):

$$\begin{aligned}
x' &= Tf(x; R_f) \\
T' &= 0
\end{aligned} \quad \begin{bmatrix} x(1; x_o) - x_o \\ x_k(0) - \eta \end{bmatrix} = 0. \tag{5.45}$$

The initial condition, $x_k(0) = \eta$ in Equation (5.45) represents a phase condition for one of the state variables to account for additional state equation that was introduced due to the normalization.

To trace a branch of periodic solutions as a function of the control parameter R_f , the initial condition x_o and the minimal period T need to be determined with R_f as the continuation parameter along the branch. On the other hand, subsequent values of R_f at appropriate intervals along the branch of the periodic solutions can be determined by the continuation algorithm itself if the arc length s , is chosen as the continuation parameter. Hence, R_f is added as an additional state variable to the transformed state equations. The augmented state vector and the dynamic equations are denoted by an underscore as shown in Equation (5.46).

$$\begin{aligned}
x' &= Tf(x; R_f) \\
T' &= 0 \\
R_f' &= 0
\end{aligned} \quad \begin{bmatrix} x(1; x_o) - x_o \\ x_k(0) - \eta \\ p(x_o, T, R_f, s) \end{bmatrix} = 0 \tag{5.46}$$

$$\begin{aligned}
\underline{x}' &= \underline{f}(\underline{x}) \quad G(\underline{x}_o) = 0 \\
\underline{x} &= [x^T \quad T \quad R_f]^T
\end{aligned}$$

The initial conditions x_o , minimal period T and, R_f are determined as a solution to a two-point boundary value problem [31,32]. The problem to be solved is given by Equation (5.46). The additional boundary condition in Equation (5.46) is given by:

$$\begin{aligned}
p(x_o, T, R_f, s) &= \varsigma \sum_{i=1}^5 (x_{oi} - x_{oi}(s_j)) \frac{dx_{oi}}{ds} + \varsigma (T - T(s_j)) \frac{dT}{ds} \\
&\quad + (1 - \varsigma) (R_f - R_f(s_j)) \frac{dR_f}{ds} - (s - s_j).
\end{aligned} \tag{5.47}$$

The required initial condition $\underline{x}_o = [x_o^T \quad T \quad R_f]^T$ is that for which $G(x_o, T, R_f, x(1; x_o))$ given by Equation (5.48) is equal to zero.

$$G(x_o, T, R_f, x(1; x_o)) = G(\underline{x}_o, x(1; \underline{x}_o)) = \begin{bmatrix} x(1; x_o) - x_o \\ x_k(0) - \eta \\ p(x_o, T, R_f, s) \end{bmatrix} \quad (5.48)$$

A Newton-Raphson iterative procedure explained below is used to determine the initial conditions. An initial guess $\underline{x}_o^{(i)}$ is used as a starting point. The subsequent solutions are found as follows:

$$\begin{aligned} G^{(i+1)} &= G^{(i)} + (\underline{x}_o^{(i+1)} - \underline{x}_o^{(i)}) G'^{(i)} = 0 \\ \Rightarrow \underline{x}_o^{(i+1)} &= \underline{x}_o^{(i)} - [G'^{(i)}]^{-1} G^{(i)}, \end{aligned} \quad (5.49)$$

where $G^{(i)} = G(\underline{x}_o^{(i)}, x(1; \underline{x}_o^{(i)}))$. The gradient of G at the i^{th} initial condition is given by:

$$\begin{aligned} G'^{(i)} &= \frac{\partial G}{\partial \underline{x}_o^{(i)}} + \frac{\partial G}{\partial x} \cdot \frac{\partial x(1; \underline{x}_o^{(i)})}{\partial \underline{x}_o^{(i)}} \\ &= B_o + B_1 \cdot Y(\tau) \Big|_{\tau=1}. \end{aligned} \quad (5.50)$$

The matrices B_o and B_1 are defined below assuming that the index k in the phase condition in Equation (5.48) is chosen as:

$$B_o = \begin{bmatrix} 1 & 0 & 0 & 0 & 0 & 0 & 0 \\ 0 & 1 & 0 & 0 & 0 & 0 & 0 \\ 0 & 0 & 1 & 0 & 0 & 0 & 0 \\ 0 & 0 & 0 & 1 & 0 & 0 & 0 \\ 0 & 0 & 0 & 0 & 1 & 0 & 0 \\ 0 & 0 & 0 & 1 & 0 & 0 & 0 \\ \frac{dx_{o1}}{ds} & \frac{dx_{o2}}{ds} & \frac{dx_{o3}}{ds} & \frac{dx_{o4}}{ds} & \frac{dx_{o5}}{ds} & \frac{dT}{ds} & \frac{dR_f}{ds} \end{bmatrix} \quad (5.51a)$$

$$B_1 = \begin{bmatrix} -1 & 0 & 0 & 0 & 0 & 0 & 0 \\ 0 & -1 & 0 & 0 & 0 & 0 & 0 \\ 0 & 0 & -1 & 0 & 0 & 0 & 0 \\ 0 & 0 & 0 & -1 & 0 & 0 & 0 \\ 0 & 0 & 0 & 0 & -1 & 0 & 0 \\ 0 & 0 & 0 & 0 & 0 & 0 & 0 \\ 0 & 0 & 0 & 0 & 0 & 0 & 0 \end{bmatrix} \quad (5.51b)$$

The derivatives in the last column of the matrix B_o are determined as follows. Assuming that the initial condition x_o , minimal period T and the control parameter R_f have been found on a particular point on a branch we have:

$$\begin{aligned}
 G(x_o, T, R_f, s) &= 0 \\
 \Rightarrow \frac{\partial G}{\partial x_o} \cdot \frac{\partial x_o}{\partial s} + \frac{\partial G}{\partial T} \cdot \frac{\partial T}{\partial s} + \frac{\partial G}{\partial R_f} \cdot \frac{\partial R_f}{\partial s} &= 0 \quad (5.52) \\
 \Rightarrow \begin{bmatrix} \frac{\partial x_o}{\partial s} \\ \frac{\partial T}{\partial s} \\ \frac{\partial R_f}{\partial s} \end{bmatrix} &= - \begin{bmatrix} \frac{\partial G}{\partial x_o} & \frac{\partial G}{\partial T} \\ \frac{\partial G}{\partial R_f} & 1 \end{bmatrix}^{-1} \frac{\partial G}{\partial R_f} \frac{\partial R_f}{\partial s}.
 \end{aligned}$$

The partial derivatives in Equation (5.52) are determined in terms of $\partial R_f / \partial s$. The vector is then normalized to have unit length. The quantities on the right hand side of Equation (5.52) are defined below:

$$\begin{aligned}
 \frac{\partial G}{\partial x_o} &= I - \frac{\partial x(1; x_o, R_f)}{\partial x_o} \quad (5.53) \\
 \frac{\partial G}{\partial T} &= f(x(1), x_o, R_f).
 \end{aligned}$$

The matrix $Y(\tau) = \frac{\partial x(\tau; \underline{x}_o^{(i)})}{\partial \underline{x}_o^{(i)}}$ in Equation (5.53) is the $n \times n$ fundamental solution defined by:

$$\begin{aligned}
 Y'(\tau) &= A(\tau)Y(\tau) \quad 0 < \tau < 1 \quad (5.54) \\
 Y(0) &= I \quad A(\tau) = \frac{\partial f(\underline{x}(\tau); \underline{x}_o)}{\partial \underline{x}(\tau)}.
 \end{aligned}$$

$A(\tau)$ represents the Jacobian of the linearized system around the constructed periodic solution. In the actual computation, the $A(\tau)$ and the solution $\underline{x}(\tau; \underline{x}_o)$ are replaced by their numerical approximations obtained by solving the problem with the initially guessed solutions.

After computing $Y(\tau) = \frac{\partial x(\tau; \underline{x}_o^{(i)})}{\partial \underline{x}_o^{(i)}} \Big|_{\tau=1}$, it is substituted in Equation (5.53) for the gradient

of G , which in turn yields the new solution from Equation (5.52). The procedure is repeated until a convergence condition is met and continued as a function of the arc length s . The stability of the bifurcating periodic solutions is determined using Floquet

theory [31]. After a periodic solution $x(t; x_o)$ with minimal period T is constructed, a by-product of the construction algorithm is the monodromy matrix Φ given by:

$$\Phi = \frac{\partial x(1; \underline{x}_o)}{\partial \underline{x}_o} \quad (5.55)$$

The location of the eigenvalues of the monodromy matrix determines the stability of the periodic solution. If the eigenvalues of the monodromy matrix are inside the unit circle, the periodic solution is stable. As the control parameter R_f is varied, the eigenvalues of Φ move in the complex plane and may exit the unit circle in one of three ways as shown in Figure 5.26.

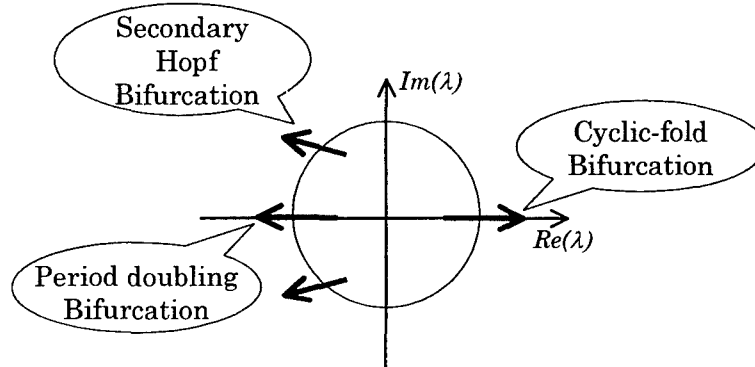


Figure 5.26. Bifurcation of Periodic Solutions

For the DC-DC buck converter with input filter, the eigenvalues of the monodromy matrix leave the unit circle through the $(1, 0)$ point. The system suffers a cyclic-fold bifurcation wherein a stable branch of periodic solutions loses stability and continues as an unstable branch of periodic solutions (Figure 5.25).

Comparison with Linear Analysis

Figure 5.27 illustrates the application of the impedance ratio criterion. It can be seen that, according to Equation (5.3) the system is guaranteed to be stable for $R_f > 0.25$. The linear analysis technique provides information only about system stability as the control parameter is varied. Information regarding the type and multiplicity of solutions as provided by the bifurcation diagram cannot be obtained from linear analysis. Figure 5.28 shows a comparison between the linear and bifurcation analyses results.

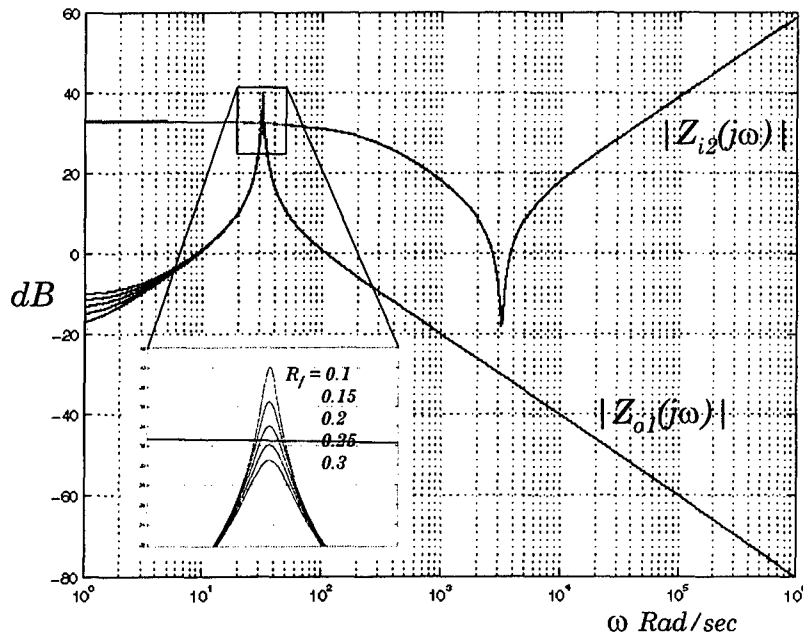


Figure 5.27. Middlebrook Criterion

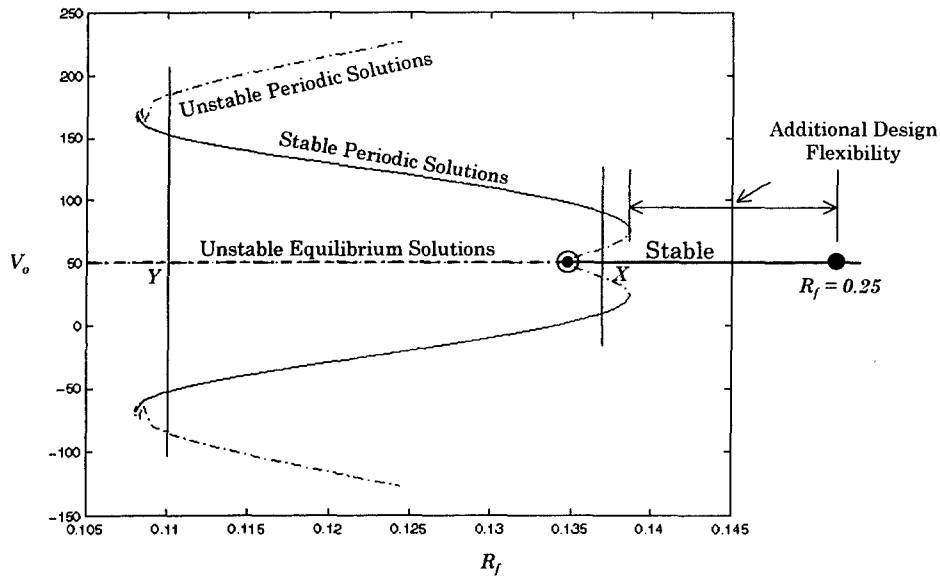


Figure 5.28. Comparison between Linear and Bifurcation Analysis

It is important to note from Figure 5.28 that a stable equilibrium solution (say X) can be perturbed strongly enough to drive the system to a periodic solution. On the other hand, an unstable equilibrium point (say Y) does not lead to catastrophic results when perturbed but only ends up in a stable periodic solution. Such an observation cannot be made from conventional linear analysis methods such as the Middlebrook Impedance Ratio Criterion. In addition, linear analysis provided a conservative estimate of system stability in this case. The Hopf point is at $R_f = 0.138$ where the equilibrium solution loses stability whereas the Middlebrook criterion provides a lower bound of $R_f = 0.25$. A clearer

understanding of the system aided by the use of nonlinear analysis methods can hence help in newer design rules, control laws that optimize performance, cost, size and reliability.

5.3.2. Interaction at the DC Bus

The interaction at the DC bus, shown in Figure 5.29, between the bus regulator and a load converter is discussed in this section. The load subsystem represented by Subsystem 2 in Figure 5.29 is a regulated DC-DC converter with a front-end input filter. The other loads on the DC bus are modeled by a current source, negative impedance (other regulated power converters) or a simple resistance.

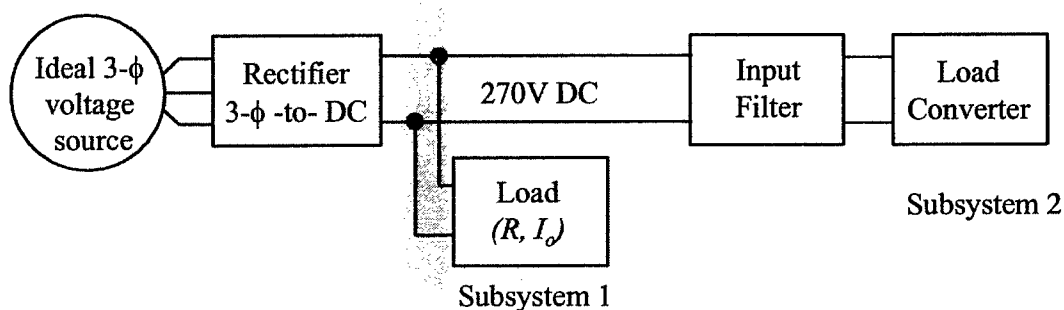


Figure 5.29. Simplified Power System Architecture

The three-phase boost rectifier is represented by its average model in rotating dq -coordinates synchronized with the input line voltages [26]. The load converter is also represented by its corresponding average model.

Stability Analysis

The circuit schematic of the simplified power system is shown in Figure 5.30.

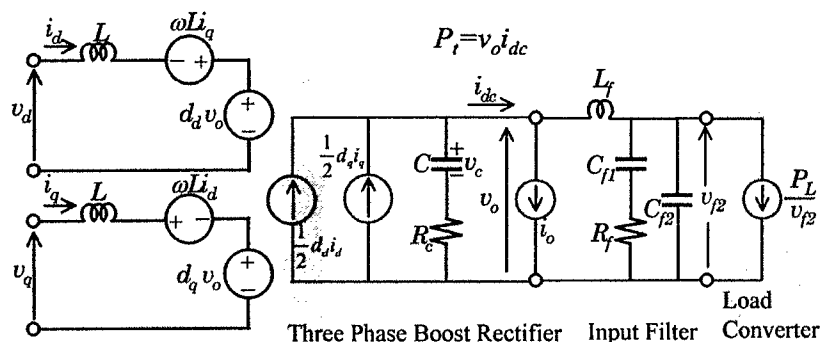


Figure 5.30. Circuit Schematic of Simplified Power System

The total power supplied by the boost rectifier is given by $P_t = v_o i_{dc}$ (Figure 5.30). The DC-DC converter in subsystem 2 is represented by a constant power load with the same

modifications as in [28]. The input filter is a two-stage configuration with the damping resistance in a shunt path to minimize the power loss.

The first step in the analysis of the baseline system is the determination of the control parameter(s) for the bifurcation analysis. The three-phase boost rectifier feeds the DC distribution bus of the baseline power system with a stiff regulated voltage of 270V. A control block diagram of the three-phase boost rectifier is shown in Figure 5.31.

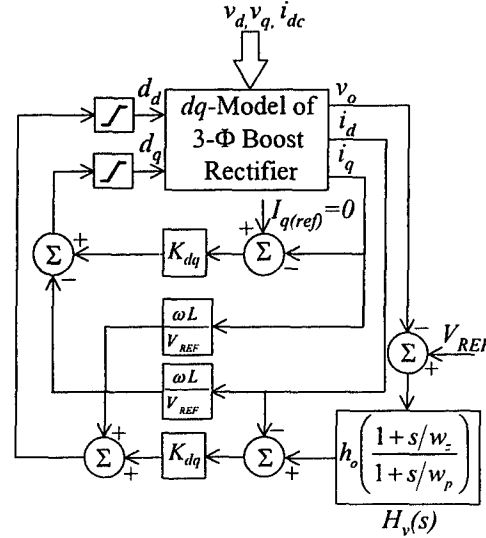


Figure 5.31. Control block diagram of three-phase boost rectifier

One of the critical performance indices of the rectifier is its bandwidth of regulation. This parameter can be related to the transient response and disturbance rejection properties of the rectifier. In addition, the bandwidth is intimately related to the stability of the rectifier and hence of the baseline system. The gain h_o of the voltage controller $H_v(s)$ (Figure 5.31) is directly related to the bandwidth of the rectifier and hence is chosen as the control parameter for the bifurcation analysis of the baseline system. The stability analysis proceeds as follows: The stability of the equilibrium solutions of the baseline system is determined as a function of the control parameter, h_o . The total power P_t , supplied by the boost rectifier is divided equally between the constant current load i_o , and the constant power load P_L/v_{f2} . The complete bifurcation diagram for the baseline system for $P_t=8kW$ is shown in Figure 5.32a.

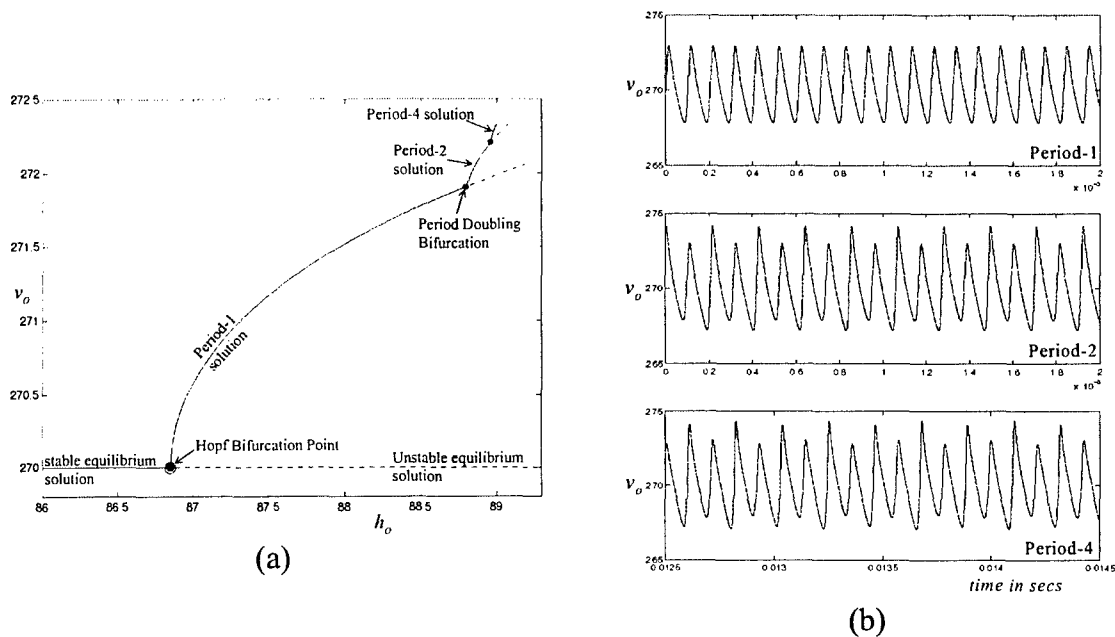


Figure 5.32. (a) Bifurcation Diagram of Baseline System as a function of h_o for $P_t=8kW$
 (b) Periodic Solutions of Baseline System

The equilibrium point loses stability through a Hopf bifurcation at $h_o=86.8295$ for $P_t=8kW$. The normal form equations (Equation (5.43)) of the system at the Hopf point indicate that the bifurcation is supercritical (i.e.) the bifurcating periodic solutions are stable as shown in Figure 5.32a. The branch of periodic solutions is followed using the pseudo-arc length continuation procedure described in the previous section. The stability of the constructed periodic solutions is monitored by observing the corresponding Floquet multipliers. As mentioned in the previous section, the Floquet multipliers move in the complex plane as a function of the control parameter and may exit the unit circle in one of three ways as shown in Figure 5.43. A period doubling bifurcation occurs at $h_o=88.7904$ where, one Floquet multiplier exits the unit circle through $(-1,0)$. This is followed by another period doubling bifurcation to a period-4 solution. These periodic solutions are shown in Figure 5.32b.

Dependence on Parameter Values

The baseline system considered in this paper consists of two interconnected nonlinear subsystems namely, the three-phase boost rectifier and the regulated load converter with input filter. The analysis method presented above considers the stability of the baseline system as a whole, regardless of the stability of the individual subsystems. To this end, as the control parameter is varied, the stability of the three phase boost rectifier as a standalone system terminated by the load P_t , is determined, in addition to that of the baseline system. The parameter values that yield the results shown in Figure 5.32 are such that, the equilibrium point of the boost rectifier as a standalone system loses its stability before that of the baseline system (i.e.) for $h_o < 86.8295$. Such a situation is only of academic interest as it defeats the entire purpose of subsystem integration in that an unstable system (the boost rectifier) is integrated with a stable system (the filter-load

converter subsystem) to form the stable baseline system. However, a different set of parameter values can result in an unstable baseline system while preserving the stability of the individual subsystems. It is the parameters of the boost rectifier that determine the manner in which the baseline system loses stability.

Since the load on the DC bus is not constant at all times, the rectifier should provide “good” regulation of the DC bus voltage at all load levels. Since the baseline system is essentially nonlinear, the bandwidth of the regulator can be expected to change significantly with the load. Hence, it becomes important to study the effect of the regulation bandwidth of the rectifier on the stability of the baseline system for different values of power P_i . The values of h_o for which the baseline system loses stability were determined for different values of power P_i . For each value of P_i , the type of the Hopf bifurcation was determined by obtaining the normal form equations of the baseline system. The values of α_2 in the normal form equations are given in Table 5.1 for different values of power P_i .

Table 5.1. α_2 for Case 1 and Case 2.

P_i (kW)	Case 1		Case 2	
	α_2	$h_o(\text{hopf})$	$\alpha_2(10^6)$	$h_o(\text{hopf})$
8	-0.01213	86.8295	26.9384	19.5325
16	-0.00818	45.8968	12.6145	8.5091
24	-0.00733	31.9366	4.6564	5.4051
32	-0.00854	24.6799	-3.0179	4.0491
40	-0.00773	19.9758	-6.4271	3.3109
48	-0.00214	16.5835	4.6585	2.8485
56	0.005724	14.0965	38.5256	2.5291

In Table 5.1, case 1 is identified as the situation where the baseline system preserves its stability in spite of the boost rectifier being unstable, and that wherein the baseline system loses its stability with the individual subsystems being stable is identified as case 2. It can be seen from Table 5.1 that, the type of bifurcation for case 2 changes from subcritical to supercritical and back as the power is increased. Further investigation is necessary to identify the reasons for such a behavior. However, the normal form equations provide an idea about the post-bifurcation behavior of the system, which can be used to design fault-clearing systems in the event of instability. In addition, it can be seen from Table 5.1, that the values of h_o for which the baseline system loses stability, decrease with increasing power. Hence, with the knowledge of the maximum possible load on the DC bus, h_o can be chosen such that the equilibrium solutions are stable at all load power levels or can be adaptively varied as a function of the load for optimal performance of the converter.

5.4 Optimal Parameter Update

The bifurcation analysis results that were obtained in the previous section provide an improved understanding of the global behavior of the system compared to linear analysis techniques, which provide local information. However, they do not lend themselves very easily to incorporation into a design procedure or an optimization problem. In this section, we investigate the applicability of a simple design methodology used in power systems, based on bifurcation analysis, [33,34] to the design of subsystem components in the aircraft power distribution system. It was shown in the last chapter that as the bifurcation parameter was varied, the interconnected systems lose stability through a Hopf bifurcation. A Hopf bifurcation indicates the presence of oscillatory solutions. The stability of these solutions is determined from the normal form equations of the system at the bifurcation point. The design methodology presented in this section deals with the determination of an optimal direction in which the parameters of the system can be varied such that a Hopf bifurcation and hence oscillations of the system can be avoided thus improving the robustness of the nominal design. The potential that this method holds for extension to an optimization formulation is discussed.

5.4.1. Bifurcation Margin

The system used to demonstrate the design methodology is based on that shown in Figure 5.29, however, with considerable simplifications. The 3- Φ to DC boost rectifier is replaced by a DC-DC boost converter and the load on the DC bus is lumped into a single DC current source. A block diagram of this simplified system is shown in Figure 5.33.

The boost converter is represented by its average model for the following analysis. The schematic of the average model of a DC-DC boost converter is shown in Figure 5.34. It can be seen that the duty cycle d , in Figure 5.34 is the duty cycle of the diode and not of the switch.

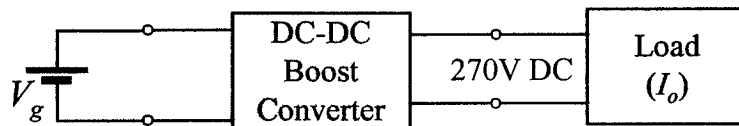


Figure 5.33. System block diagram

The converter is controlled using a multiloop controller consisting of an outer voltage loop and an inner average current loop.

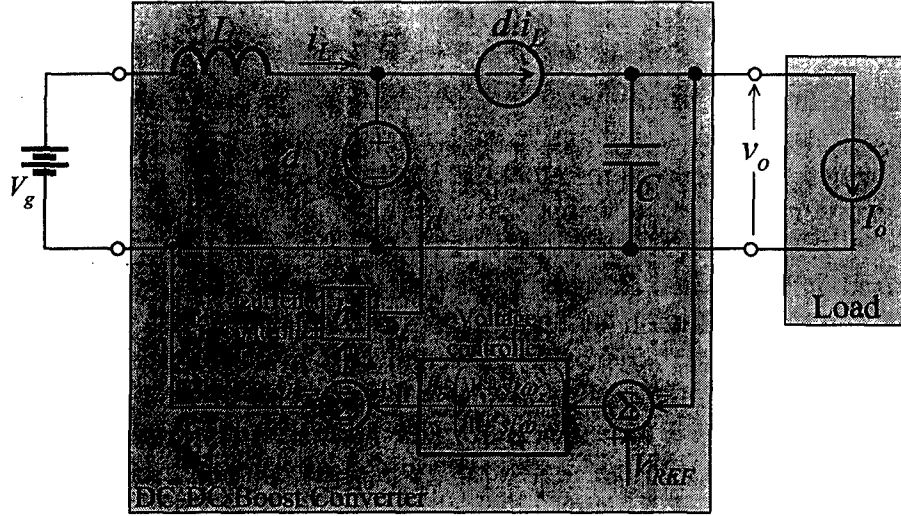


Figure 5.34. Average model of DC-DC boost converter with multiloop controller

The load current I_o is chosen as the bifurcation parameter as a function of which the stability of the system is monitored. The design variables of the system are chosen to be the voltage and current controller gains, namely h_o and h_i respectively. The design variable vector is defined as $p = [h_o \ h_i]$. The remaining parameters of the system are considered fixed in the analysis.

A control parameter vector $\lambda = [I_o, h_o, h_i]$ of the system, consisting of the bifurcation parameter and the design variable vector is defined. At the nominal operating point of the system, the control parameter vector is denoted by $\lambda_{nom} = [I_{o,nom}, h_{o,nom}, h_{i,nom}]$. The system suffers a Hopf bifurcation point at $\lambda_{hopf} = [I_{o,hopf}, h_{o,hopf}, h_{i,hopf}]$, with a simple pair of complex eigenvalues of the linearized system on the imaginary axis. The proximity of the nominal design to the Hopf bifurcation is measured by a bifurcation margin M . The bifurcation margin is defined as the distance between the bifurcation point and the nominal operating point. Hence, M is given by:

$$M = \|\lambda_{hopf} - \lambda_{nom}\|, \quad (5.56)$$

where the distance measure in Equation (5.33) is the conventional Cartesian distance measure [33]. If only the bifurcation parameter I_o is varied with the design variables fixed at their nominal operating values, the bifurcation margin reduces to:

$$M = \|I_{o,hopf} - I_{o,nom}\|. \quad (5.57)$$

The goal of the design methodology is to determine the optimal direction of first order change in the design variable vector p such the bifurcation margin M is increased. The bifurcation margin is regarded as a function of the controller parameter vector and the gradient or the sensitivity $M_{\lambda/\lambda_{nom}}$ of the margin M is computed such that the design may be incrementally improved by changing parameters in the direction $M_{\lambda/\lambda_{nom}}$. The gradient $M_{\lambda/\lambda_{nom}}$ is given by:

$$M_{\lambda/\lambda_{nom}} = \left[\begin{array}{c} \frac{\partial M}{\partial I_o} \\ \frac{\partial M}{\partial h_o} \\ \frac{\partial M}{\partial h_i} \end{array} \right]_{\lambda_{nom}} \quad (5.58)$$

Since the bifurcation parameter I_o cannot be controlled, the optimal direction of change is along the projection of the gradient $M_{\lambda/\lambda_{nom}}$, on the design variable space. This projection $M_{p/p_{nom}}$ is given by:

$$M_{p/p_{nom}} = \left[\begin{array}{c} \frac{\partial M}{\partial h_o} \\ \frac{\partial M}{\partial h_i} \end{array} \right]_{p_{nom}} \quad (5.59)$$

The computation of the gradient $M_{\lambda/\lambda_{nom}}$, and hence the projection $M_{p/p_{nom}}$, is described in the following section.

5.4.2. Computation of the Gradient

The computation of the gradient of the bifurcation margin for the DC-DC boost converter is presented in this section. The nonlinear state equations of the system shown in Figure 5.34 are given below:

$$\dot{x} = \frac{d}{dt} \begin{bmatrix} i_L \\ v_o \\ v_{C1} \\ v_{C2} \end{bmatrix} = f(x, \lambda) = \begin{bmatrix} (v_g - d v_o) \frac{1}{L} \\ (d i_L - I_o) \frac{1}{C} \\ (v_{C2} - v_{C1}) \omega_z \\ [(v_o - V_{REF}) h_o - (v_{C2} - v_{C1})] \omega_p \end{bmatrix}, \quad (5.60)$$

where the duty cycle d is given by:

$$d = (V_{REF} - v_{C2} - i_L) h_i. \quad (5.61)$$

The variables v_{C1} and v_{C2} in Equations (5.60) and (5.61) correspond to the states in the voltage controller.

The Hopf bifurcation hypersurface is determined by the vanishing real parts of the eigenvalues of the linearized system. Specifically, Σ^{hopf} is defined as the space of control parameter vectors $\lambda_{hopf} = [I_{o,hopf}, h_{o,hopf}, h_{i,hopf}]$ such that the system described by Equations (5.60) and (5.61) suffers a Hopf bifurcation. That is, with $\lambda = \lambda_{hopf}$ the Jacobian of the system given by:

$$f_x(x, \lambda) = \frac{\partial f}{\partial x} = \begin{bmatrix} h_i \frac{v_o}{L} & -h_i \frac{(V_{REF} - v_{C2} - i_L)}{L} & 0 & h_i \frac{v_o}{L} \\ h_i \frac{(V_{REF} - v_{C2} - 2i_L)}{C} & 0 & 0 & -h_i \frac{i_L}{C} \\ 0 & 0 & -\omega_z & \omega_z \\ 0 & h_o \omega_p & \omega_p & -\omega_p \end{bmatrix}, \quad (5.62)$$

when evaluated at the equilibrium solution $(x_{hopf}, \lambda_{hopf})$ has a simple pair of eigenvalues $\pm j\omega_{hopf}$, and all other eigenvalues with nonzero real parts. The bifurcation hypersurface for the system under consideration is the load current $I_{o,hopf}$ for which the system undergoes a Hopf bifurcation plotted as a function of the design variables h_o and h_i as shown in Figure 5.35.

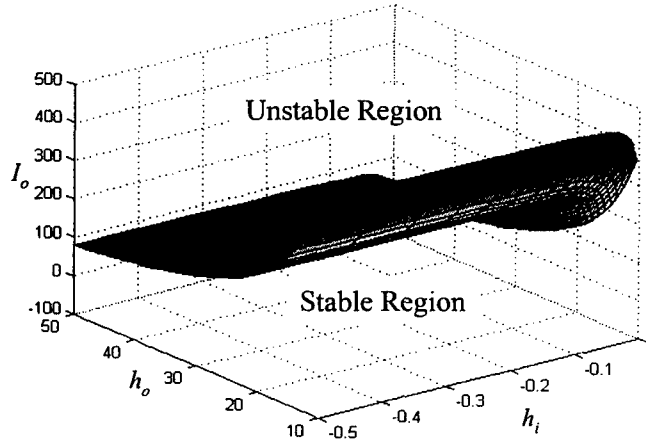


Figure 5.35. The Hopf bifurcation hypersurface

It is shown in [33] that the gradient $M_{\lambda/\lambda_{nom}}$ given by Equation (5.58), is essentially a function of the normal vector to the Hopf bifurcation hypersurface Σ^{hopf} . The normal vector, in turn is given by the sensitivity or the gradient of the real part of the eigenvalues of the linearized system with respect to the control parameter vector λ at the bifurcation point as given by:

$$N(\lambda_{hopf}) = \left. \frac{d}{d\lambda} [\text{Re}(\mu(\lambda))] \right|_{\lambda_{hopf}}, \quad (5.63)$$

where, $\mu(\lambda)$ represents the simple pair of complex eigenvalues whose real part goes to zero at $\lambda = \lambda_{hopf}$. The determination of the normal vector is described in the following. To

start with, the equilibrium solutions $\mu(\lambda)$ of the system described by Equations (5.60) and (5.61) are given by:

$$u(\lambda) = \begin{bmatrix} I_L \\ V_o \\ V_{C1} \\ V_{C2} \end{bmatrix} = \begin{bmatrix} I_o \frac{V_{REF}}{V_{dc}} \\ V_{REF} \\ V_{REF} - I_o \frac{V_{REF}}{V_{dc}} - \frac{V_{dc}}{V_{REF}} \frac{1}{h_i} \\ V_{REF} - I_o \frac{V_{REF}}{V_{dc}} - \frac{V_{dc}}{V_{REF}} \frac{1}{h_i} \end{bmatrix}. \quad (5.64)$$

Let the right and left eigenvectors of the Jacobian given by Equation (5.62), corresponding to $\mu(\lambda)$ be denoted by $w^T(\lambda)$ and $v(\lambda)$ respectively. The eigenvectors are normalized according to $|v(\lambda)|=1$ and $w^T(\lambda)v(\lambda)=1$. Using this normalization, it can be easily shown that:

$$\mu(\lambda) = w^T(\lambda) f_x(u(\lambda), \lambda) v(\lambda). \quad (5.65)$$

Differentiating $\mu(\lambda)$ with respect to the control parameter vector λ ,

$$\begin{aligned} \frac{d}{d\lambda} [\mu(\lambda)] &= \frac{d}{d\lambda} [w^T f_x(u, \lambda) v] \\ &= w^T \frac{d}{d\lambda} (f_x(u, \lambda)) v + \frac{d}{d\lambda} (w^T) f_x(u, \lambda) v + w^T f_x(u, \lambda) \frac{d}{d\lambda} (v) \\ &= w^T \frac{d}{d\lambda} (f_x(u, \lambda)) v + \mu \frac{d}{d\lambda} (w^T v) \\ &= w^T \frac{d}{d\lambda} (f_x(u, \lambda)) v. \end{aligned} \quad (5.66)$$

The dependence on λ of the variables in Equations (5.66) is intentionally omitted to avoid notational clutter. Taking the real part of Equation (5.66) and using

$$\frac{d}{d\lambda} [\text{Re}(\mu(\lambda))] \Big|_{\lambda_{hopf}} = \text{Re} \left[\frac{d}{d\lambda} (\mu(\lambda)) \right] \Big|_{\lambda_{hopf}}, \quad (5.67)$$

the normal vector to the hypersurface, according to Equation (5.63), is obtained as:

$$N(\lambda_{hopf}) = \text{Re} \left[w^T(\lambda) \frac{d}{d\lambda} (f_x(u(\lambda), \lambda)) v(\lambda) \right] \Big|_{\lambda_{hopf}}. \quad (5.68)$$

Expanding the derivative of the Jacobian with respect to the control parameter in Equation (5.68), the normal vector is given by:

$$N(\lambda_{hopf}) = \begin{bmatrix} n_{I_o} \\ n_{h_o} \\ n_{h_i} \end{bmatrix} = \text{Re} \begin{bmatrix} w^T(\lambda) \left[\frac{d}{dI_o} (f_x(u(\lambda), \lambda)) \right] v(\lambda) \\ w^T(\lambda) \left[\frac{d}{dh_o} (f_x(u(\lambda), \lambda)) \right] v(\lambda) \\ w^T(\lambda) \left[\frac{d}{dh_i} (f_x(u(\lambda), \lambda)) \right] v(\lambda) \end{bmatrix}_{\lambda_{hopf}} \quad (5.69)$$

The partial derivatives in Equation (5.69) are given by:

$$\frac{d}{dI_o} (f_x(u(\lambda), \lambda)) = \begin{bmatrix} 0 & 0 & 0 & 0 \\ -\frac{1}{C} \frac{h_i V_{REF}}{V_g} & 0 & 0 & -\frac{1}{C} \frac{h_i V_{REF}}{V_g} \\ 0 & 0 & 0 & 0 \\ 0 & 0 & 0 & 0 \end{bmatrix} \quad (5.70a)$$

$$\frac{d}{dh_o} (f_x(u(\lambda), \lambda)) = \begin{bmatrix} 0 & 0 & 0 & 0 \\ 0 & 0 & 0 & 0 \\ 0 & 0 & 0 & 0 \\ 0 & \omega_p & 0 & 0 \end{bmatrix} \quad (5.70b)$$

$$\frac{d}{dh_i} (f_x(u(\lambda), \lambda)) = \begin{bmatrix} \frac{V_{REF}}{L} & 0 & 0 & \frac{V_{REF}}{L} \\ -\frac{1}{C} \frac{I_o V_{REF}}{V_g} & 0 & 0 & -\frac{1}{C} \frac{I_o V_{REF}}{V_g} \\ 0 & 0 & 0 & 0 \\ 0 & 0 & 0 & 0 \end{bmatrix} \quad (5.70c)$$

According to [33], the gradient $M_{\lambda/\lambda_{nom}}$ of the bifurcation margin (Equation (5.57)) with respect to the control parameter vector λ is given by:

$$M_{\lambda/\lambda_{nom}} = - \left(N(\lambda_{hopf})^T \begin{bmatrix} 1 \\ 0 \\ 0 \end{bmatrix} \right)^{-1} N(\lambda_{hopf}) = - \frac{1}{n_{I_o}} \begin{bmatrix} n_{I_o} \\ n_{h_o} \\ n_{h_i} \end{bmatrix} \quad (5.71)$$

The geometric interpretation of Equation (5.71) is that the optimum direction to increase the distance with respect to the bifurcation parameter, namely I_o of a nominal design point λ_{nom} to the bifurcation hypersurface is antiparallel to the outward normal to the

hypersurface. Hence, the optimum direction to vary the design variable vector is along the projection of the gradient given by Equation (5.71) on the design variable space. This projection can be obtained as:

$$M_{p/p_o} = -\left(\frac{1}{n_{I_o}}\right) \begin{bmatrix} n_{h_o} \\ n_{h_i} \end{bmatrix}. \quad (5.72)$$

5.4.3. Simulation Results

Simulation results of the DC-DC boost converter are presented in this section to demonstrate the proposed design methodology. Specifically, a nominal design is taken through a fixed number of design iterations to illustrate the incremental improvement in the design. The nominal operating condition is specified in terms of the nominal load current $I_{o,nom}$, and nominal design variable vector $p_{nom} = [h_{o,nom} \ h_{i,nom}]$. The nominal control parameter vector is hence, given by $\lambda_{nom} = [I_{o,nom} \ h_{o,nom} \ h_{i,nom}]$. The remaining variables in the converter are assumed fixed throughout the design process. For the given design variable vector p_{nom} , the load current $I_{o,hopf}$, for which the system suffers a Hopf bifurcation is determined from the bifurcation hypersurface shown in Figure 5.35. The corresponding control parameter vector on the bifurcation hypersurface is then $\lambda_{hopf} = [I_{o,hopf} \ h_{o,nom} \ h_{i,nom}]$. The projection of the normal vector to the hypersurface at λ_{hopf} , on the design variable space is determined from Equation (5.72). The nominal design is then incrementally improved by modifying the design variable vector $p_{nom} = [h_{o,nom} \ h_{i,nom}]$ along the projection. Figure 5.36 shows the optimal trajectory of the design variable vector from a given nominal design.

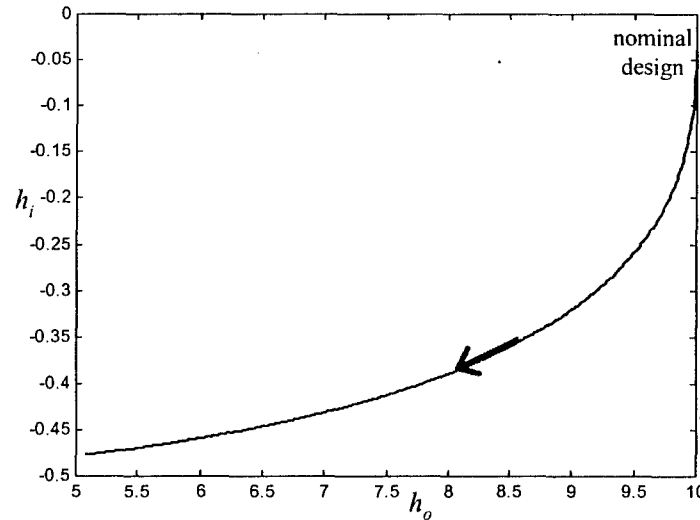


Figure 5.36. Optimal trajectory of design variable vector

At each point on the trajectory, the control parameter vector on the bifurcation hypersurface is determined. The projection on the design variable space, given by

Equation (5.72), of the normal vector to the bifurcation hypersurface at the control parameter vector is determined. The new design variable vector is then determined by modifying the previous vector, by an incremental magnitude, in the direction of the projection. The optimal trajectory informs the designer as to which of the parameters in the design variable vector, the stability of the system is more sensitive to. The direction of the arrow indicates the direction in which the design variables are modified. From Figure 5.36, it can be seen that the variation in h_i is greater than that of h_o initially. The phase margin of the linearized system is determined at each design point and is plotted in Figure 5.37 to illustrate that the robustness of the linearized system improves along the trajectory.

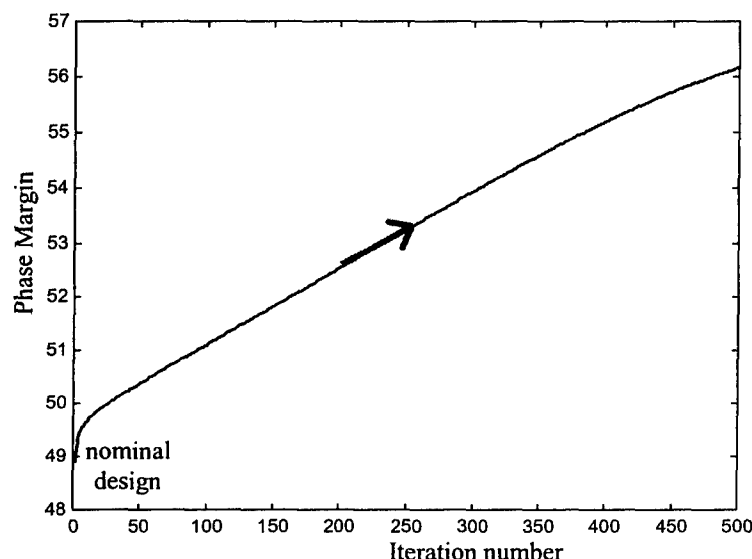


Figure 5.37. Phase Margin of linearized system

6. Optimization of a Thyristor Assembly

In this section, the work performed by one of our industry partners (BAE Systems, Johnson City, NY) in applying optimization methodologies to the design of a thyristor assembly for pulsed power applications is described.

The requirements associated with developing more electric aircraft and associated electric weapons systems tax the capabilities of current power generation, distribution and control technologies. New technologies are being developed to meet the ever-increasing demands on the power system. To achieve the required performance goals of an airborne electrical weapons system, the designer must consider all the limits of its operation. Size and weight must be limited to fit in a conventional size vehicle. Electrical efficiency and heat dissipation must be optimized to maximize firing rate. Structural strength must be maximized to accommodate the large Lorenz forces that are imparted on the weapons system components.

An important element in the design of these systems will be the effective balancing of design variables to achieve an optimum solution. The work reported in this section represents a first step towards the development of a cost effective tool for this purpose.

6.1 Thyristor Assembly

A thyristor assembly for pulsed power applications was selected as an example problem to test and demonstrate the optimization technologies. Power demands from electrical weapons systems require switch assemblies that can control very high peak currents, but these assemblies are large and add to aircraft weight. The design must be optimized to minimize size and/or weight, while constraining inductance, power dissipation, current density, junction temperature, Lorentz forces and other performance parameters.

The thyristor assembly studied in this section is illustrated in Figures 6.1 through 6.3. The assembly consists of 4 parallel stacks of 4 thyristors in series.

- Item AA is a 125 *mm* diameter thyristor stack that is equally spaced and repeated 4 times around the center of the assembly.
- Item BB is an aluminum disk that provides an electrical path through the tops of each thyristor. This disk conducts current from a raised area at its inner diameter to the thyristor stacks. The disk also contributes to mechanical support of the assembly.
- Item CC is a hollow aluminum tube that makes electrical contact with the bottom base plate FF. This tube conducts return current from the bottoms of the thyristors stacks and aids in field cancellation.
- Item DD is a 125 *mm* diameter aluminum disk that is placed between the top of a thyristor stack and the top base plate BB. Item DD is repeated 4 times. Current flows into the assembly at the raised area on the inner diameter of top disk BB. Current will tend to crowd to the inside of each thyristor, because it wants to flow along the path of lowest resistance. Item DD is intend to help minimize the current density gradient across the thyristor stacks by allowing the current to spread before it enters a stack. Alternatively, top disk BB could be made thicker to allow the entering current to spread, but this would result in a thicker and heavier disk.
- Item EE performs the same function as item DD, but item EE is placed between the bottom of each thyristor stack and the bottom base plate FF. As current exits a thyristor stack, it must flow towards the center return tube. This could cause excessive current crowding in the stack near the thyristor exit area. Item EE should help spread the current.
- Item FF is an aluminum disk that provides an electrical path through the bottoms of each thyristor. This disk conducts current form the bottoms of each thyristor stack to

the center return tube. The disk also contributes to mechanical support of the assembly.

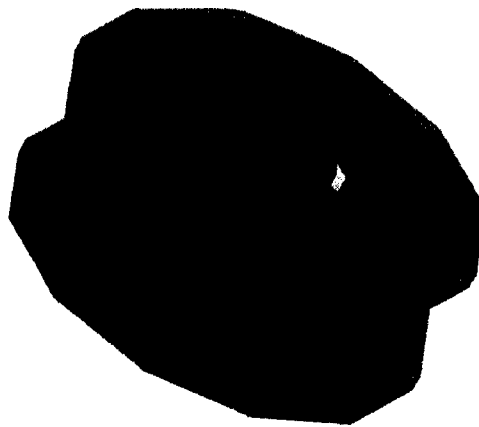


Figure 6.1. Thyristor Assembly

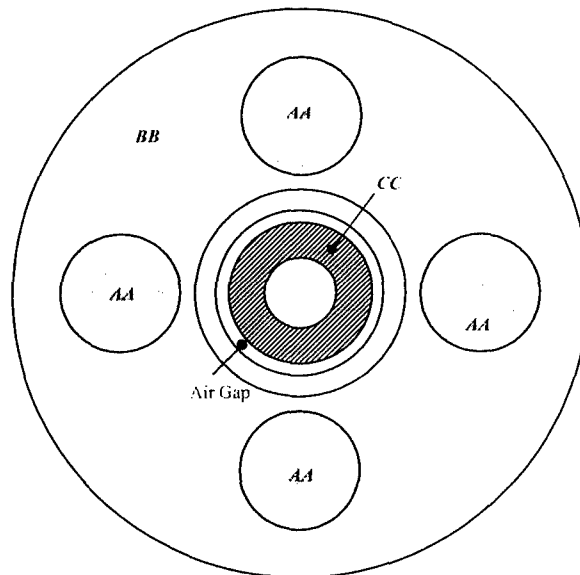


Figure 6.2. Top View of Thyristor Assembly

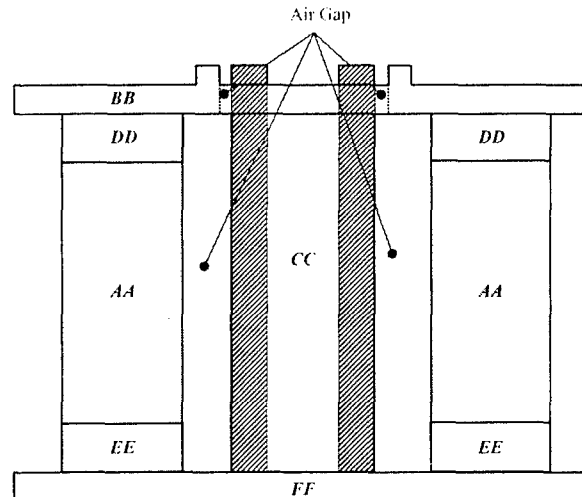


Figure 6.3. Side View of Thyristor Assembly

6.2 Simulation

The electrical performance of the thyristor assembly was simulated using Ansoft Maxwell 3D. The input current in a real application is a pulse of current that lasts for an unspecified number of milliseconds. Simulating a pulse of this type would require a large number of Fourier components to accurately represent the pulse. The resulting simulation would be computationally intensive and impractical in a design environment. As a compromise, an eddy current analysis was run on a single high frequency current waveform. The current source for the analyses is given in Table 6.1 and is applied at the raised inner boundary of the top disk BB. A second current source is applied at the center return leg (item CC). This has the same magnitude as the first current source, but is opposite in polarity to indicate a current that is exiting the assembly.

Table 6.1. Current Source

Symbol	Magnitude (A)	Frequency (kHz)
I_{DC}	40,000A	0
I_{AC}	40,000A	100kHz

The thermal performance of the thyristor assembly was simulated using a thermal model of the thyristor stack developed using Orcad PSPICE. This model is illustrated in Figure 6.4.

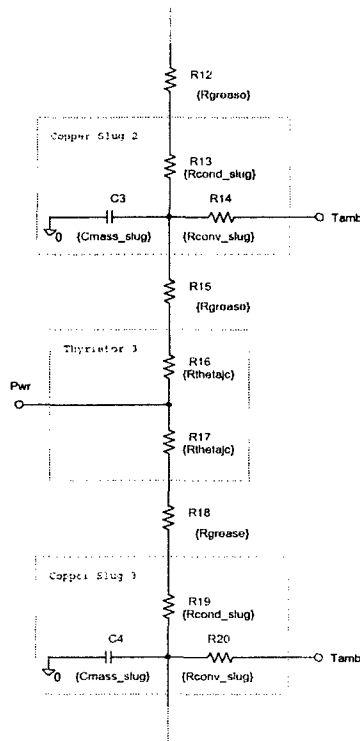


Figure 6.4. PSPICE Thermal Model of Thyristor Stack

6.3 Optimization Formulation

6.3.1. Design Variables

The six design variables used for this study are illustrated in Figure 6.5. Variables B, C, X, and Y control the relative radial positions of the thyristor stacks, the center cylinder, and the air gap. Variables E and F control the thickness of the disks, and the thyristor stack to disk offset distance, respectively. During the optimization process, these variables were allowed to vary continuously between upper and lower bounds.

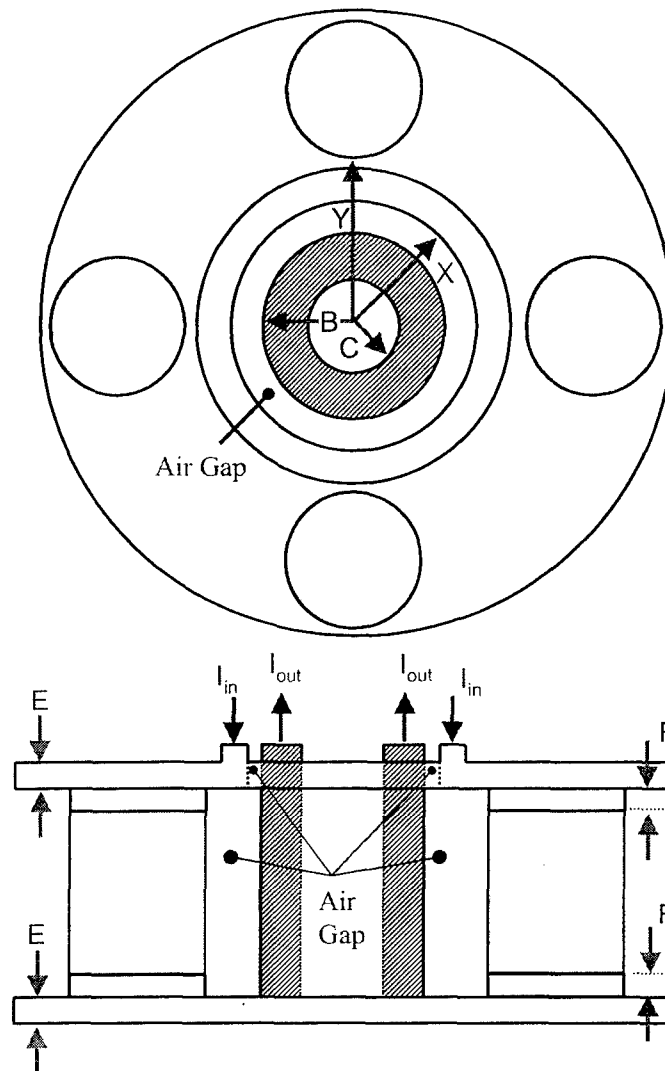


Figure 6.5. Thyristor Assembly Design Variables

6.3.2. Fixed Parameters

Fixed parameters of the system are given in Table 6.2.

- The thyristor diameter T is fixed by the choice of device.
- The width of the raised area N for the current entry is fixed partly by a consideration of the interface to the source of the current.
- There are four (4) thyristors in each stack. Each thyristor is 0.885 in (22.48 mm) thick.
- The thyristor resistivity R_T is an average value calculated from the individual resistivity of the materials in each thyristor. It is assumed that the thyristors are in the conducting state. (Note that conductivity is the reciprocal of resistivity.)

- The power disk, return disk and center return resistivity R_{Al} is a typical value for aluminum. This is also true of the density D_{Al} for the power disk, return disk and center return.

Table 6.2. Fixed Parameters

Symbol	Value	Description
T	125 mm	Thyristor Diameter
N	15 mm	Width of Raised Area for Current Input
K	89.92 mm	Thyristor Stack Height
R_T	9.712 m Ω -cm	Thyristor Resistivity
R_{Al}	3.8 $\mu\Omega$ -cm	Power and Return Disks and Center Return Resistivity (68°F)
D_{Al}	2.713 gm/cm ³	Power and Return Disks and Center Return Density

6.3.3. Constraints

In the initial phase of the study, constraints were imposed to assure physically meaningful dimensions, to limit the inductance, and to limit the power loss. Ansoft Maxwell was used to evaluate the inductance, power loss, and current density for each design. In the second phase of the research, an additional constraint was added to limit the junction temperature of the thyristor stacks. Orcad PSPICE was used to evaluate the junction temperature.

Physical Constraints

Physical constraints are imposed that assure that the final design is physically meaningful and to account for factors (such as the structural strength) that are not accounted for by the Ansoft and PSPICE simulations. The physical constraints imposed for this study are as presented in Table 6.3.

Table 6.3. Physical Constraints

Symbol	Description
Y-B > 20 mm	Thyristor to Center Return Separation
X-B > 20 mm	Top Disk to Center Return Separation
E > 15 mm	Power and Return Disk Thickness

The thyristor to center return separation bound is determined by the need to prevent arcing from the high voltage between the thyristors and the center return, when the thyristors are in the off state. The top disk to center return separation bound is required

for the same reason. The power disk thickness and return disk thickness bounds are determined from a consideration of structural requirements to prevent the assembly from failing under the forces generated during a current pulse. A certain minimum thickness is also required to maintain the thyristors under the required compression.

Power Dissipation

A constraint is imposed that limits the maximum power loss of the assembly to 750 W. Power dissipation in the top and bottom disks and the center return is found under static (DC) and dynamic (AC) conditions using the current sources in Table 6.1. Since the thyristor geometry is fixed, it can be ignored in the calculation. The total power dissipation is computed by summing the power losses from both the DC and AC boundary conditions.

Inductance

The inductance value, L , is an important parameter of the system, as it will influence the rate of rise of the current pulse. In the current work, L is limited to Self-inductance of the entire assembly is found under both static (DC) and dynamic (AC) conditions using the current sources in Table 6.1. Both the DC and AC inductance values were constrained to a maximum value of 18 nH.

Current Density

Current density through the thyristors is found under both static (DC) and dynamic (AC) conditions using the current sources in Table 6.1. Both the DC and AC current density values will be constrained by $\Delta J_{\max} = 0.896 \text{ A/mm}^3$.

Junction Temperature

The junction temperature of the thyristor stack was limited to 110 degrees C when applying the current sources in Table 6.1.

6.3.4. Objective Function

The objective of the optimization is to minimize the volume of the thyristor assembly. The volume is computed using Ansoft Maxwell.

6.4 Optimization Algorithm

The optimization was performed using an Evolutionary Strategies (ES) algorithm developed by BAE Systems. This algorithm mimics the process of evolution for developing optimum solutions to difficult problems. The algorithm utilizes a population of solutions that compete against each other. The fittest individuals survive to create new individuals and improve the overall strength of the population.

ES codes each individual solution with a vector, X , (object parameters) that are used to directly evaluate a solution. Associated with the object parameter vector is a strategy parameter vector, s , that stores the mutation size for each entry in X . The strategy parameters store information on the direction and size of changes to X that produce a high probability of improvements in the overall solution. Strategy parameters help to speed of convergence in ES.

The ES process usually starts with a randomly initialized population. The fitness of each individual in the population is evaluated and they are ranked based on fitness. Multiple new children are created by combining two parents selected randomly from a pre-specified number of the best individuals (m). The new offspring are mutated based on the strategy parameters and the new population is evaluated. The process repeats for multiple generations. A method is also implemented to seed the population with predefined solutions to help speed convergence.

One of the application specific tasks that must be performed in implementing an ES based optimization algorithm is to select an appropriate fitness function. The fitness function must be carefully selected to appropriately define the goals of the solution and to help guide the algorithm to an optimum. In the present problem, the main goal is to minimize the volume of the materials used in the thyristor assembly. The other design goals were implemented as constraints, where each performance parameter was assigned a maximum acceptable value and the weight was artificially inflated when a constraint was exceeded. These additions to the weight function are the constraint penalties.

The first penalty is non-zero if the structure is non-realizable. For example, if the inner radius of a cylinder is larger than the outer radius or if the air gap minimum distance is not satisfied, the structure is not physically meaningful. The penalty for this condition is set to a large value (40,000) to prevent these types of solutions from surviving the evolutionary process. The other performance constraints are set to zero when the constraint is not exceeded or a large value (10,000) if the constraint is exceeded. The penalty is proportional to the magnitude of the constraint violation.

6.5 Software Interface

6.5.1. Direct Interface

Ansoft Maxwell 3D was first connected directly to a software implementation of the ES algorithm using an External Program Interface (Figure 6.6). A graphical user interface allows the user to select the various ES parameters such as population size, number of offspring per generation, number of generations, etc. This information is used to initialize and control the ES algorithm. Maxwell 3D provides a macro language that can be used to automate the specification and analysis of electro-magnetic systems. To interface between the ES algorithm and Maxwell 3D macros were developed that to read the assembly dimensions from a data file, draw the assembly, and evaluate the assembly

performance. The macros then write the performance constraints to a data file. The C++ external program interface takes the object parameters from the ES algorithm and writes them to a data file that is read from the Maxwell macros. It initiates Maxwell to run an analysis, waits for Maxwell to complete, and reads the results from the Maxwell generated data file. The results of the analysis are then passed back to the ES algorithm.

The optimization problem was then solved with physical and electrical constraints only (no thermal constraints). The ES algorithm required from 500 to 1000 Maxwell simulations to achieve a converged design. Using a 1.0 GHz Pentium III processor, a single Maxwell simulation took from one to three minutes, resulting in a total optimization time of approximately ten hours.

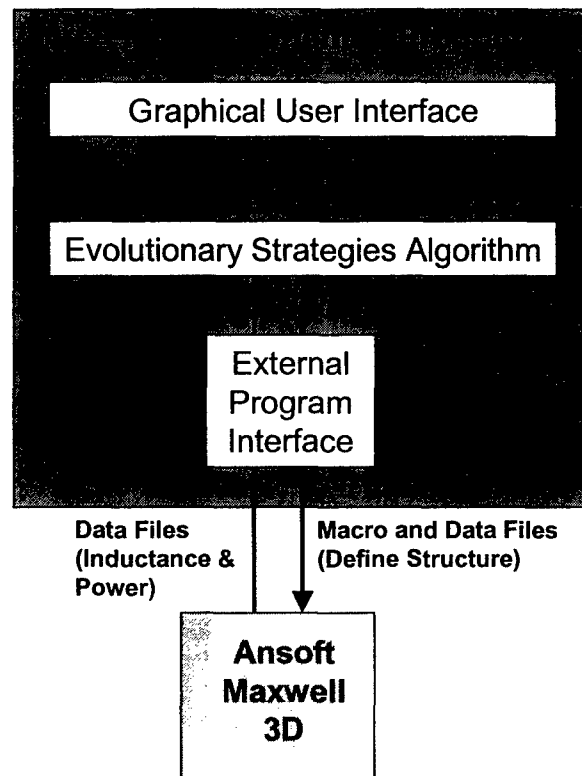


Figure 6.6. Direct Interface

6.5.2. Neural Network Interface

When the ES algorithm is executed, the inputs (geometry parameters) and outputs (inductance, current density, volume, and power dissipation) of the Maxwell 3D simulations are stored to a data file. Using this data, it is possible to create a neural network model of the performance of the thyristor structure.

The neural network uses as inputs the particular geometry parameters of interest and the neural network is trained to produce an output that is equal to the Maxwell simulation outputs. The result of training the network is to capture the information produced by the

Maxwell 3D finite element analysis in a closed form continuous mathematical expression. Figure 6.7 illustrates a neural network with 2 hidden layers and 2 outputs. In actuality (for this problem) some of the parameters only needed one hidden layer. An individual neural network with one output was trained to model each performance parameter of the structure (4 neural networks).

Neural Networks are useful for this (and any other modeling problem) since the neural network is trained using an automated software tool that quickly generates the model from data. The software tool can model simple problems or very difficult problems, the only thing that the user needs to do is experiment with the network size to find a size the works well for a particular problem. The resulting neural network models are then easily implemented by a single object oriented C++ class that loads the neural network definition from a file and evaluates its output.

Once the neural network models were available, the software tool to optimize the structure was modified to use neural network models instead of Ansoft Maxwell 3D (Figure 6.8). Since the neural networks are a compact mathematical algorithm, evaluation of the neural network output for a given input vector is orders of magnitude faster than the Maxwell 3D finite element analysis. Using a 1.0 GHz Pentium III processor, the total optimization time was approximately 10 seconds.

The inclusion of neural networks into the modeling software allows for a practical multidisciplinary optimization tool to be generated. Since neural networks can model almost any system, neural networks can be used to model the electrical, thermal, and structural characteristics of a system design. Integrating neural networks with the optimization algorithm allows the optimization algorithm to simultaneously evaluate the performance of a system design in all the appropriate disciplines (Figure 6.9). During this research, such a system was implemented and demonstrated using the thyristor optimization problem.

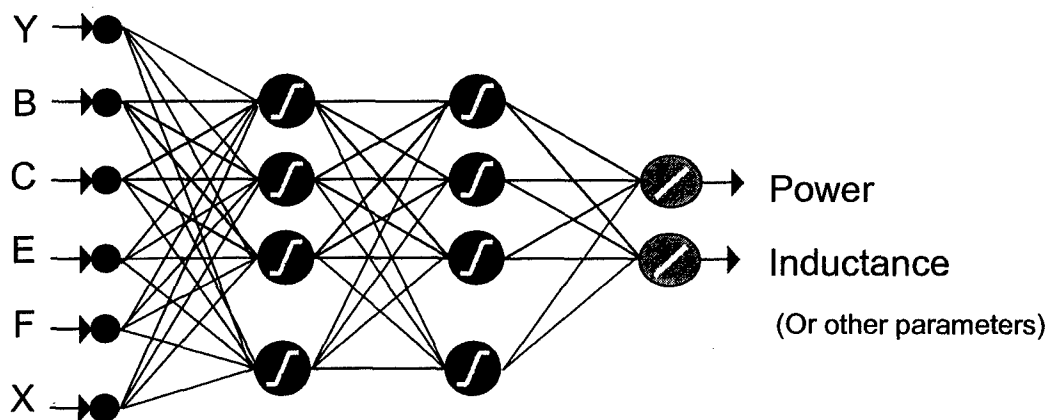


Figure 6.7. Sample Neural Network

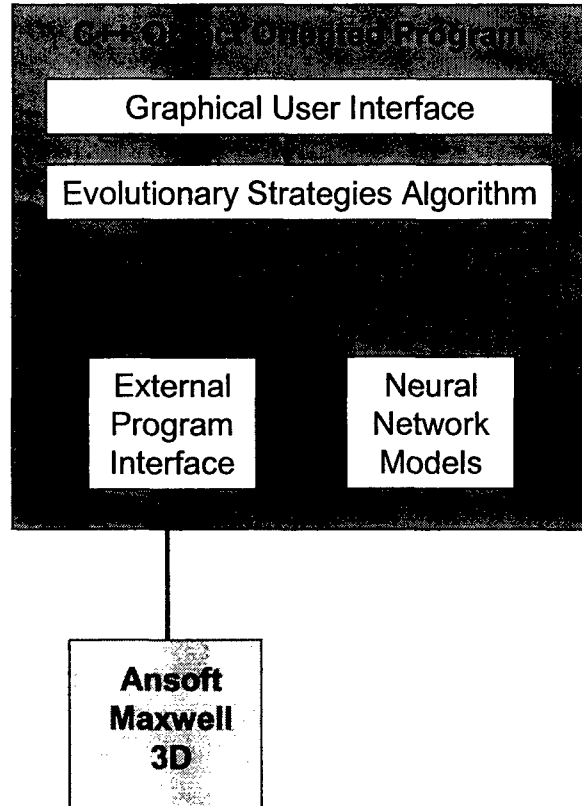


Figure 6.8. Neural Network Interface

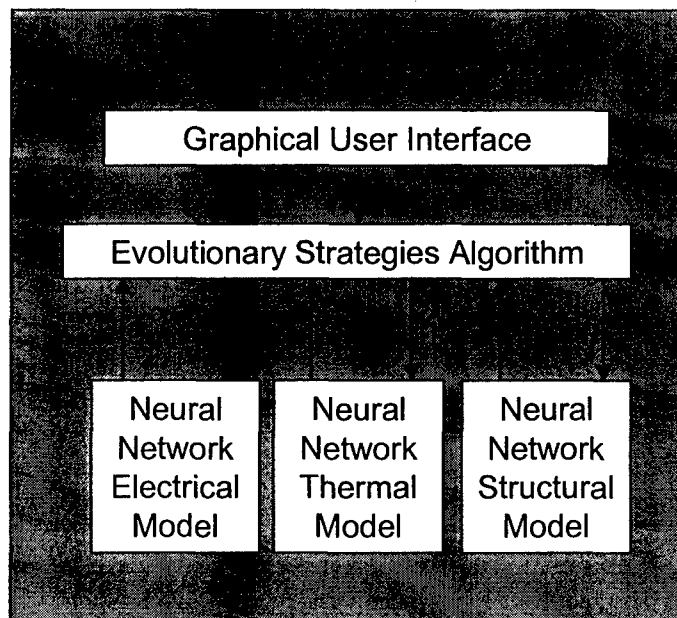


Figure 6.9. Multidisciplinary Neural Network Interface

6.6 Optimization Results

Several sets of results were generated for the thyristor optimization problem using the neural network interface.

6.6.1. Optimization with Electrical Constraints

Results Set 1

Results were first generated using the electrical simulation only (no thermal simulations were used). The optimized volume was 5662 cm^3 . Both the power dissipation constraint and the inductance constraint were active for the final design.

Figures 6.10 and 6.11 illustrate two performance parameters (power dissipation and inductance) of the thyristor assembly. These plots were generated using the neural networks. The blue arrows in the bottom planes indicate the direction of decreasing volume. In the power plot (Figure 6.9), the black line on the bottom plane shows where the power constraint of 750 watts becomes active. The red shaded area is where the power is less than 750 watts. The white dot in the bottom plane shows the optimum point. In the inductance plot (Figure 6.10), the black line on the bottom plane shows where the inductance constraint of 18 nH becomes active. The green shaded area is where the inductance is less than 18 nH . The white dot in the bottom plane shows the optimum point.

These two plots show that the optimization algorithm attempts to find a solution in the direction pointed to by the blue arrow. However it must stay with the red and green shaded areas to meet the performance constraints. The small area near the white dot is the optimum solution at a minimum volume that satisfies the performance constraints. Using plots such as these, an engineer can learn the characteristics of his design from the neural network. The neural networks allow this type of plot to be generated and allow an engineer to test various "what if" scenarios. In the present problem, the power is primarily affected by the thickness of the inner cylinder (B). A thinner inner cylinder leads to higher power dissipation. The inductance is primarily affected by the air gap: the larger the air gap, the larger the inductance.

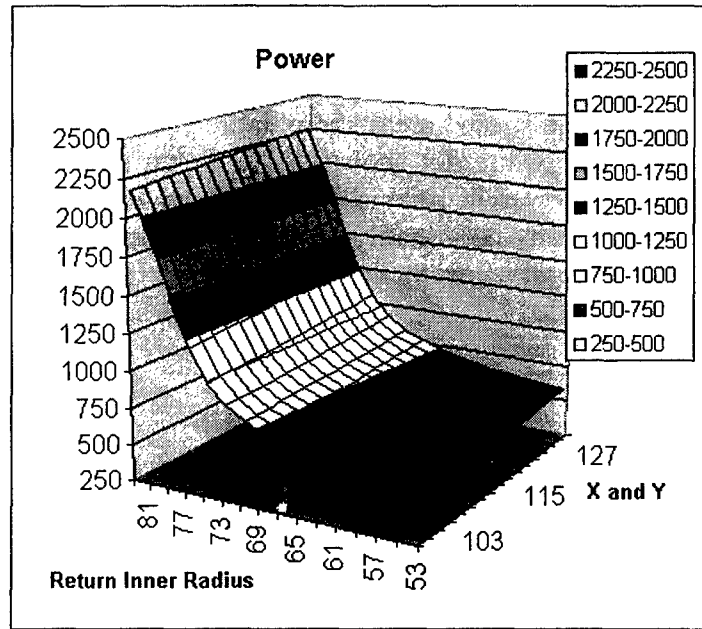


Figure 6.10. Results Set 1 (Power vs. X and Y)

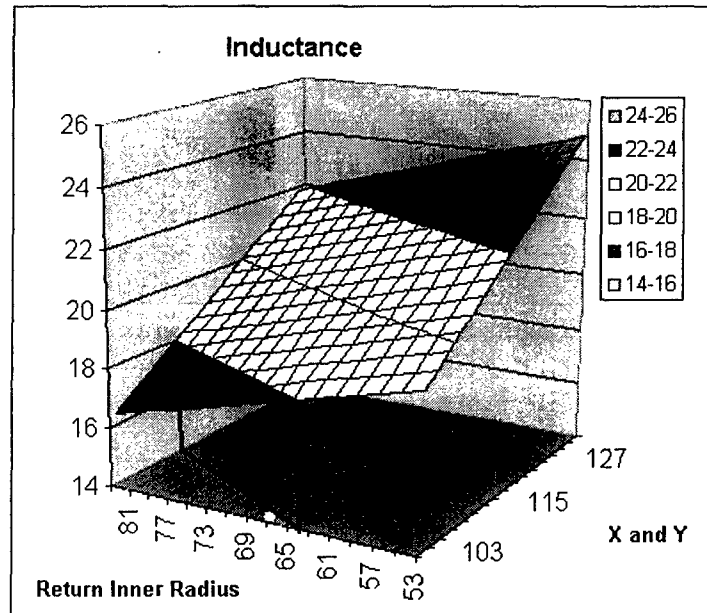


Figure 6.11. Results Set 1 (Inductance vs. X and Y)

Results Set 2

In the previous set of result, the current density constraint was not active. A second optimization test was performed where the thyristor conductivity was increased to make the current density variation more significant. In this run, the current density constraint became active and the inductance constraint became inactive. The optimized volume was 8070 cm^3 .

Figures 6.12 and 6.13 illustrate two performance parameters (power dissipation and current density) for the thyristor assembly. As before, the blue arrow shows the direction of minimizing volume and the shaded areas show the regions in which the performance constraints are satisfied. The white dot shows the optimum solution found by the ES algorithm. As before, the power is primarily affected by the thickness of the inner cylinder (B). The current density is primarily affected by the placement of the thyristors (Y). The further the thyristors are from the inner cylinder the smaller the maximum current density in the thyristors.

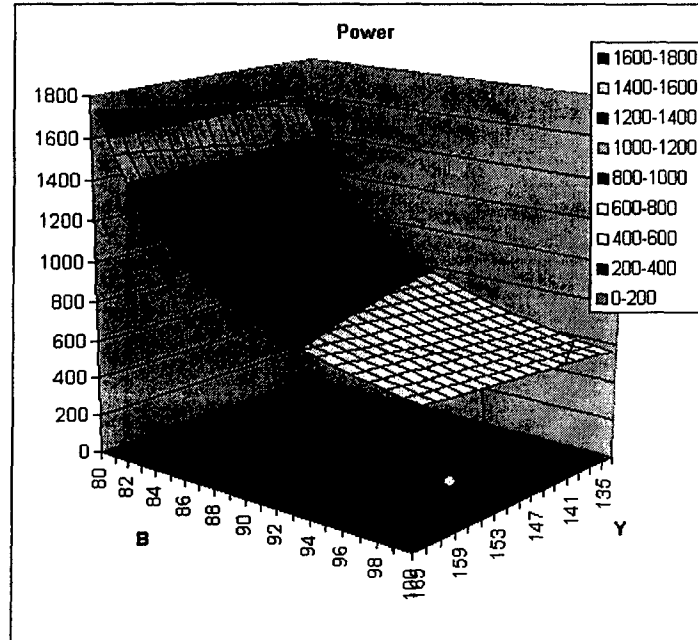


Figure 6.12. Results Set 2 (Power Dissipation vs. B and Y)

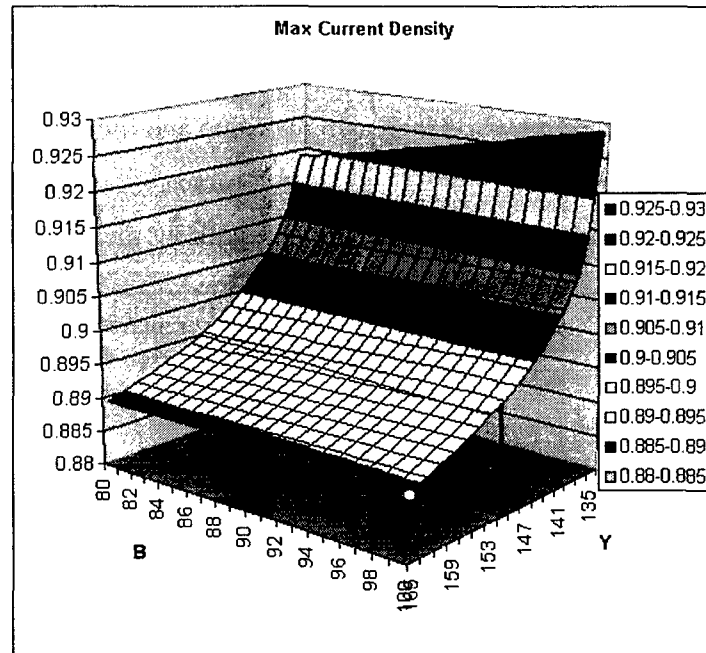


Figure 6.13. Results Set 2 (Current Density vs. B and Y)

Design Tradeoffs

For the present application, it was determined that one of the biggest trade-off that must be made concerns the design of the inner cylinder thickness. For volume and inductance considerations the inner cylinder should be as thin as possible. For power considerations, a thicker inner cylinder is better. An optimum that balances these conflicting constraints is needed. Another major consideration is the placement of the thyristors. The thyristors must be kept as close the center as possible to minimize inductance and volume, but must be kept far enough way so that a minimum air gap can be obtained and an acceptable current density is achieved.

The discs between the thyristors and the top and bottom plates were always set to the minimum thickness by the optimizer. They were added to spread current flow into the thyristor and ended up not being that useful to this end. The usefulness of these disks to the thermal performance of the structure will be in the following section.

6.6.2. Optimization with Thermal and Electrical Constraints

When the thermal model was added to the optimization procedure, the disks between the thyristors and the top and bottom disks became significant. The disks were previously set to the minimum values since they did not affect the electro-magnetic performance of the assembly. However, when the thermal characteristics were considered these disks were increased in thickness from 5 mm to approximately 20 mm in order to dissipate heat. This thickness increase resulted in an increased assembly inductance. The previous constraint of 18 nH could no longer be met and this constraint needed to be relaxed to 25 nH.

The data in the Tables 6.4 and 6.5 show the optimum solutions with and without the thermal model active. When the thermal model is active, the increased dimension (F) reduces the junction temperature while increasing volume and inductance.

Table 6.4. Optimum Solutions with and without thermal model

	Y	B	C	E	F	X
Without Thermal Model	104.0	84.0	70.0	12.7	5.0	104.0
With Thermal Model	100.9	79.8	60.2	12.7	20.3	100.8

Table 6.5. Performance of Optimal Solutions with and without thermal model

	Power (W)	Inductance (nH)	Temperature (°C)	Volume (cm³)
Without Thermal Model	741.8	17.8	266.35	5662
With Thermal Model	749.8	23.57	110.00	7452

6.7 Conclusions

A practical methodology and a generic design tool for implementing multi-disciplinary optimization have been demonstrated. The evolutionary methods that perform the optimization are very robust and can handle noisy, multi-model, non-linear and discontinuous optimization problems. The neural network models can model virtually any system for which a simulation exists.

This technology was demonstrated using the thyristor design application, and several optimum designs were obtained, each corresponding different problem definitions. The technologies were also very helpful in learning more about this particular structure and in visualizing its performance.

One of the main strengths of this approach lies in the power of neural networks. Neural network models used automated training methods that require minimal user time to generate a model. The only thing the user must do is a little experimentation to select an appropriate sized model to match the complexity of the particular problem. Neural networks are easily implemented in software since they have a fixed structure that can be implemented in just a few lines of code.

Simultaneous with the present research, a transient EM modeling capability was being developed at Ansoft. Since the thyristors are mainly used in a transient sense for pulsed power applications, this modeling capability is necessary to truly model their performance characteristics. The current project ended before this new capability became available. It will be important to model the transient capabilities of these thyristor assemblies to produce useful design decisions. The transient thermal model also needs to

be improved to represent a more realistic scenario. The current thermal model was sufficient to demonstrate the basic idea of multi-disciplinary optimization, but a more detailed simulation is needed to develop a true optimal solution.

7. References

1. MIL-STD-704E, Military Standard, *Aircraft Electric Power Characteristics*, May 1, 1991
2. Leonhard Werner, "Control of Electrical Drives", *Springer*, 1997.
3. Wang, K, Chandrasekaran, S., and Cuadros, C., et al., "Quasi-Single Stage Three phase ZVZCS PWM Buck Rectifier", *Virginia Power Electronics Center-Project Report Ericsson submitted to Components*, Sweden, March 1999.
4. J. G. Kassakian, M. F. Schlecht, G. C. Verghese, "Principles of Power Electronics", *Addison-Wesley*, 1991.
5. Middlebrook, R. D., "Input Filter Considerations in Design and Application of Switching Regulators," *IEEE Industry Application Society Annual Meeting*, October 11-14, 1976, Chicago, Il.
6. Ridley R. B., Zhou. C., Lee. F. C., "Application of nonlinear design optimization for power converter components", *IEEE Transactions on Power Electronics*, vol. 5. no. 1., January 1990, pp. 29-39.
7. Vanderplaats, G.N., *Numerical Optimization Techniques for Engineering Design: With Applications*, Vanderplaats R&D Inc., Colorado Springs, CO, 1988.
8. Haftka, R.T., and Gürdal, Z., *Elements of Structural Optimization, Third Revised and Expanded Edition*, Kluwer Academic Publishers, Dordrecht, 1992, pp. 182-186.
9. Ogata. K, "Modern Control Engineering", *Prentice Hall, Eastern Economy Edition*, 1986.
10. Moses, R. W, "Vertical Tail Buffeting Alleviation Using Piezoelectric Actuators-Some Results of the Actively Controlled Response of Buffet-Affected Tails (ACROBAT) program," *Proceedings of SPIE's 4th Annual Symposium on Smart Structures and Materials, Industrial and Commercial Applications of Smart Structures Technologies, Conference 3044*, San Diego, CA, March 4-6, 1997.
11. Smith R.C, and C.L. Hom., "A Domain Wall Model for Ferroelectric Hysteresis", *Proceedings of SPIE, The International Society for Optical Engineering*, Vol.3667, 1999, pp.150-61.
12. Clingman, J. D. "Drive Electronics for large piezoactuators," *Proceeding of SPIE's 1997 North American Symposium on Smart Structures and Materials: Industrial and Commercial Applications of Smart Structures Technologies*, Janet M. Sater; Ed., Vol. 3044, San Diego, CA, March, 1997, pp. 459-467.

13. Clingman. D.J, Gamble. M, "High voltage switching power amplifiers [for helicopter blade actuator]," *Proceedings of the SPIE, The International Society for Optical-Engineering*, vol. 3326, 1998, pp. 472-8.
14. Zvonar, G. A., J. Luan, F. C. Lee, D. K. Lindner, S. Kelly, D. Sable, and T. Schelling, "High-Frequency Switching Amplifiers For Electrostrictive Actuators", *Proceedings of SPIE's 1996 North American Symposium on Smart Structures and Materials: Industrial and Commercial Applications of Smart Structures Technologies*, C. Robert Crowe; Ed., Vol. 2721, San Diego, CA, February, 1996, pp. 465-475.
15. Zvonar, G. A. and D. K. Lindner, "Power Flow Analysis of Electrostrictive Actuators Driven by Switchmode Amplifiers," *Journal on Intelligent Material Systems and Structures*, special issue on the 3rd Annual ARO Workshop on Smart Structures, Vol. 9, 1998, No 3, pp. 210 - 222.
16. Zvonar, G. A. and D. K. Lindner, "Nonlinear Electronic Control of an Electrostrictive Actuator," *Proceeding of SPIE's 1997 North American Symposium on Smart Structures and Materials: Industrial and Commercial Applications of Smart Structures Technologies*, Janet M. Sater; Ed., Vol. 3044, San Diego, CA, March, 1997, pp. 448-458.
17. Main, J. A, Garcia, E, Newton, D. V, "Precision position control of piezoelectric actuators using charge feedback," *Journal of Guidance, Control and Dynamics*, Vol. 18, No. 5, Sep-Oct 1995, pp. 1068-1073.
18. Main JA, Garcia E. "Piezoelectric stack actuators and control system design: strategies and pitfalls". *Journal of Guidance Control & Dynamics*, vol.20, no.3, May-June 1997, pp.479-85.
19. Newton, D. V, Main, J. A, Garcia, E., Massengill,L., "Piezoelectric actuation systems: optimization of driving electronics," *Proceedings of SPIE's 1996 North American Symposium on Smart Structures and Materials: Smart Structures and Integrated Systems*, Vol. 2717, San Diego, CA, February 1996, pp. 259-266.
20. Mohan N., T.M. Undeland, and W. Robbins, "Power Electronics-Converters, Applications and Design", *John Wiley and Sons*, 1995.
21. Warkentin. D. J, Crawley. E.F, "Power flow and amplifier design for piezoelectric actuators in intelligent structures," *Proceedings of the SPIE, The International Society for Optical-Engineering*, vol. 2190, 1994, pp. 283-94.
22. S. Hiti, V. Vlatkovic, D. Borojevic and F. C. Lee, "A New Control Algorithm for Three Phase PWM Buck Rectifier with Input Displacement Factor Compensation", *Proceedings of the 11th VPEC Seminar*, September 1993, pp. 19-25.
23. Mao H, et al., "Novel reduced-order small signal model of three phase PWM rectifiers and its application in control design and system analysis", *Proceedings of the 27th Power Electronics Specialists Conference*, June 1996, vol. 1, pp. 556-562.
24. V. Vlatkovic, D. Borojevic and F. C. Lee, "Input Filter Design for Power Factor Correction Circuits", *Proceedings of the IECON '93*, November 1993, pp.954-958.

25. Mohamed Belkhat, "Stability Criteria for AC power Systems with Regulated Loads", *PhD Dissertation, Department of Electrical and Computer Engineering, Purdue University*, 1997.
26. S. Hiti, D. Borojevic, "Small-signal modeling and control of three-phase PWM converters", *Proceedings of the 15th VPEC Seminar*, 1994, pp. 63-70.
27. Green, Limebeer, "Linear Robust Control", *Prentice Hall Information and System Sciences Series*, 1995.
28. Abed, E.H. et al, "Stability and Dynamics of Power Systems with Regulated Converters". *Proceedings of the IEEE Symposium on Circuits and Systems*, vol. 1, 1995, pages 143-145.
29. Belkhat, M. et al, "Large Signal Stability Criteria for Distributed System with Constant Power Loads, *Proceedings of the 26th Annual IEEE Power Electronics Specialists Conference*, Atlanta, GA, 1995, pages. 1333-1338.
30. M. Al-Fayyumi, "Nonlinear dynamics and Interaction in Power Electronics Systems", *M.S. Thesis, Department of Electrical and Computer Engineering, Virginia Tech*, 1998.
31. Nayfeh, A.H, "Applied nonlinear dynamics", *John Wiley*, 1995
32. Seydel Rudiger, "From Equilibrium to Chaos", *Elsevier Science Publishing*, 1988.
33. Dobson. I, Alvarado F, De Marco C. L, "Sensitivity of Hopf Bifurcations to Power System Parameters", *Proceedings of the 31st Conference on Decision and Control*, Arizona, December 1992, pp. 2928-2933.
34. Dobson. I., "Computing a Closest Bifurcation Instability in Multidimensional Parameter Space," *Journal of Nonlinear Science*, Vol. 3, 1993, pp. 307-327.